Molecular Dynamics Study of Rheological Properties of Liquid Alkanes under High Pressure and Shear

Eunju Julia Choe

Submitted in fulfilment for the degree of

Doctor of Philosophy

Department of Chemistry

September 2017

Contents

List of Figures

List of Tables

Acknowledgement

Every human endeavour requires contributions from many others. This work is not an exception. I am indebted to many people for their help and support during the course of this study.

First of all, I would like to express my sincere gratitude to the late Professor Mark Rodger for his kindness, support, and patience. He was one of the most generous persons I have met as well as being an inspiring scientist. I miss him starting an answer with 'Yes and no.' with a twinkle in his eye. I am sorry that he is not here to see this work completed.

I wish to thank Doctor Rebecca Notman for her support and encouragement in finishing this thesis. I appreciate Doctor James Elliott and Professor Vas Stavros for the guidance and insight.

I also thank Salvatore Cosseddu, Aaron Finney and all the members of the Molecular Simulations Group at Warwick for discussions and their friendship which made my time at Warwick more enjoyable.

Most importantly, I would like to thank Yongmann for always being there for me. And Daddy, I miss you.

Declaration

This thesis is submitted to the University of Warwick in support of my application for the degree of Doctor of Philosophy. It has been composed by myself and has not been submitted in any previous application for any degree.

Abstract

In this study, molecular dynamics (MD) simulations have been performed to study rheological properties of liquid alkanes under a range of pressures up to several GPa and high shear rates. The liquid alkane considered in this study is 2,4-dicyclohexyl-2-methylpentane (DCMP), which is a highly viscous fluid. Two further molecular motifs, octadecane (Linear) and 1,6-dicyclohexyl-hexane (Dumbbell) were chosen as comparison. The rheological properties of DCMP under high pressure were studied using molecular dynamics simulations. A wide range of pressure (1 atm $\leq P \leq$ 10 000 atm) and shear (5.47×10^7 s^{-1} $\leq \dot{\gamma} \leq 5.47 \times 10^{11}$ s^{-1}) conditions have been considered. Simulation parameters have been carefully chosen from preliminary simulations. MD allows access to understanding not always available experimentally.

The present simulation results confirm that the density of all three motifs increase as pressure increases. The results also show that the mean squared displacements of molecules decrease as pressure increases. At pressures higher than 3000 atm, the movement almost ceases for DCMP and Dumbbell implying a solid-like behaviour at very high pressures. The viscosity of DCMP is higher than that of Dumbbell, but comparable to Linear. As molecules tend to adopt compact shapes at high pressures, this affects their rheological properties accordingly. The

viscosity of Dumbbell is found to be the lowest among the three. Viscosities increase with pressure for all three molecules with larger changes with DCMP and Linear.

It is found that the pressure of the systems increase when the shear is applied. The viscosity of DCMP and Dumbbell increase as pressure increases. The viscosity of DCMP is found to be higher than that of Dumbbell, especially in the high pressure region. DCMP and Dumbbell show the shear thinning behaviour. The start of a plateau is observed for DCMP and the viscosity in the plateau is at the same order of magnitude as the zero shear viscosity estimated from the Stokes-Einstein relation for low pressure systems.

Chapter 1

INTRODUCTION

The viscosities of Non-Newtonian fluids do not have a linear response to an external force. These fluids are widely used in everyday life and in engineering systems, from tomato ketchup to 3D printing and gear fluids. This is mainly due to the fact that the behaviour can be manipulated widely by altering the working environments. For example, squeezing out ketchup is made easier by shaking the bottle, this is recognised as shear thinning behaviour.

Among non-Newtonian fluids of engineering applications, 2,4-dicyclohexyl-2-methylpentane (DCMP) has been in use for more than two decades for various use, in particular as part of traction lubricant systems. Typical pressure conditions that traction lubricants are exposed to, vary from atmospheric to GPa range.[1,2]

DCMP is a highly viscous fluid.[3] It shows shear-thinning behaviour as a lubricant under ambient conditions but is known to form a pseudo-solid pad under pressures of industrial interest.[2,4] By taking advantage of this behaviour, one of the applications of DCMP is a lubricant acting as part of traction drive mechanisms such as continuously variable transmissions (CVTs) or infinitely variable transmissions (IVTs) shown in Figure 1.1. However, little understanding of its behaviour on a molecular level is known.

A traditional gear system uses a set of cogs as shown in Figure 1.1(a) allows the speed, torque, or direction of the machine to be changed. The change depends on the design of cogs and occurs typically in steps. On the other hand, CVTs or IVTs have smooth surfaces. When two solid surfaces that are separated by a liquid lubricant roll, as in Figure 1.1(b), the pressure and shear exerted on the liquid changes. By engaging a fluid lubricant that changes viscosity behaviour depend-

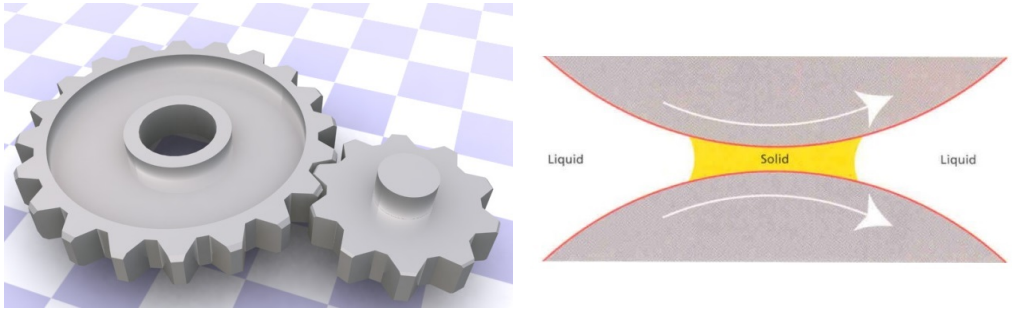

(a) A conventional gear (b) Pressure strain of IVT

Figure 1.1: Schematic drawing of (a) conventional gears and (b) an infinitely variable transmission (IVT) system.

ing on the condition, CVT or IVT can vary the speed and torque continuously without the cogs.

Despite its wide range of applications, there is little research on DCMP at a molecular level, though the structure of the molecule as well as its composition has a great impact on bulk properties. In this project, we aim to understand the structure and rheological behaviour of DCMP under high pressure and shear and its dependence on molecular motifs. Two further molecular motifs of the same molecular weights, octadecane and 1,6-dicyclohexane, are chosen as comparison motifs. These molecular motifs are shown in Figures 4.1 and 4.2.

In this study, molecular dynamics (MD) simulations have been performed to investigate behaviours of DCMP. A range of pressures from ambient pressure to 10 000 atm were studied. A wide range of shear rates ($5.47 \times 10^7/\text{s} \leq \dot{\gamma} \leq 5.47 \times 10^{11}/\text{s}$) were also considered for various pressure conditions. Transport properties were calculated and structures of chosen molecules were investigated in terms of distances and alignments between molecules and also their components.

A brief history of MD research as well as studies regarding rheological behaviour of liquids is described in Chapter 2. The structure of the thesis is as follows. The theories relating to MD and rheology are summarised in Chapter 3. Details of simulation and analysis methods are described in Chapter 4 with pre-

liminary results. There are four main results chapters. Chapter 5 provides studies of DCMP under various pressures in terms of rheological behaviour and structural analysis. Rheological behaviour of DCMP is compared to those of the two other motifs in Chapter 6. Chapter 7 discusses the molecular structure of DCMP in comparison to two other motifs. Shear viscosity of DCMP and the other molecules are presented in Chapter 8. Finally, conclusions of the project and suggestions for future work are summarised in Chapter 9.

Chapter 2

LITERATURE REVIEW

The main objective of this study is to understand how the molecular structure of a fluid can affect its physical properties using molecular dynamics (MD). A review of the relevant literature is presented in the following sections.

2.1 Molecular dynamics

2.1.1 Early works of molecular dynamics

From the early days of computers, MD simulations have been used for science research. The Monte Carlo method was initiated by the Los Alamos group and it

was the first example of computer simulations of molecules.[5] One of the earliest MD work was that of Alder and Wainwright,[6,7] which calculated molecular dynamic motion of hard sphere systems. It used hard sphere particles and square well potentials of attraction with periodic boundary conditions. Rahman[8] performed computer simulations to study liquid argon using the Lennard-Jones potential. Based on this study, Verlet[9,10] presented a way to integrate the equation of motion of about a thousand particles with Lennard-Jones fluids. The Verlet scheme is still used in many MD simulation packages. Then in 1977, protein was simulated for the first time by McCammon *et al.*[11] using MD for bovine pancreatic trypsin inhibitor (BPTI). Over the years, the MD method has become a useful research tool as computing power increases.

These early studies first started in the 1970s.[12,13] Further works were carried out in the 1990s and early 2000s when the predictive nature of the simulations were established and the quality of force-field that was needed was identified. The studies have moved on towards bridging the gap between experimental regime and the simulations regime and towards detailed understanding of molecular behaviours. Earlier MD works laid the foundation of the current computational study of rheology and provides a good starting point for this project.

2.1.2 Application of molecular dynamics

The molecular dynamics simulation method has been widely used in various fields. Melt dynamics and phase transition were studied using MD simulations.[14] The MD method was used in modelling nanocatalyst growth,[15] and membrane proteins.[16] Transport properties of hydrocarbons were studied by MD simulations. The rheological behaviour of liquids was studied,[17–19] in particular, in ionic liquids[20,21] and in polymers.[22,23] Also, temperature dependence of viscosity[21] was investigated. How viscosity was affected by the structure of molecules was studied.[19] Equilibrium Molecular Dynamics (EMD)[24] and Non-Equilibrium Molecular Dynamics (NEMD) methods were employed for this.

The viscosity of DCMP at low shear rates are reported by Bair and his colleagues.[25,26] At low-shear rates, the viscosity of DCMP increased more rapidly than the viscosity of other hydrocarbons considered such as Poly-α-Olephines or squalane (2,6,10,15,19,23-Hexamethyltetracosane) at both 40 °C and 100 °C . Low-shear viscosity of DCMP changed from about 10^{-2} Pa·s to over 10^{3} Pa·s at 40 °C and from 10^{-3} Pa·s to over 10 Pa·s at 100 °C when pressure increased from 0.1 MPa to 378 MPa. Also, Asano *et al.*[27] reported experimental viscosity values of DCMP.

Molecules in the present study are represented using the UA model, where

hydrogens are incorporated in carbon sites. The UA model was employed successfully in various studies where the time scale of the interest is slower than movements of atoms in a molecule,[14,28] (GROMOS UA and Martini Coarse Grain),[29] CG MD liquid cyclohexane.[30]

UA model calculations were compared to explicit-atom model calculations for hydrocarbons[31,32] and for perfluoroalkanes.[33,34] According to these works, UA force fields parameterised for phase equilibria calculations have been shown to underpredict the viscosity but are able to capture the temperature dependence and pressure dependence well.

Kiran and Sen[35] measured high pressure viscosities and densities of *n*-butane, *n*-pentane, *n*-hexane, and *n*-octane at pressures ranging $P = 10$ - 70 MPa and temperatures $T = 310$ - 450 K. They found that as the carbon number of the alkane increased, the viscosity and density increased. Furthermore, for each alkane, viscosity also increased with pressure and decreased with temperature. They also suggested empirical equations for the density - viscosity and temperature-viscosity relations with sets of parameters.

2.1.3 Computer simulations of liquids

There has been many further MD studies of rheological properties of linear alkanes.[36–39] However, only a few studies were on more complicated structures such as DCMP which contains cyclohexyl rings and methyl groups. Washizu *et al.*[40,41] compared frictions of linear- and ring- structured alkanes in elasto-hydrodynamic lubrication and boundary lubrication regimes. Results showed that MD results were reliable for predicting oil film thicker than 5 nm and agreed with experiment data quantitatively for sub-micron films.

MD simulations with shear rates are rare and these data under high pressures are even rarer. Studies of transport properties of hydrocarbons using MD simulations started in the 1970s.[12,13]

Temperature dependence of viscosity of liquids was also studied. Mauro *et al.*[42] suggested a new formula and parameters for the glass-forming liquids and compared results to some of the existing equations.

2.2 2,4-dicyclohexyl-2-methylpentane

2.2.1 Characterisation of 2,4-dicyclohexyl-2-methylpentane

2,4-dicyclohexyl-2-methylpentane (DCMP) shows shear-thinning behaviour as a lubricant under normal conditions but is known to form pseudo-solid pads under a certain pressure-shear conditions. This was also experimentally observed by Ohno.[2] He showed that the structure of lubrication oils can transform into a quasi-solid structure under high pressure with a conventional automotive traction fluid (Nissan CVT Fluid: KTF-1) using a maximum contact pressure of 4 GPa. Hirayama *et al.*[4] also observed solidification of oil under high pressure. The viscosity of DCMP is then reported to return back to its 'normal' liquid state level when the high pressure is removed.

Low shear rate viscosity behaviours of DCMP were reported by Bair and his co-workers.[25,26] At low-shear rates, viscosity of DCMP increased at a more rapid rate than any other hydrocarbons compared such as Poly-α-Olephines or squalane ($2,6,10,15,19,23$-Hexamethyltetracosane) at both 40 °C and 100 °C. Low-shear viscosity of DCMP changed from about 10^{-2} Pa·s to over 10^{3} Pa·s at 40 °C and from 10^{-3} Pa·s to over 10 Pa·s at 100 °C in pressure ranges of 0.1 MPa to 378 MPa. Also, Asano *et al.*[27] reported experimental viscosity values

of DCMP.

2.2.2 Pressure dependency of viscosity of 2,4-dicyclohexyl-2-methylpentane

Pressure dependency of viscosity of a liquid can be estimated from the Barus equation[43] as shown in Equation (2.1),

$$\eta = \eta_0 e^{\alpha P}, \tag{2.1}$$

where η_0 is the viscosity at 0.1 MPa and α is the pressure coefficient. η_0 and α values were measured at a set of temperatures by Asano *et al.*[27,44] and these values are tabulated in Table 2.1.

DCMP has higher α-values compared to other hydrocarbons,[27,44] therefore it is expected to show a larger viscosity change as pressure increases. Applying

T /°C	η_0 /Pa·s	α /GPa^{-1}	T /°C	η_0 /Pa·s	α /GPa^{-1}
-5	0.546	53.2	15	0.0584	41.2
0	0.281	49.6	20	0.0387	39.0
5	0.156	46.5	25	0.0267	37.0
10	0.0928	43.7	35	0.0142	33.7

Table 2.1: Observed η_0 and α value for DCMP from experiments.[27,44] Pressure-viscosity coefficient α is higher than other liquids compared.

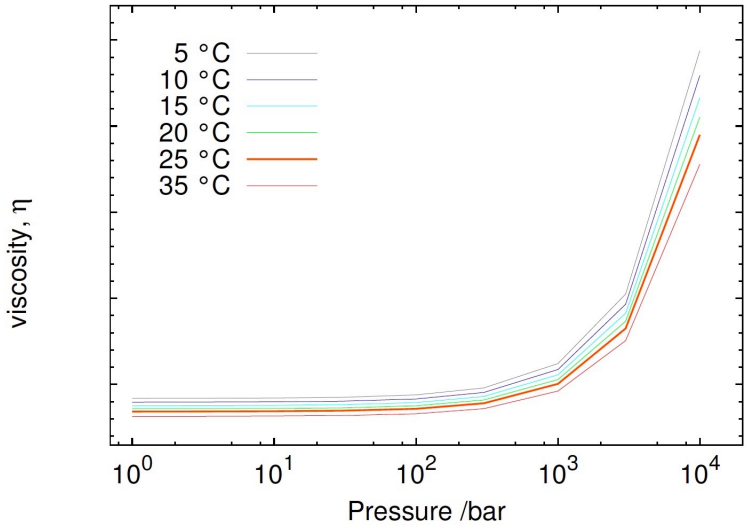

Figure 2.1: Schematic diagram of the viscosity of DCMP at various temperatures based on the Barus equation and the measurement data available in literature[27,44] tabulated in Table 2.1. The viscosity increases exponentially with an exponent of α. The largest change seems to occur between 10^3 bar and 10^4 bar.

these data to the Barus equation, the viscosity of DCMP under 10 000 bar and 25 °C is estimated to be in the order of 10^{15} Pa·s.

This viscosity behaviour of DCMP over a range of temperatures is shown in Figure 2.1. This figure shows that the viscosity of DCMP increases exponentially, as suggested by the Barus law's exponential form. The increase is more noticeable, significantly at pressures above 1000 bar. Figure 2.1 suggests that the pressure conditions under which DCMP is typically found in engineering use will see DCMP experience dramatic viscosity changes.

The relationship between the traction properties of traction fluids and the molecular structures was studied by Hata and Tsubouchi.[45] After studying viscosities of 38 compounds, they stated that the traction properties of these fluids were closely related to the molecular structure details such as the presence of rings, length of aliphatic alkylene chains, soft C–C bond in molecules, and the position of its substituents. Also, Kioupis and Maginn[46,47] used equilibrium and nonequilibrium MD to predict viscosities for linear and branched alkanes using poly-α-olefines of C_6–C_{20}. They simulated three molecular structures (linear C_{18}, star-shaped, and highly branched) at 40 °C and 100 °C , and calculated viscosities at different shear rates ranging 10^9 - 10^{11} /s. It was also observed that aligning of molecules did not always result in shear-thinning.

Viscosity depends on shear rate as well as pressure. McCabe *et al.*[32] calculated viscosity at various pressures. Their NEMD simulations showed that the viscosity of 9-octylheptadecane strongly depended on strain rate. They observed shear thinning at higher strain rates and a Newtonian plateau at the lowest strain rates. The onset of shear thinning occurred at the higher shear rate in the simulations at the higher temperature. Also this onset is correlated with the inverse of the rotational relaxation time calculated from EMD simulations. The plateau viscosity was larger at higher pressure, but once it entered the shear thinning region, viscosities were similar across all pressures. They obtained the pressure-viscosity

coefficient from NEMD simulation results, which was close to the value obtained from experimental data.

Chapter 3

THEORIES

3.1 Molecular dynamics

Molecular dynamics (MD) is a powerful computer simulation method that enables us to understand behaviour of materials at the molecular level. The MD simulation generates configurations of particles in a molecular system, and calculates their evolution in time by integrating Newton's equation of motion. This is a useful method connecting macroscopic and microscopic properties of a material. The MD method started in the 1950s[6,7] and has become a standard research tool as the power of the computer has increased.

In MD, a set of particles (atoms or molecules) are moving at a velocity ac-

cording to Newton's equation of motion at a given thermodynamic condition. The particle positions are available from the MD simulations and this information is used to understand the molecular behaviour of the material. Typically, particles are placed in a finite simulation box of size L^3 (where L is the size of the box in one direction). With an initial position and velocity distribution, the forces acting on each molecule are calculated; each particle then moves according to the calculated force. By repeating this process, the movement of each particle can be calculated, and from these movements physical properties of the particles can be obtained.

3.1.1 Inter-atomic potential

Forces in MD are calculated in terms of an interatomic potential. The potential energy of a system containing N atoms can be expressed in several terms, depending on the coordinates of atom, pairs, triplets, etc.

$$U = \sum_i v_1(\mathbf{r}_i) + \sum_i \sum_{j>i} v_2(\mathbf{r}_i, \mathbf{r}_j) + \sum_i \sum_{j>i} \sum_{k>j>i} v_3(\mathbf{r}_i, \mathbf{r}_j, \mathbf{r}_k) + \cdots \tag{3.1}$$

The first term in Equation (3.1), $v_1(\mathbf{r}_i)$, accounts for the effect of an external field on the system. The second term, $v_2(\mathbf{r}_i, \mathbf{r}_j)$, is a pair potential and it depends on the distance between two atoms, and the third term, $v_3(\mathbf{r}_i, \mathbf{r}_j, \mathbf{r}_k)$, is a three-body term.

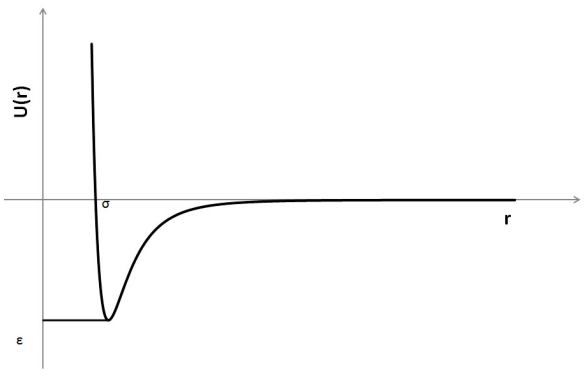

Figure 3.1: Lennard-Jones potential. r is the distance between two particles, and σ is the critical distance where the potential energy is zero. The negative value of $\frac{dU}{dr}$ represents repulsive force, and the positive value indicates attractive force.

From the third term onwards, the calculation cost outweighs the benefit for accuracy. Therefore, an effective pair potential can be used in computer simulations to incorporate the effect of the three-, four-, and many-body terms.

$$U_{eff} \approx \sum_i v_1(\mathbf{r}_i) + \sum_i \sum_{j>i} v_2^{eff}(\mathbf{r}_i, \mathbf{r}_j). \tag{3.2}$$

As shown in Figure 3.1 and Equation (3.2), the potential energy between two particles is described as a function of distance, r. Two particles are at their most stable state, *i.e.*, energy minima, when the potential energy is $U(r_\varepsilon) = -\varepsilon$, while the potential energy is zero when they are at a distance of $r = \sigma$. The repulsive force is stronger when two particles are in close proximity ($r < r_\varepsilon$) and the attractive force is dominant when they are far apart ($r > r_\varepsilon$).

One of the most commonly used pair potentials is Lennard-Jones potential proposed by Lennard-Jones.[48] This models two-body potential using a $\left(\frac{\sigma}{r}\right)^{12}$ term for the repulsive force and a $\left(\frac{\sigma}{r}\right)^{6}$ term for the attractive force. The relation can be expressed as in Equation (3.3).

$$U(r) = 4\varepsilon \left[\left(\frac{\sigma}{r}\right)^{12} - \left(\frac{\sigma}{r}\right)^{6} \right], \tag{3.3}$$

where ε is the minimum energy, σ is the distance where the potential energy $U(r)$ is zero, and r is the distance between two particles.

3.1.2 Freely jointed chain model for polymer

The freely jointed chain model is a simple model for a single polymer in solution. The basis of many single polymer theories stem from Flory's *Freely Jointed Chain* (FJC) model[9]. This model assumes that chemical bonds are free to rotate and posses a uniform distribution of bond angles. The end-to-end distance, or chain vector $\mathbf{r}$ is described by Equation (3.4). This is the summation over all bond vectors L_i, where n is the number of bonds in the chain (see Figure 3.2). The uniform distribution of bond angles necessitates that the average chain vector over all conformations is zero. The square of the chain vector averaged over all conformations however, has a finite value. With the assumption that L is the average

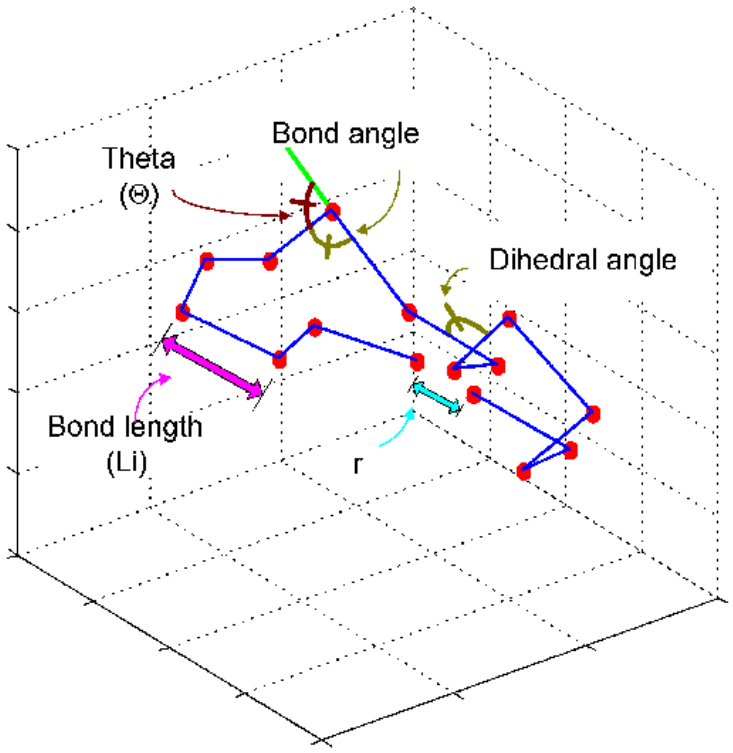

Figure 3.2: Worm-like chain with fixed bond length and bond angle (109.5°), and random dihedral angle.

bond length, the average square chain vector simplifies to Equation (3.5), where the brackets $< \cdot >$ denote the statistical average over all conformations.

$$L = \frac{\sum_i^n L_i}{n}, \tag{3.4}$$

$$< \mathbf{r}^2 > = nL_i^2, \tag{3.5}$$

$$C_n = \frac{< \mathbf{r^2} >}{nL^2}. \tag{3.6}$$

Flory uses this relation to define the characteristic ratio C_n of a polymer, as in Equation (3.6). By definition C_n is a unity for freely jointed chains. For other models, such as the worm-like chain (WLC), which do not assume that the bond angle is free to rotate, C_n exceeds unity. Based on viscosity studies conducted by Debye,[49] it is well known that r^2 is related to the radius of gyration, R_g, by Equation (3.7).

$$< R_g^2 >= \frac{< r^2 >}{6}. \tag{3.7}$$

3.1.3 Force fields

Force field is used in MD to calculate an atomic system. It is a set of energy functions or interatomic potentials, and includes the functional form and parameters. These parameters can be either derived from experimental data or quantum mechanics calculations. Depending on the degree of explicitness, all-atom force field, united-atom (UA) force field, or coarse grained potentials can be adopted. All-atom force field provides parameters for every atom in a system, whereas united-atom force field groups light atoms such as hydrogen and a single heavy atom such as carbon together. Methyl group (-CH_3), methylene bridge (-CH_2-), hydrogen bond (-CH-), or a quaternary carbon (-C-) are all treated as one site. The united-atom force field is used mainly in simulations where the fast movement of hydrogen does not contribute much to the property of interest. For longer simu-

lations of larger materials such as proteins or polymers, coarse-grained potentials are often used. Coarse-graining usually groups several heavy atoms together and treats them as a single unit.[50–55]

There are many force fields available in the literature, including AMBER (Assisted Model Building with Energy Refinement),[56] GROMOS (GROningen MOlecular Simulation),[57] OPLS (Optimized Potentials for Liquid Simulations).[58,59] In this study CHARMM force field was used among these force fields. CHARMM (Chemistry at HARvard Macromolecular Mechanics) force field is developed by the CHARMM Development Project.[60,61] CHARMM is also the name of an MD package with a broad range of applications. CHARMM force fields are generally good for small molecules and macromolecules although it was primarily developed for biological applications such as peptides, proteins and lipids.

3.1.4 Periodic boundaries

A physical experiment contains a huge number of particles and the direct MD simulation of these particles is intractable even for the most powerful computers available today. In contrast, a relatively small simulation box is used in MD and the number of particles used in a simulation system is much smaller than the number found in the day-to-day physical system. Particles located near the edge

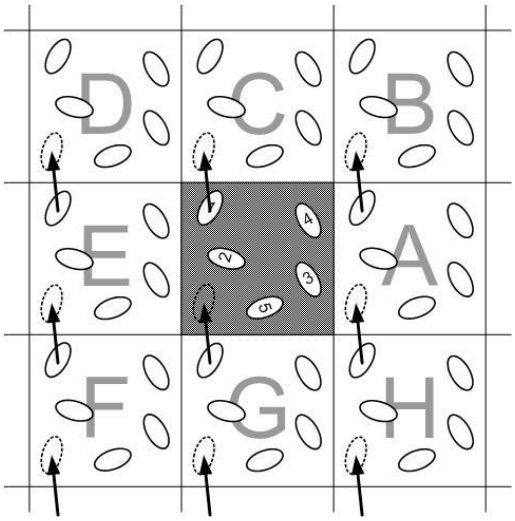

Figure 3.3: Application of periodic boundary condition in 2D.

of the simulation box experience asymmetric force field due to the finite size of the simulation box. A periodic boundary condition (PBC) is used to overcome this issue.

The periodic boundary condition concept is graphically presented in Figure 3.3. The centre box is the main simulation box, and infinite number of identical simulation boxes are assumed around it. The particles in the central box move according to Newton's equation of motion. Sometimes particles move beyond the wall of this simulation box and move to the adjacent one. When particle 1 moves to box C, the equivalent particle in box G moves in to the central simulation box. For every particle that moves out of the central box, there is an identical particle moving into a box through the opposite boundary. Therefore, the number of particle in the simulation system is always preserved. With the PBC, the simulation

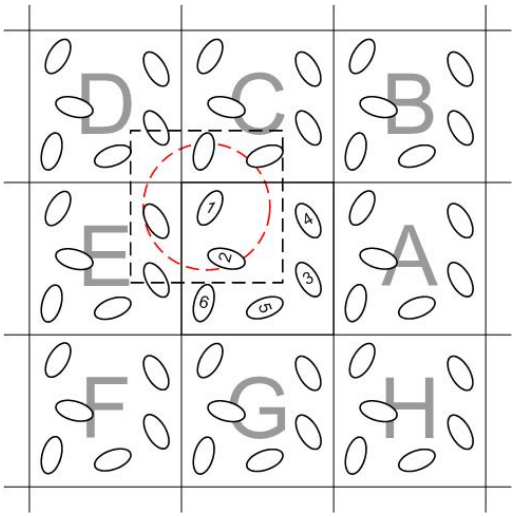

Figure 3.4: A 2D example of minimum image convention in MD.

box is able to replicate the physical system while using a much smaller number of particles.

An MD simulation can be made even more efficient by employing the concept of a cut-off radius, r_{cut}. Because the force between two molecules become rapidly smaller as the distance increases (see Equation (3.3)), molecules far apart can be safely ignored from the calculation without affecting the accuracy of the simulation, and molecules only within the cut-off radius ($r < r_{cut}$) are considered for an efficient calculation of the potential energy instead of considering all particles in the simulation box.

The periodic boundary condition is incorporated with the cut-off radius, and the nearest atoms in a neighbouring duplicated simulation box will be considered

rather than atoms in the same simulation box. A 2-D example of the minimum image convention is presented in Figure 3.4. Atoms inside of the black dashed line will be included in the calculation regardless of the box it belongs. The red dashed line represents the spherical truncation, with a radius r_{cut}. Some atoms in the central simulation box will be ignored unless they come within r_{cut} circle, and atoms in other simulation box will be counted as long as they are within $r < r_{cut}$. To avoid an atom 'seeing' itself, the central simulation box needs to be large enough to satisfy $L > 2r_{cut}$.

3.1.5 Lees-Edwards boundary condition

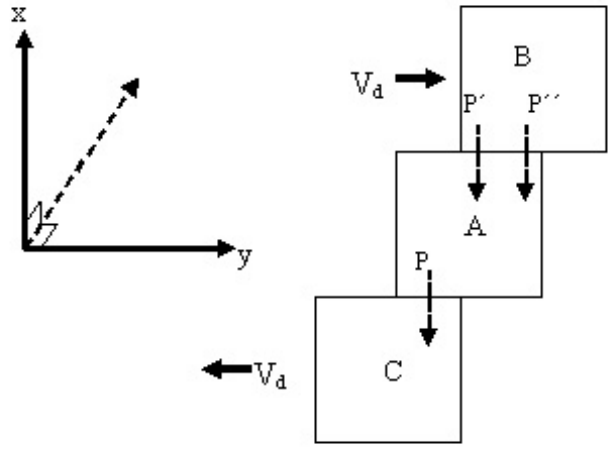

Figure 3.5: Lees-Edwards periodic boundary condition.

The use of exact correlation function expressions to obtain the viscosity in

the limit of small shear, although exact, is nevertheless indirect: the fluid is studied in true equilibrium and the effect of a small shear is deduced from correlation functions found.[12] In simulating a liquid under a high shear stress, the main requisite of any approach is the representation of a macroscopic element of the fluid by a small sample. The box containing the particles is considered as being embedded in a fluid which has constant velocity gradient in the x direction, for example. The cyclic boundary conditions which are normally associated with equilibrium calculations need to be modified to maintain the system under a shearing stress in a steady state. The maintenance of a steady state is the basic problem in the molecular simulation of this type. Once stationary conditions have been obtained, results of the required accuracy may be produced by taking all averages over a sufficiently large number of time steps.

One such scheme which adapts periodic boundary conditions to be consistent with shear is shown in Figure 3.5. The box under consideration, A, is surrounded by cyclic images of itself in the yz-plane, as in the 'conventional' calculations. The neighbouring cells in the x-direction are made to drift with a specified speed V_d in the y-direction with respect to the central cell. The system may be started from a perfect lattice configuration with the neighbouring boxes B and C aligned to A, as in an equilibrium study. The particles in A are given a random velocity whose root mean square value is V_d, the mean thermal speed. In addition to this an

atom at the point (X,Y,Z) is given an extra velocity in the y-direction ΔV, where

$$\Delta V = V_d \left(\frac{X}{L} - \frac{1}{2} \right), \tag{3.8}$$

resulting in a linear velocity profile centred about the midpoint of box A. This method may be used to initiate the system in as near as possible static conditions. Alternatively, the system may be started in another state and the decay to static conditions may be observed qualitatively.

Imagine that during the calculation a particle leaves the principal box A at point P with a y-direction velocity component Y_y. Under normal cyclic boundary conditions the particle will be reintroduced into the cell at P$'$ with all three velocity components unaltered. If the cell is considered to be an element of fluid, all of which has a linear velocity profile it will be seen that the particle returns to the box at P$''$ with velocity V' where,

$$\begin{aligned} V_y' &= V_y + V_d, \\ V_x' &= V_x, \\ V_z' &= V_z. \end{aligned} \tag{3.9}$$

The sign in the first equation of Equation (3.9) is reversed for particles going through the boundary in the opposite direction.

The method initially employed used the boundary conditions for velocities as shown in Equation (3.9), but reintroduced the particle at point P′, since it was argued that the precise location of re-entry was unimportant. This method, however, fails to produce stable velocity gradients over long periods.[12] The reason for this failure is attributed to the flux of momentum through the inter-atomic potential field. In addition to the momentum carried by a particle across the walls of the basic cell, there is another flux ΔF given by,

$$\Delta F = \lim_{\Delta t \to \infty} \frac{1}{\Delta t} \int_{t}^{t+\Delta t} \Sigma' F_{ij}(t')dt', \tag{3.10}$$

where Σ' denotes summation over all i and j atoms such that the line joining them crosses the boundary of the cell which lies in the yz-plane shown in Figure 3.6.

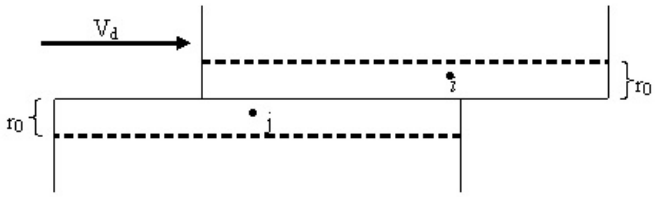

Figure 3.6: Sliding surfaces where r_0 is the potential cut-off radius.

$$F = \Sigma F_{ij}(t). \tag{3.11}$$

The time variation of the quantity Equation (3.11) clearly depends on the shear

rate. In the equilibrium case the limiting value of the time average must be zero. To evaluate the contribution in the general case, the force evaluation routine must be modified to allow neighbouring cells to slip past one another. Consider, for example, the interaction of atoms i and j as shown in Figure 3.7. Under normal conditions atom i would be considered as interacting with the cyclic reflection of j at position j'. However, since neighbouring boxes are considered as slipping with respect to each other, i is now regarded as interaction with j' where the displacement j'- j'' is in the x-direction only with a magnitude X,

$$X = n_t V_d \Delta t - \left[\frac{n_t V_d \Delta t}{L} \right] L, \tag{3.12}$$

where n_t denotes the number of time steps and [Y] represents the highest integer which is less than Y.

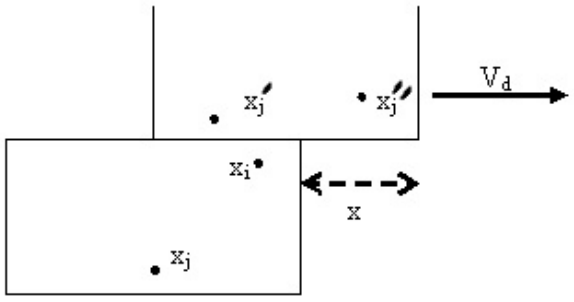

Figure 3.7: The force exerted on particles and displacement of boxes.

Having modified the calculation of the forces in this way, it becomes impor-

tant to reintroduce a boundary traversing atom at an appropriate place that is point P$''$ in Figure 3.7. This makes the model completely consistent. Any inconsistency in the model would result in non-conservation of energy.

The model as described so far would give rise to a slow heating up of the system. This effect may readily be assessed as follows. In Figure 3.6 atom i exerts a mean force ΔF on atom j, so that

$$\text{mean rate of work} = \Delta F \overline{V_x}. \tag{3.13}$$

$\overline{V_x}$ representing the mean relative velocity of i and j atoms,

$$\overline{V_x} = \frac{V_D r_0}{L}, \tag{3.14}$$

where V_D is the speed differential between opposite sides of the box (L). If there are n particles in the model, this work is dissipated among $2nr_0/L$ atoms. Therefore

$$\frac{dT}{dt} = \frac{\Delta F V_D}{2n\kappa}, \tag{3.15}$$

where κ is the Boltzmann constant. Taking the case for which V_D is the thermal speed, this expression gives the heating rate of about 8 K per thousand time steps (when $\Delta t = 2.0 \times 10^{-14}$s). Indeed a trend with this order of magnitude was

observed in the preliminary simulations.

3.1.6 Time advancement

Newton's equation of motion for an atomic system can be written as in Equation (3.16).

$$m_i \ddot{\mathbf{r}}_i = \mathbf{f}_i, \tag{3.16}$$

where m_i and $\mathbf{f}_i$ are the mass and force acting on an atom i, and $\mathbf{a}_i = \ddot{\mathbf{r}}_i$ is the acceleration. These equations can be applied to the centre of mass of an atom, with $\mathbf{f}_i$ being the total force action on atom i.

Verlet algorithm

In MD, the position of each particle is monitored to find the physical properties. One of the most widely used methods for calculating this is the Verlet algorithm.[62] The position or Cartesian coordinates of a particle, $\mathbf{r}$, is advanced via,

$$\mathbf{r}(t+\Delta t) = 2\mathbf{r}(t) - \mathbf{r}(t-\Delta t) + \Delta t^2 \mathbf{a}(t), \tag{3.17}$$

where Δt is the time step size, $\mathbf{r}(t)$ is the current position, $\mathbf{r}(t-\Delta t)$ the previous position, $\mathbf{r}(t+\Delta t)$ the next position, and $\mathbf{a}(t)$ the acceleration at the current time.

Please note that the velocity of the particle is absent from Equation (3.17). From the Taylor expansions about $\mathbf{r}(t)$,

$$\begin{aligned} \mathbf{r}(t+\Delta t) &= \mathbf{r}(t) + \Delta t\mathbf{v}(t) + \frac{1}{2}\Delta t^2\mathbf{a}(t) + \dots \\ \mathbf{r}(t-\Delta t) &= \mathbf{r}(t) - \Delta t\mathbf{v}(t) + \frac{1}{2}\Delta t^2\mathbf{a}(t) - \dots . \end{aligned} \tag{3.18}$$

If velocity is needed, it can be calculated from Equation (3.19),

$$\mathbf{v}(t) = \frac{\mathbf{r}(t+\Delta t) - \mathbf{r}(t-\Delta t)}{2\Delta t}. \tag{3.19}$$

The Verlet algorithm is compact and simple to program. It is reversible in time due to its symmetry, and conserves linear momentum with conservative forces. On the other hand, its handling of velocity is a bit awkward and the accuracy of the velocity is lower because as shown in Equation (3.19), $\mathscr{O}(\Delta t^2)$ is added to $\mathscr{O}(\Delta t^0)$.

Leap-frog scheme

Some modifications to the Verlet algorithm have been proposed. One of them is the half-step 'leap-frog' scheme,

$$\mathbf{r}(t+\Delta t) = \mathbf{r}(t) + \Delta t \mathbf{v}(t+\frac{1}{2}\Delta t), \tag{3.20a}$$

$$\mathbf{v}(t+\frac{1}{2}\Delta t) = \mathbf{v}(t-\frac{1}{2}\Delta t) + \Delta t \mathbf{a}(t). \tag{3.20b}$$

The current position $\mathbf{r}(t)$, acceleration $\mathbf{a}(t)$, and the mid-step velocity $\mathbf{v}(t-\frac{1}{2}\Delta t)$ are needed. The velocity equation (Equation (3.20b)) is implemented first, and the velocity leaps over the coordinates to give the next mid-step values $\mathbf{v}(t+\frac{1}{2}\Delta t)$. During the calculation, the current velocity can be calculated using,

$$\mathbf{v}(t) = \frac{1}{2}\left(\mathbf{v}(t+\frac{1}{2}\Delta t) + \mathbf{v}(t-\frac{1}{2}\Delta t)\right). \tag{3.21}$$

Integration algorithm used in DL_POLY Classic was this Verlet Leapfrog scheme since this is time reversible and simple.

Velocity Verlet algorithm

To improve the velocity calculation, another modification to the Verlet algorithm was suggested. A Verlet-equivalent algorithm which utilises positions, velocities, and accelerations at time t was proposed.[63] The Velocity Verlet algorithm is formulated as,

$$\mathbf{r}(t+\Delta t) = \mathbf{r}(t) + \Delta t\mathbf{v}(t) + \frac{1}{2}\Delta t^2\mathbf{a}, \tag{3.22a}$$

$$\mathbf{v}(t+\Delta t) = \mathbf{v}(t) + \frac{1}{2}\Delta t\left[\mathbf{a}(t) + \mathbf{a}(t+\Delta t)\right]. \tag{3.22b}$$

The Verlet algorithm can be recovered by eliminating the velocities. It involves two steps; first, the position is updated using Equation (3.22a) and the velocity is updated at mid-step using,

$$\mathbf{v}(t+\frac{1}{2}\Delta t) = \mathbf{v}(t) + \frac{1}{2}\Delta t\mathbf{a}(t). \tag{3.23}$$

Then the force and acceleration are updated, and the velocity is calculated using

$$\mathbf{v}(t+\Delta t) = \mathbf{v}(t+\frac{1}{2}\Delta t) + \frac{1}{2}\Delta t\mathbf{a}(t+\Delta t). \tag{3.24}$$

3.1.7 Thermostat

DL_POLY allows a choice of thermostats including Nosé-Hoover thermostat[64] and Berendsen thermostat[65] to maintain a constant temperature during simulations. For NVT simulations, Nosé-Hoover thermostat which generates trajectories in the NVT ensemble was used in this study. Newton's equations of motions are modified as:

$$\frac{d\mathbf{r}(t)}{dt} = \mathbf{v}(t), \tag{3.25}$$

$$\frac{d\mathbf{v}(t)}{dt} = \frac{\mathbf{f}(t)}{m} - \chi(t)\mathbf{v}(t). \tag{3.26}$$

The friction coefficient, χ, is controlled by the first order differential equation

$$\frac{d\chi(t)}{dt} = \frac{N_f k_B}{Q}(\mathcal{T}(t) - T_{ext}), \tag{3.27}$$

where $Q = N_f k_B T_{ext} \mathcal{T}_T^2$ is the effective 'mass' of the thermoststat, $\mathcal{T}_T$ is a specified time constant (normally in the range [0.5, 2] ps) and N_f is the number of degrees of freedom in the system. $\mathcal{T}(t)$ is the instantaneous temperature of the system at time t. In the Leapfrog scheme, χ is stored at half time-steps. The time advancement is conducted as follows:

$$\chi\left(t + \frac{1}{2}\Delta t\right) \leftarrow \chi\left(t - \frac{1}{2}\Delta t\right) + \frac{\Delta t\, N_f k_B}{Q}\left(\mathcal{T}(t) - T_{ext}\right)$$

$$\chi(t) \leftarrow \frac{1}{2}\Big[\chi\big(t-\frac{1}{2}\Delta t\big)+\chi(t+\frac{1}{2}\Delta t)\Big]$$

$$\mathbf{v}(t+\frac{1}{2}\Delta t) \leftarrow \mathbf{v}(t-\frac{1}{2}\Delta t)+\Delta t\left[\frac{\mathbf{f}(t)}{m}-\chi(t)\,\mathbf{v}(t)\right]$$

$$\mathbf{v}(t) \leftarrow \frac{1}{2}\Big[\mathbf{v}(t-\frac{1}{2}\Delta t)+\mathbf{v}(t+\frac{1}{2}\Delta t)\Big]$$

$$\mathbf{r}(t+\Delta t) \leftarrow \mathbf{r}(t)+\Delta t\,\mathbf{v}\big(t+\frac{1}{2}\Delta t\big). \tag{3.28}$$

The conserved quantity is derived from the extended Hamiltonian, in the form of:

$$\mathcal{H}_{NVT} = U + KE + \frac{1}{2}Q\chi(t)^2 + \frac{Q}{\mathcal{T}_T^2}\int_0^t \chi(s)ds. \tag{3.29}$$

Bond constraints of 10^{-8} Å were also applied in this study.

3.1.8 Barostat

In the NPT part of simulations, Hoover NPT barostat was used to maintain the average pressure of the system. Hoover barostat has a well defined conserved quantity and the equation of motion coupled with a Nosé-Hoover thermostat and a barostat in DL_POLY Classic.

For isotropic fluctuations, the equations of motion are:

$$\begin{aligned}
\frac{d\mathbf{r}(t)}{dt} &= \mathbf{v}(t) + \eta(\mathbf{r}(t) - \mathbf{R}_0), \\
\frac{d\mathbf{v}(t)}{dt} &= \frac{\mathbf{f}(t)}{m} - \left[\chi(t) + \eta(t)\right]\mathbf{v}(t), \\
\frac{d\chi(t)}{dt} &= \frac{N_f k_B}{Q}\left(\mathcal{T}(t) - T_{ext}\right) + \frac{1}{Q}\left(W_\eta(t)^2 - k_B T_{ext}\right), \\
\frac{d\eta(t)}{dt} &= \frac{3}{W}V(t)\left(\mathcal{P}(t) - P_{ext}\right) - \chi(t)\eta(t), \\
\frac{dV(t)}{dt} &= \left[3\eta(t)\right]V(t).
\end{aligned} \tag{3.30}$$

where $Q = N_f k_B T_{ext} \mathcal{T}_T^2$ is the effective 'mass' of the thermostat and $W = N_f k_B T_{ext} \mathcal{T}_P^2$ is the effective 'mass' of the barostat. N_f is the number of degrees of freedom, η is the barostat friction coefficient, R_0 is the system centre of mass, $\mathcal{T}_T$ and $\mathcal{T}_P$ are specified time constants for temperature and pressure fluctuations respectively, $\mathcal{P}(t)$ is the instantaneous pressure, and V is the system volume. The conservative quantity is:

$$\begin{aligned}
\mathcal{H}_{NPT} = U + KE + \mathcal{P}_{ext} V(t) + \frac{1}{2}Q\chi(t)^2 \\
+ \frac{1}{2}W\eta(t)^2 + \int_0^t \left(\frac{Q}{\mathcal{T}_T^2}\chi(s) + k_B T_{ext}\right) ds.
\end{aligned} \tag{3.31}$$

This algorithm is implemented as:

$$\chi\left(t+\frac{1}{2}\Delta t\right) \leftarrow \chi\left(t-\frac{1}{2}\Delta t\right) + \frac{\Delta t\, N_f k_B}{Q}\left(\mathcal{T}(t)-T_{ext}\right) + \frac{\Delta t}{Q}\left(W\eta(t)^2 - k_B T_{ext}\right)$$

$$\chi(t) \leftarrow \frac{1}{2}\left[\chi\left(t-\frac{1}{2}\Delta t\right) + \chi\left(t+\frac{1}{2}\Delta t\right)\right]$$

$$\eta\left(t+\frac{1}{2}\Delta t\right) \leftarrow \eta\left(t-\frac{1}{2}\Delta t\right) + \Delta t\left\{\frac{3V(t)}{W}\left(\mathcal{P}(t)-P_{ext}\right) - \chi(t)\,\eta(t)\right\}$$

$$\eta(t) \leftarrow \frac{1}{2}\left[\eta\left(t-\frac{1}{2}\Delta t\right) + \eta\left(t+\frac{1}{2}\Delta t\right)\right]$$

$$\mathbf{v}\left(t+\frac{1}{2}\Delta t\right) \leftarrow \mathbf{v}\left(t-\frac{1}{2}\Delta t\right) + \Delta t\left[\frac{\mathbf{f}(t)}{m} - \left[\chi(t)+\eta(t)\right]\mathbf{v}(t)\right]$$

$$\mathbf{v}(t) \leftarrow \frac{1}{2}\left[\mathbf{v}\left(t-\frac{1}{2}\Delta t\right) + \mathbf{v}\left(t+\frac{1}{2}\Delta t\right)\right]$$

$$\mathbf{r}(t+\Delta t) \leftarrow \mathbf{r}(t) + \Delta t\left(\mathbf{v}\left(t+\frac{1}{2}\Delta t\right) + \eta\left(t+\frac{1}{2}\Delta t\right)\left[\mathbf{r}\left(t+\frac{1}{2}\Delta t\right) - \mathbf{R}_0\right]\right)$$

$$\mathbf{r}\left(t+\frac{1}{2}\Delta t\right) \leftarrow \frac{1}{2}\left[\mathbf{r}(t) + \mathbf{r}(t+\Delta t)\right].$$

Five iterations with the standard Verlet leapfrog predictions for the initial estimates of $\mathcal{T}(t)$, $\mathcal{P}(t)$, $\mathbf{v}(t)$, and $\mathbf{r}(t+\frac{1}{2}\Delta t)$ were performed in DL_POLY Classic. The change in box size was updated with the new cell vectors and volumes from:

$$V(t+\Delta t) \leftarrow V(t) exp\left[3\Delta t\,\eta\left(t+\frac{1}{2}\Delta t\right)\right],$$

$$\underline{\underline{\mathrm{H}}}(t+\Delta t) \leftarrow exp\left[\Delta t\,\eta\left(t+\frac{1}{2}\Delta t\right)\right]\underline{\underline{\mathrm{H}}}(t). \tag{3.32}$$

where $\underline{\underline{H}}$ is the cell matrix whose columns are the three cell vectors **a**, **b**, and **c**.

3.1.9 DL_POLY

The MD simulations reported here were obtained using DL_POLY Classic.[66] DL_POLY Classic is a molecular simulation package designed to facilitate molecular dynamics simulations of various molecular systems on a distributed memory parallel computer.[67,68] DL_POLY Classic is based on a replicated data parallelism and suitable for simulations of up to 30 000 atoms on up to 100 processors. The generic form of the total configuration energy of a molecular system used in DL_POLY Classic is represented by Equation (3.33).

$$
\begin{aligned}
U(r_1, r_2, ..., r_N) = & \sum_{i_{bond}=1}^{N_{bond}} U_{bond}(i_{bond}, r_a, r_b) \\
& + \sum_{i_{angle}=1}^{N_{angle}} U_{angle}(i_{angle}, r_a, r_b, r_c) \\
& + \sum_{i_{dihed}=1}^{N_{dihed}} U_{dihed}(i_{dihed}, r_a, r_b, r_c, r_d) \\
& + \sum_{i_{inv}=1}^{N_{inv}} U_{inv}(i_{inv}, r_a, r_b, r_c, r_d) \\
& + \sum_{i=1}^{N-1} \sum_{j>i}^{N} U_{pair}(i, j, |r_i - r_j|) \\
& + \sum_{i=1}^{N-2} \sum_{j>i1}^{N-1} \sum_{k>j}^{N} U_{3\_body}(i, j, k, r_i, r_j, r_k) \\
& + \sum_{i=1}^{N-1} \sum_{j>i}^{N} U_{Tersoff}(i, j, r_i, r_j, R^N) \\
& + \sum_{i=1}^{N-3} \sum_{j>i}^{N-2} \sum_{k>j}^{N-1} \sum_{n>k}^{N} U_{4\_body}(i, j, k, n, r_i, r_j, r_k, r_n) \\
& + \sum_{i=1}^{N} U_{Metal}(i, r_i, R^N) \\
& + \sum_{i=1}^{N} U_{extn}(i, r_i, v_i).
\end{aligned}
\tag{3.33}
$$

Here, U_{bond}, U_{angle}, U_{dihed}, U_{inv}, U_{pair}, U_{3_body}, $U_{Tersoff}$ and U_{4_body} are empirical interaction functions representing chemical bonds, valence angles, dihedral angles, inversion angles, two-body, three-body, many-body covalent, and four-body forces, respectively. U_{bond}, U_{angle}, U_{dihed}, and U_{inv} are regarded as intra-molecular interactions and U_{pair}, U_{3_body}, $U_{Tersoff}$, U_{4_body}, and U_{Metal} as inter-molecular

interactions. The final term U_{extn} represents the external potential. The vectors r_a, r_b, r_c and r_d represent the positions of the atoms involved in a given interaction and R^N is used to indicate a many-body dependence. $N_{bond}, N_{angle}, N_{dihed}$ and N_{inv} are the total numbers of these respective interactions present in the simulation system, and $i_{bond}, i_{angle}, i_{inv}$ and i_{dihed} are individual interactions of each type. Also, non-bonded pair interactions are updated using a Verlet neighbour list, which is reconstructed at intervals during the simulation.

3.2 Rheology

Rheology is the study of the flow and deformation of matter resulting from the application of a force. One of the most important rheological properties of fluids in traction applications is the viscosity, especially the shear viscosity. DCMP under pressure experiences Elastohydrodynamic Lubrication (EHL) regime and viscosity is expected to change when a shear is applied.

3.2.1 Lubrication

Friction occurs when two parts are moving relative to each other. From cogwheels to a knee joint, friction causes wear of the parts and reduces the performance by

generating heat, corrosion and inflammation. There are two types of friction: dry friction and fluid friction. Fluid friction develops between layers of fluid moving at different velocities. Fluid friction is important for the flow of fluids through pipes or dealing with bodies immersed in moving fluids. The dry friction condition is where no lubricant is used and the coefficient of friction is the highest.

Lubrication is the process to reduce the friction, hence enhancing performance and lifetime of the parts involved. Also, careful selection of lubricants can control the surface property as well. Either solids or fluids can be used as lubricants.

3.2.2 Different regimes of lubrication

Depending on the geometry of the surface and the distance between the surfaces, different types of lubrication can occur. Figure 3.8 shows the Stribeck curve used in tribology. This figure shows the transition of the lubricating regimes of the sliding surfaces. The vertical axis represents the coefficient of friction and the horizontal axis the bearing characteristic number, which is $\eta V/P$, where η is shear viscosity, V sliding speed, and P average surface pressure. As the bearing characteristic number increases, the lubrication type moves from boundary lubrication to hydrodynamic lubrication via the mixed regime.

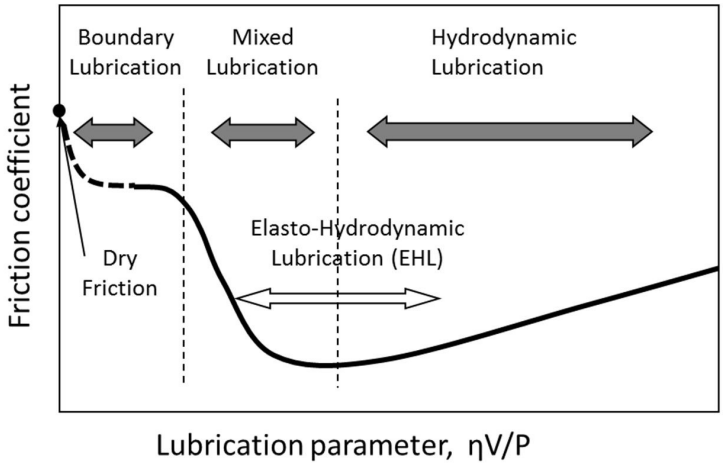

Figure 3.8: Schematic of the Stribeck curve showing lubrication regimes.[69] η is the fluid viscosity, V is the relative speed of the surfaces, and P is the pressure applied on the interface.

Boundary lubrication

Boundary lubrication occurs when a liquid is under conditions where the solid surfaces are so close together that contact between two is almost possible.[70] The friction and wear in boundary condition are determined predominantly by interaction between the solids and between the solids and the liquid. The bulk properties of the liquid are less relevant in the friction and wear behaviour, and properties of solid plays a bigger role. Typically, lubricant films of less than 100 nm are formed. This film layer lies between surfaces in the contact area to control the adhesion between solid interfaces and to reduce the resistance, and so to decrease the coefficient of friction. Synovial joints, teeth-saliva during chewing, and the start up and shut down period of engines are examples of boundary lubrication.

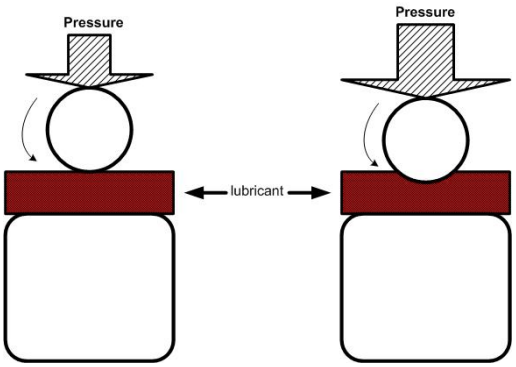

Figure 3.9: An example diagram of hydrodynamic lubrication.

In the mixed lubrication regime, the fluid film bears a portion of friction and the coefficient of friction decreases further. In boundary lubrication and mixed lubrication, a film adsorption layer must be formed on the sliding surfaces to reduce the friction.

Hydrodynamic Lubrication

Hydrodynamic lubrication, also called full film lubrication, occurs when two surfaces sliding relative to each other are fully separated by a film of fluid, as in a system like Figure 3.9. In this case, the fluid film bears the entire load and the contact area disappears. Friction force is due only to the viscous resistance of the fluid. This means the coefficient of friction reduced to its minimum. However, the viscosity of fluid and sliding speed now increase the bearing characteristic number and also the coefficient of friction. In hydrodynamic lubrication, a thick layer of

film must exist and bear some load even under high pressure and low speed. As a result, the lubricant characteristics of the fluid becomes more important.

Elastohydrodynamic Lubrication

When two surfaces roll, slide or spin relative to each other, the lubricant will be dragged along due to the shear stress exerted on it. In the contact zone, the hydrodynamic pressure developed in the lubricant causes a further increase in viscosity that is sufficient to separate the surfaces. Because of this high viscosity and the short time required to carry the lubricant through the contact area, the lubricant cannot escape and the surfaces will remain separated. The film thickness will not be affected by pressure because, under the usual pressure to which this type of lubricants is exposed, the lubricant film is harder than the metal surfaces. Therefore, increasing the pressure or load will result in deformation of the metal surface and increase of the contact area, as shown in Figure 3.10. This lubrication mechanism is called elastohydrohynamic lubrication (EHL). EHL is dominant where the external load on a unit is larger than the stiffness of the material of the moving parts and the contacting surface do not fit well; in other words, the surfaces are non-conformal.[71] Such a load is typically applied and removed in hundreds of microseconds.

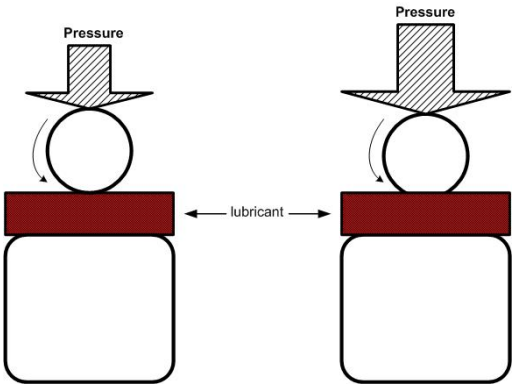

Figure 3.10: An example diagram of elastohydrodynamic lubrication (EHL).

EHL can be divided into two types: hard or soft. Hard EHL is observed with materials of high elastic modulus such as metals. Up to 3 - 4 GPa of pressure is exerted and a minimum film thickness of 0.1 - 1 μm occurs, but elastic deformation can be several orders of magnitude higher than the film thickness. The film thickness depends on the applied load, surface moving speed, surface geometry, elasticity of the surface material, and pressure-viscosity coefficient. Viscosity of the lubricant can be ten orders of magnitude higher than viscosity at ambient pressure. Examples of hard EHL are gears, rolling element bearing, continuously variable speed drives, etc. With materials of low elastic modulus, such as rubber or plastic, soft EHL occurs. Elastic deformation occurs under even light load of up to 1 MPa. The viscosity of the lubricant is not affected by this low pressure, and pressure-viscosity coefficient is not as significant. The minimum film thickness is about 1 μm. Examples of soft EHL are seals, tyres, gaskets, etc.

The friction in an EHL contact is largely determined by high pressure behaviour. Therefore it is important to know properties of the lubricant at high pressure.

3.2.3 Viscosity

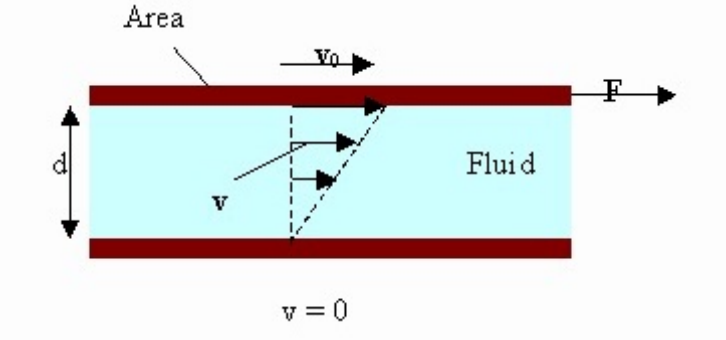

Figure 3.11: A flow of a viscous fluid.

Consider a fluid between two flat surfaces, one moving at velocity v_0 relative to the other surface as shown in Figure 3.11. The shear stress τ is the ratio of the force acting on one surface, F, and the surface area, A. Also, shear stress is related to the velocity of the moving surface and the separation between the two surfaces, d, with a coefficient μ. This coefficient is the viscosity of the fluid. The molecules close to the top surface will tend to move with that surface, moving at a velocity v_0, while the molecules close to the bottom (stationary) surface will tend to stay with the stationary surface. There are short-range attractive intermolecular forces which then create a velocity gradient along the separation distance. Shear

viscosity is a measure of fluid's resistance to this flow. This relation is expressed in Equation (3.34), the negative sign indicating this is resistance.

$$\tau = \frac{F}{A} = -\mu \frac{v_0}{d}. \tag{3.34}$$

Temperature dependence of viscosity

The viscosity of a liquid can change with temperature and there are a few models for the temperature dependence of shear viscosity. The Arrhenius equation shows the temperature dependence of reaction rates. For fluids following this equation, the temperature dependence of viscosity also can be expressed using the Arrhenius relation:

$$\eta(T) = \eta_0 \ \exp^{\left(\frac{E}{RT}\right)}, \tag{3.35}$$

where viscosity η is dependent on the viscosity at a reference temperature η_0, activation energy E, and temperature T. R is the gas constant.

Also, another well known viscosity model is the Vogel-Fulcher-Tammann (VFT) model.[72]

$$\log_{10} \ \eta(T,x) = \log_{10} \ \eta_\infty(x) + \frac{A(x)}{T - T_0(x)}, \tag{3.36}$$

where T is temperature, x is composition, and three VFT parameters (η_∞, A, and T_0) are obtained from fitting the experimental measurements. Equation (3.36) is also known as the Williams-Landel-Ferry (WLF) equation. Although this model works reasonably well for a variety of liquids, it tends to break down at low temperature.

The Avramov-Milchev (AM) equation also relates the viscosity to temperature.[73]

$$\log_{10}\eta(T,x) = \log_{10}\ \eta_\infty(x) + \left(\frac{\tau(x)}{T}\right)^{\alpha(x)}, \tag{3.37}$$

where η_∞, τ, and α are fitting parameters.

Pressure dependence of viscosity

The shear viscosity can also change with pressure, and relations between viscosity and pressure can be expressed using the Barus equation.[43]

$$\eta = \eta_0\ \exp^{\alpha P}, \tag{3.38}$$

where η_0 is the viscosity at 0.1 MPa and α is the pressure-viscosity coefficient. Although this equation has been used extensively in the EHL research, it works reasonably well only at pressures up to about 500 MPa. One of the most widely

used alternatives is the equation by Roelands, which is said to be valid up to 1 GPa.[74]

$$\eta_R = \eta_0 \ \exp^{\alpha^* P}, \tag{3.39}$$

where

$$\alpha^* \ P = [\ln(\eta_0) + 9.67] \left\{ \left(\frac{T - 138}{T_0 - 138} \right)^{-S_0} \times (1 + 5.1 \times 10^{-9} P)^Z - 1 \right\}, \tag{3.40}$$

where T_0 is a reference or ambient temperature. The Roelands pressure-viscosity coefficient, α^*, is a function of both pressure P and temperature T. The dimensionless constant Z is,

$$Z = \frac{\alpha}{5.1 \times 10^{-9} (\ln \eta_0 + 9.67)}, \tag{3.41}$$

where α is the pressure-viscosity coefficient of the Barus equation (Equation (3.38)).

3.2.4 Non-Newtonian fluids

Fluids can be categorised into two types depending on its response to the external force. Liquids, where the viscosity is a constant regardless of the shear rate are called Newtonian fluids. If the viscosity changes with the change of shear rate, the fluid is a non-Newtonian fluid. Fluids showing shear thickening (or dilatant) and

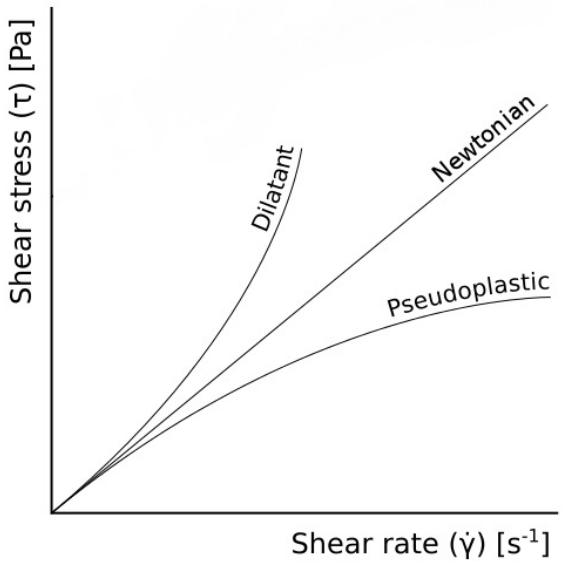

Figure 3.12: Examples of non-Newtonian behaviour.

shear thinning (or pseudoplastic) response presented in Figure 3.12 are of shear-rate dependant non-Newtonian fluids. Shear thinning fluids become less viscous with increased shear rate and these are more common and the most important class of non-Newtonian fluids.[75] Ketchup and paints are two of everyday examples. By controlling its viscosity response, its spread and flow can be manipulated. Therefore, non-Newtonian fluids have more scope for industrial applications.[76]

3.3 Analysis methods

3.3.1 Radial distribution function

The radial distribution function (RDF) is used to see how the atoms in a system are distributed. The RDF is a useful way to describe the average structure of a molecular fluid system. The RDF is the probability of finding another particle at a certain distance from the reference molecule. A schematic diagram of 2-D case is shown in Figure 3.13. The probability of finding a blue particle between the distance (r) and ($r + \Delta r$) from the red particle can be expressed by the RDF.

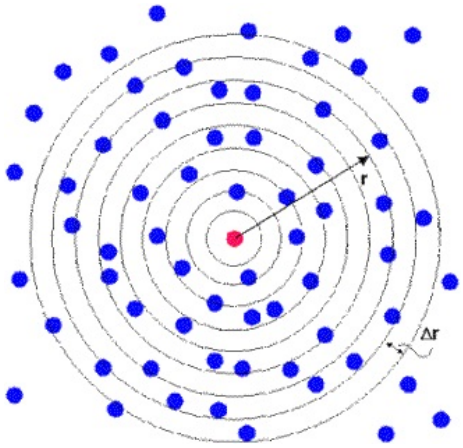

Figure 3.13: Calculating the radial distribution function (RDF).[77]

In this study, the RDF of the centres of the mass of the molecule was used to measure how the molecules are distributed. The RDF for the 3-D case is calculated

as Equation (3.42).

$$g(r) = \frac{n(r)}{\frac{4}{3}\pi((r+\Delta r)^3 - r^3)\rho}, \tag{3.42}$$

where $g(r)$ is the RDF, $n(r)$ is the number of molecules in the volume between the distance from the centre of the mass of the reference molecule, r and the width of shell Δr, and ρ is the number density of the system defined as total number of the molecules in the system divided by the total volume of the simulation system. This distribution is averaged over all the particles in the simulation system and over the simulation times.

3.3.2 Radius of gyration

Viscosity of fluids was estimated using the Stokes-Einstein relation (Section 3.3.4). According to the Stokes-Einstein relation (Equation (3.49)), viscosity of a spherical particle of the radius a can be described as,

$$\eta = \frac{k_B T}{6\pi \mathrm{D} a},$$

where k_B is Boltzmann constant, T is temperature and D is diffusion coefficient of the particle. The radius of gyration of the molecules r_g was used in place of the

radius.

Radius of gyration (R_g) is the radius of a thin hollow sphere whose mass and moment of inertia are the same as the particle of interest.[78] This length is often used as a measure of the size of large molecules such as in polymers and DNA. It is defined as,

$$R_g^2 = \frac{1}{N}\sum_{i=1}^{N}(r_i - r_{COM})^2, \tag{3.43}$$

where r_i is the distance of atom i from the centre of mass (COM) of the molecule which the atom is a part of. Moment of inertia, I, can be defined as

$$I = \sum_i m_i r_i^2, \tag{3.44}$$

where m_i is the mass of atom i and the r_i the distance of atom i from the centre of mass.

As shown in Figure 3.14, the radius of gyration for the same molecule changes depending on how spread a molecule is. The top one will have the largest R_g and the bottom one the smallest.

Moment of inertia can tell how symmetrical an object is. The moment of inertia along one axis, say x, is smaller than the values along the other axes when the shape of the object is elongated along the $x-$axis.

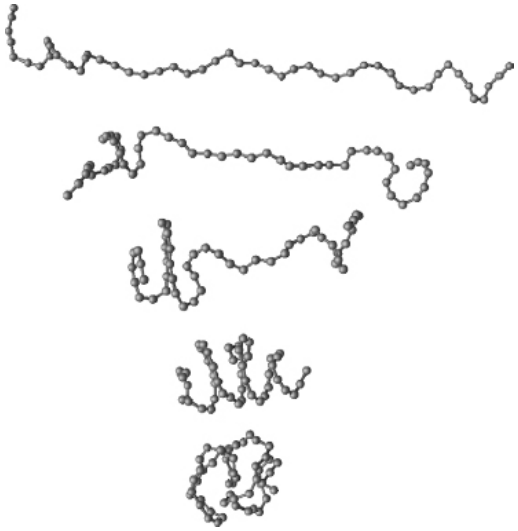

Figure 3.14: Radius of gyration, R_g, becomes smaller from top to bottom.

3.3.3 Diffusion coefficient

Diffusion is caused by the molecular motion of the particles in the liquid. The macroscopic law describing diffusion is Fick's law,

$$\mathbf{j} = -D\nabla c, \tag{3.45}$$

which tells the flux, $\mathbf{j}$, of the diffusion particles is proportional to the negative gradient in the concentration of those particles. The coefficient D is the diffusion coefficient.

At the molecular level, diffusion coefficients can be expressed as Equation (3.46).

$$D = \frac{1}{3}\int_0^\infty dt \langle \mathbf{v}_i(t) \cdot \mathbf{v}_i(0) \rangle, \tag{3.46}$$

where $\mathbf{v}_i$ is the centre of mass velocity of a molecule i.

At a long time, it becomes Equation (3.47).

$$\langle |r(t) - r(0)|^2 \rangle = 6Dt + C, \tag{3.47}$$

where the left-hand side is mean squared displacement of the molecules, D the diffusion coefficient, t the time elapsed, and C a constant.

Molecules in a dense fluid moves constantly, and they collide with other molecules and change their paths and end up in a random walk. This walk is proportional to the time elapsed. Equation (3.47) shows this relationship. Therefore, the diffusion constant is estimated from the gradient of mean squared displacement (MSD) of particles of the system.

3.3.4 Stokes-Einstein relation

The relation between molecular movement and diffusion in a liquid can be expressed by Equation (3.48) shown by Einstein.

$$D = \mu k_B T, \tag{3.48}$$

where D is the diffusion constant and $\mu = v_d/F$ is the 'mobility' of the particle.

Combined with Stokes' law, viscosity of a spherical particle, η, can be estimated using,

$$\eta = \frac{k_B T}{6\pi D a}, \tag{3.49}$$

where k_B is Boltzmann constant, T temperature in K, D diffusion coefficient, and a the radius of the spherical particle.

Chapter 4

SIMULATION DETAILS

Simulations in this project use the united-atom model where hydrogens are incorporated in carbon sites. The united-atom model reduces computational cost and is able to capture the temperature dependence and pressure dependence well.[31–34] DCMP and other C_{18} alkanes are presented in the UA-model. Simulation details and preliminary results are presented in this chapter.

4.1 Molecules used in the study

4.1.1 DCMP

2,4-Dicyclohexyl-2-methylpentane (DCMP) is a nonpolar hydrocarbon, which is commonly used in traction lubrication.[79] Having two cycloheyl rings connected by three carbon chain and three methyl side chains on the two of these three carbons, DCMP is expected to be a stiff molecule. It has a higher viscosity than other alkanes of a similar molecular weight. It is a clear colourless liquid at room temperature with a melting point of -30 °C, a boiling point of 112 °C, and a molecular weight of 250.46 g/mol. A molecular structure of DCMP is presented in Figure 4.1. In the UA model, DCMP is represented with CH_3, CH_2, CH and C carbon types with adjusted molecular weight.

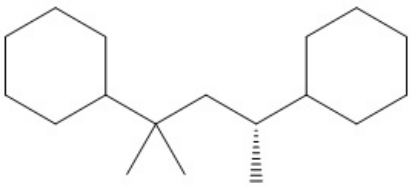

Figure 4.1: A representation of 2,4-Dicyclohexyl-2-methylpentane (DCMP). DCMP is characterised by two cyclohexyl rings and three methyl hooks.

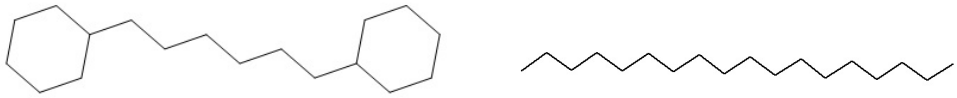

(a) (b)

Figure 4.2: Representations of comparison molecules used in this study. (a) 1,6-dicyclohexylhexane (Dumbbell) and (b) octadecane (Linear). 1,6-dicyclohexylhexane is chosen for not having methyl groups and octadecane is chosen for not having cyclohexyl rings.

4.1.2 Comparison motifs

Having defined the characteristic features of DCMP to be cyclohexyl rings and methyl hooks, two 18-carbon alkanes, *i.e.* 1,6-dicyclohexylhexane (Dumbbell) and octadecane (Linear) were chosen for comparison. Dumbbell is a $C_{18}H_{34}$ molecule that has two cyclohexyl rings linked by a hexane backbone as shown in Figure 4.2(a). It has CH_2, and CH carbon types in terms of the UA model. Dumbbell has cyclohexyl rings, similar to DCMP, but no methyl hooks. A linear alkane, octadecane ($C_{18}H_{38}$), shown in Figure 4.2(b), does not have cyclohexyl rings nor methyl hooks in the backbone. In the UA model, it is represented using CH_3-type carbons and CH_2 carbons.

4.1.3 Physical properties

Selected physical properties of DCMP, linear, and dumbbell molecules are presented in Table 4.1.

Table 4.1: Selected physical properties of DCMP, Dumbbell, and Linear. † are taken from Yaws,[80] and * are from ChemSpider[81–83] (predicted).

Name	DCMP $C_{18}H_{34}$	Dumbbell $C_{18}H_{34}$	Linear $C_{18}H_{38}$
Average Mass, g/mol	250.468†	250.463*	254.500†
Molar Volume, cm^3	286.2±3.0*	292.5±3.0*	325.7±3.0*
Melting Point, K	303.15*	N/A	301.15-303.35*
Boiling Point, K	601.75†	613.45±9.0*	589.30*

4.2 Simulation details

A series of MD simulations were performed for three C_{18} alkane molecules (DCMP, Dumbbell, and Linear) at 300 K under various pressure conditions ranging from 1 atm to 10 000 atm using DL_POLY[66]. The DCMP molecule contains 18 atoms of united-atom (UA) carbons. First, a simulation box of 1000 DCMP molecules at 1 atm was created. NPT simulations were performed for 2500 ps at 300 K. This is to give enough time for DCMP molecules to relax from the initial conditions. High pressure cases were prepared by gradually increasing the pressure from a set of configurations during simulations of lower pressure systems; in each case,

Table 4.2: Simulation parameters used in the current molecular simulation study.

Δt	cut-off radius	temperature	number of molecules
10^{-15} sec	3.5σ	300 K	1000

a system with pressure no more than 10 times lower than the target pressure was used. Pressures studied were 1, 3, 10, 30, 100, 300, 1000, 3000, and 10 000 atm.

In addition, to ensure the independence to the initial condition, the molecules were heated to 1000 K for 1000 ps to obtain an equilibrated ensemble, then further simulated at 300 K for 3000 ps. The same procedures of heating up and cooling down were repeated for the systems under each pressure to achieve the equilibrium. Dumbbell and Linear molecules at various pressure conditions were prepared in the same way as DCMP.

To show the effect of pressurising speed, comparison between before and after the heat treatment was made and thermodynamical analysis of these molecules are presented in the following sections.

4.2.1 Simulation parameters

CHARMM force field was used for UA carbon atoms. Parameters for united atoms were prepared to use in DL_POLY Classics using DL_FIELD.[84]

Bond potentials

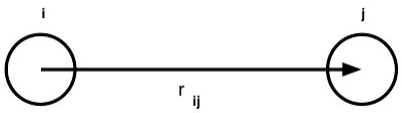

Figure 4.3: Schematic diagram of the interatomic bond vector within a molecule.[66] Atoms i and j are bonded at a length r_{ij}.

Table 4.3: Harmonic bond parameters used in Equation (4.1).

atom i	atom j	k /Å^{-2}	r_0 /Å
CT	CH1E	536	1.53
CT	CH2E	536	1.53
CT	CH3E	480	1.54
CH1E	CH1E	536	1.53
CH1E	CH2E	536	1.53
CH1E	CH3E	536	1.53
CH2E	CH2E	536	1.53
CH2E	CH3E	536	1.53

Figure 4.3 shows the atom-atom bond potential within a molecule. This bond was modelled using a harmonic potential as represented in Equation (4.1).

$$U_{bond}(r_{ij}) = \frac{1}{2}k\,(r_{ij} - r_0)^2, \tag{4.1}$$

where r_{ij} is the distance between atom i and atom j. Four types of UA carbon atoms are used in the simulations and the parameters k and r_0 of Equation (4.1) for these atom types are presented in Table 4.3.

Valence angle potentials

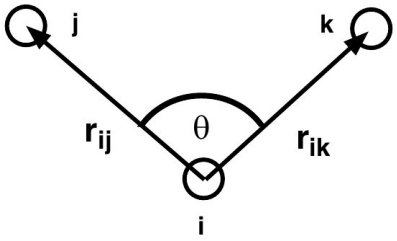

Figure 4.4: Schematic diagram of the valance angle.[66] Vector r_{ij} of atoms i and j and vector r_{ik} of atoms i and k form valence angle θ.

Table 4.4: Valence angle parameters used in Equation (4.2).

atom i	atom j	atom k	k /° $^{-2}$	θ_0 /°
CH1E	CT	CH2E	90	112.5
CH1E	CT	CH3E	90	112.5
CH2E	CT	CH3E	100	112.5
CH3E	CT	CH3E	100	112.5
CH1E	CH1E	CH2E	90	110.3
CH1E	CH1E	CH3E	90	110.3
CH2E	CH1E	CT	100	112.5
CH2E	CH1E	CH1E	90	110.3
CH2E	CH1E	CH2E	100	112.5
CH2E	CH1E	CH3E	100	112.5
CT	CH2E	CH2E	142	112.4
CH1E	CH2E	CH2E	90	112.5
CH2E	CH2E	CH2E	100	112.5

The potential caused by three atoms as presented in Figure 4.4 are modelled by Equation (4.2) and the parameters in Table 4.4.

$$U_{angle}(\theta_{jik}) = \frac{k}{2}(\theta_{jik} - \theta_0)^2. \tag{4.2}$$

Dihedral angle potentials

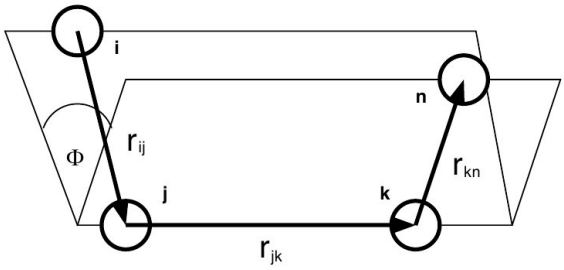

Figure 4.5: The dihedral angle and associated vectors.[66]

Four-atoms dihedral potentials as shown in Figure 4.5 are modelled by a cosine potential as in Equation (4.3).

$$U_{dih}(\phi_{ijkn}) = A[1 + \cos(m\phi_{ijkn} - \delta)]. \tag{4.3}$$

The intermolecular potentials

$$U(r_{ij}) = 4\varepsilon \left[\left(\frac{\sigma}{r_{ij}} \right)^{12} - \left(\frac{\sigma}{r_{ij}} \right)^{6} \right]. \tag{4.4}$$

The Lennard-Jones potential was used for a short ranged (van der Waals) potential as in Equation (4.4). The parameters used in the simulations are tabulated in Table 4.5.

Table 4.5: Parameters used for the intermolecular potential.

Molecule 1	Molecule 2	ε /kcal/mol	σ/ Å
CH2E	CH2E	0.11420	3.98232
CH2E	CH1E	0.07450	4.00904
CH2E	CT	0.10155	3.59478
CH2E	CH3E	0.14381	3.91995
CH1E	CH1E	0.04860	4.03577
CH1E	CT	0.06625	3.62150
CH1E	CH3E	0.09382	3.94668
CT	CT	0.09030	3.20724
CT	CH3E	0.12788	3.53241
CH3E	CH3E	0.18110	3.85759

4.2.2 Time step

A system was used to decide suitable time step for main simulations. The choice of an appropriate timestep is more problematical than usual in this study due to the interest in very high pressures. Under very high pressures, the intermolecular forces become potentially very large. Initially, the time step of 1 fs was suggested for the carbon-only united atoms model. To verify that this was adequate, time steps of 0.1 fs, 0.5 fs, 1 fs, 2 fs and 5 fs were also tested. Constant energy - NVE ensemble simulations at the temperature of 300 K and a pressure of 1000 bar (108 Pa) for each time step were carried out to see the effect of time step. Each of these simulations was run for 2 ps at different time steps, *i.e.* for 20 000 steps at 0.1 fs time step, for 2000 steps at 1 fs, etc.

The relative root-mean-square (RMS) fluctuation ($\sigma E/NkT$) in total energy

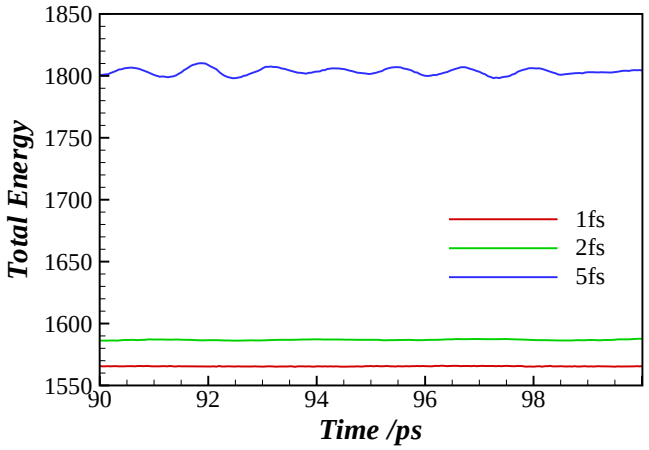

Figure 4.6: A selection of fluctuations of total energy using different time steps. Energy is in kcal/mol and time in ps.

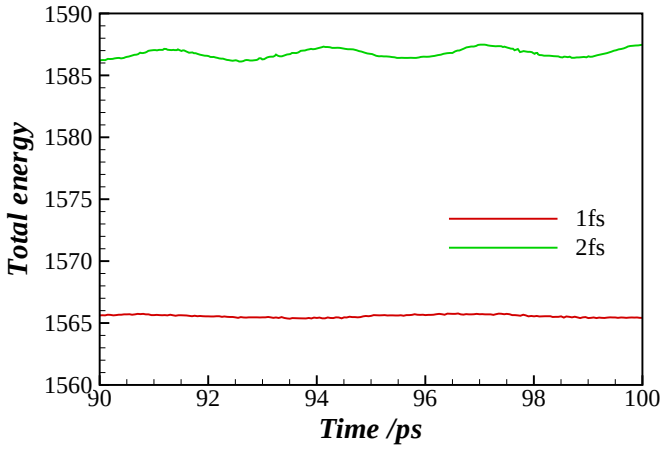

Figure 4.7: Fluctuations of total energy with time steps of 1 fs and 2 fs are compared. Energy is in kcal/mol and time in ps.

for each simulation was compared in Figures 4.6 and 4.7. It is clear from the graph that 5 fs time step simulation fluctuates significantly more than other simulations. Generally, the relative RMS fluctuation less than the order of 10^{-4} is considered

Table 4.6: Deviation of energy; σ_E is standard deviation of the energy, N is the degree of freedom of the system, k_B is the Boltzmann constant and T is temperature.

Time step, Δt (fs)	σ_E/Nk_BT
0.1	8.329203×10^{-7}
0.5	1.741253×10^{-5}
1.0	4.418547×10^{-5}
2.0	1.762422×10^{-4}
5.0	2.907099×10^{-4}

acceptable.[62,85] In this respect, 5 fs time step is not suitable. 2 fs simulation has the relative RMS fluctuation of 1.76×10^{-4}, and so of marginal validity. Other standard deviations of the energy shown in Table 4.6 are smaller than the acceptable level. 1.0 fs time step was therefore chosen for the further calculations.

Two smaller time step simulations were presented in Figure 4.7. The fluctuation in 0.1 fs simulation is negligible from the graph. It is presented as a straight line. In fact, its relative RMS fluctuation is in the order of 10^{-7}, whereas the relative RMS fluctuation of 1.0 fs time step simulation is 4.42×10^{-5}. This test shows that 1.0 fs time step is acceptable for the united-atom carbon model simulation. Smaller time steps are not expected to give any better calculation result than this time step, although they take much longer time to calculate.

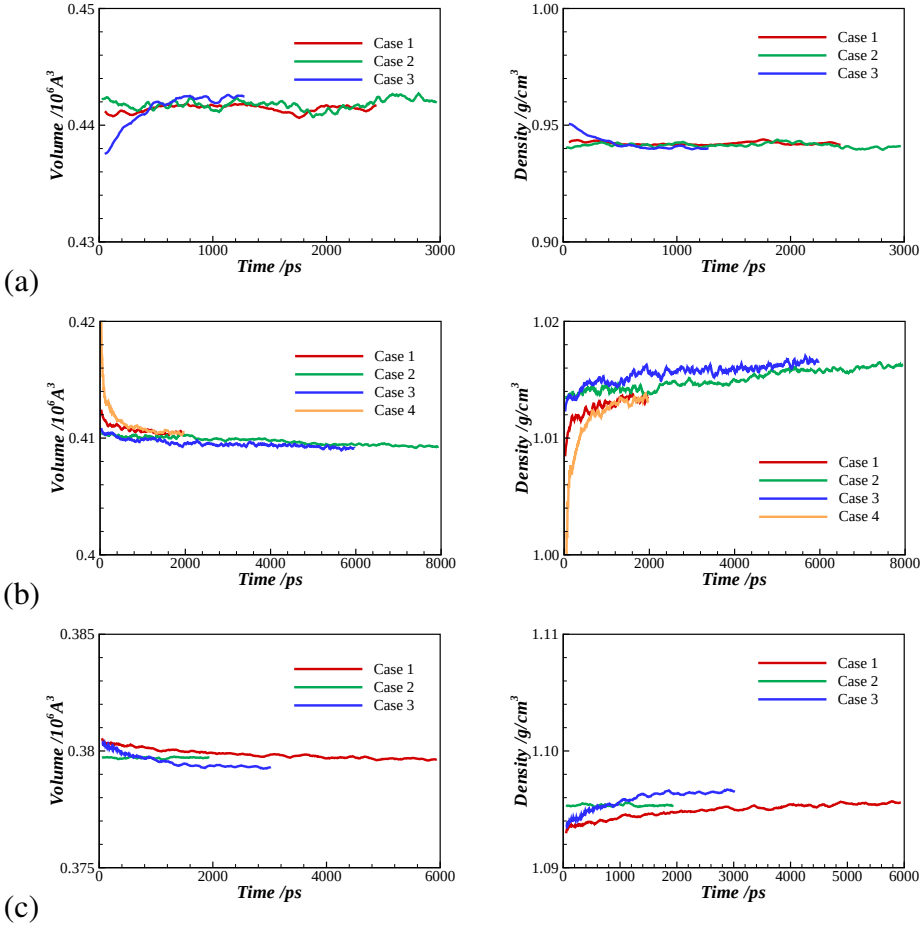

Figure 4.8: Time evolutions of volume (left) and density (right) for DCMP at 300 K for three pressures (a) 1 atm, (b) 3000 atm, and (c) 10 000 atm. All cases in the graph were run at the same pressure but with different initial conditions and history. Volume is in 10^6 Å^3, density in g/cm^3, and pressure in atm.

4.2.3 Time evolution of simulations

Examples of time evolution of the volume and density of the simulation system are presented in Figure 4.8. These plots show how the volume and also the density evolve during NPT simulations at 300 K. Three pressure conditions are shown

here: (a) 1 atm, (b) 3000 atm, and (c) 10 000 atm. Each plot has a different history; for example, 1 atm Case 1 was equilibrated at 300 K, while Case 2 was heated to 1000 K for a short time and cooled to 300 K. Case 3 was started from 10 000 atm. All three cases converge to the same volume and density regardless of the previous history. The variation between different cases is rather small and the difference is less than 0.5%. At 10 000 atm, the variaton is even smaller and the difference is less than 0.2%. It appears that a longer time is taken for the volume to converge at the higher pressure. Figure 4.8 shows that the volume from simulations with different histories converges to the same values. At 1 atm, volumes of the three cases converged after 1200 ps. It took more than 2000 ps at 3000 atm and 3000 ps at 10 000 atm.

The volume and density changes for DCMP, Dumbbell, and Linear as the simulations evolved are shown in Figure 4.9. The variations of volume during NPT simulations are relatively small and the effect of pressure on volume and density is clearly discernible. As expected, at large pressures (1000 atm, 3000 atm, and 10 000 atm), changes in volume and density are significant. 10 000 atm (blue) and 3 000 atm (green) cases are prominent in all graphes. Blue lines consistently show low volume high pressure for all three molecule types, then green lines of 3000 atm follow.

The RDFs for three molecular motifs are presented in Figure 4.10 at the high-

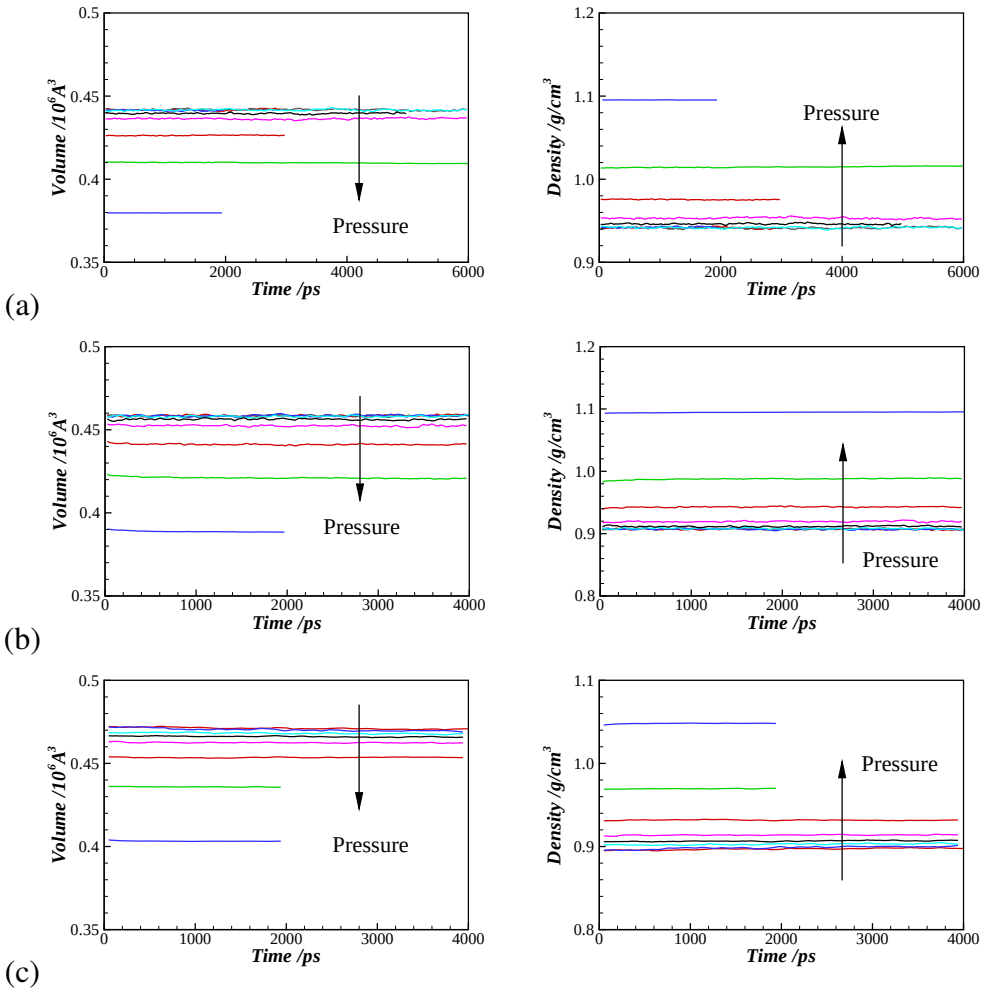

Figure 4.9: Time evolution of volume and density at various pressures. (a) DCMP, (b) Dumbbell, and (c) Linear. Volume is in 10^6 Å^3, density in g/cm^3, and pressure in atm. The arrows indicate increasing pressure.

est and the lowest pressures. RDFs are calculated over all molecule pairs in the simulation box and averaged over time. The thick red lines are time-averaged RDF profiles and the other thin lines on the background are instantaneous RDF profiles. Figure 4.10(a) shows the RDF of DCMP at 1 atm (left) and at 10 000 atm

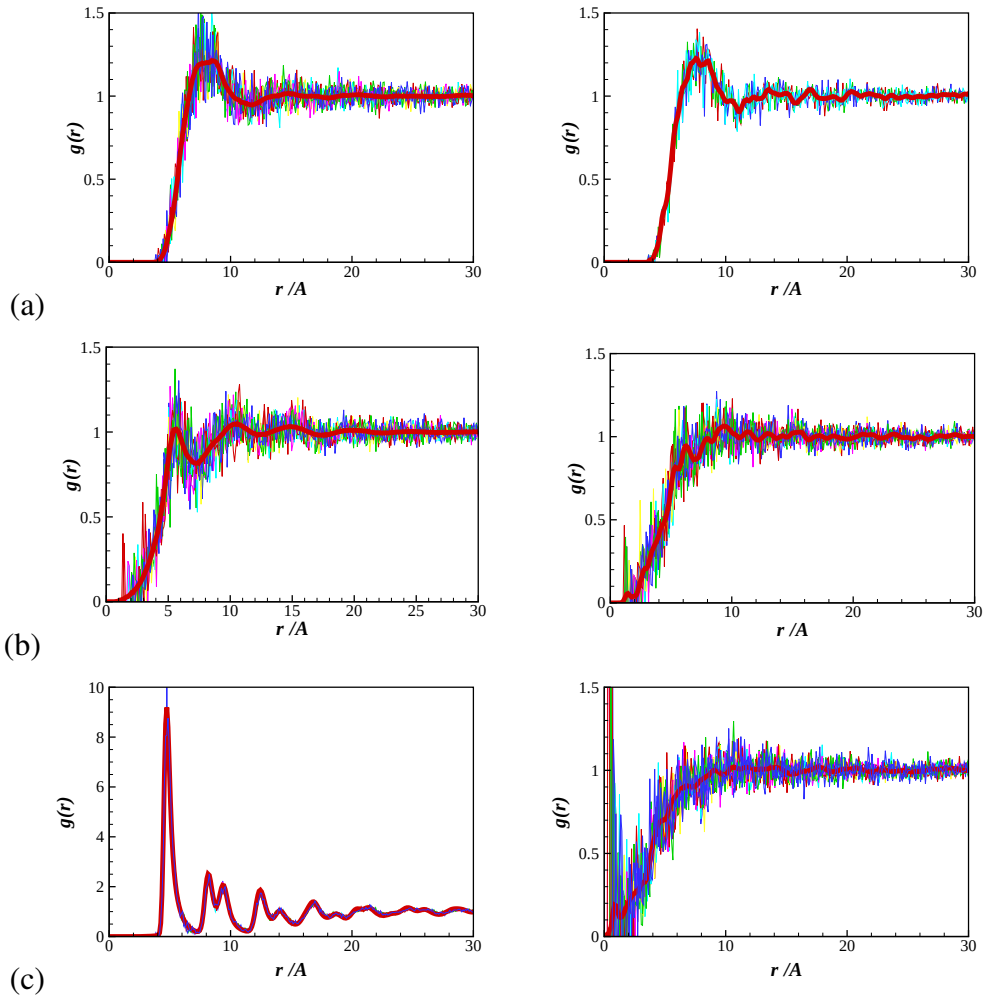

Figure 4.10: Radial distribution at 1 atm (left) and 10 000 atm (right). The thin lines are $g(r)$ of instantaneous data, and thick lines are the time-averaged $g(r)$. (a) DCMP, (b) Dumbbell, and (c) Linear. Inter-molecular centre of mass distance, r, is in Å.

(right). For small r values, $g(r)$ remains to be zero, indicating that the minimum distance between two DCMP molecules is $r \approx 4$ Å. DCMP at 1 atm has the first RDF peak at around $r = 8$ Å, and this is a broad peak with a width of 2 Å. The

first trough appears near $r = 11$ Å. Then there are signs of the second and third peaks but they are not very pronounced and converge to $g(r) = 1$ as expected from an equilibrated liquid. DCMP at 10 000 atm shows broadly a similar trend as in DCMP at 1 atm but with a noisier time-averaged RDF profile. The location of the first local maximum point is similar to that of DCMP at 1 atm, but it seems that there are two peaks rather than a broad single peak. Instantaneous RDF profiles show a lower level of fluctuations around the time-averaged RDF at higher pressures. The RDF eventually converges to $g(r) = 1$, which is the bulk average value, but the oscillations decay much more slowly.

The RDF profiles of Dumbbell at 1 atm (left) and 10 000 atm (right) are presented in Figure 4.10(b). The minimum distance for the Dumbbell molecule pairs is much smaller than that for the DCMP molecules. At 1 atm, $g(r)$ starts to increase gradually to the first peak at around $r = 6$ Å. The RDF of Dumbbell at 1 atm converges to $g(r) = 1$ at $r = 20$ Å farther out than DCMP. The RDF at 10 000 atm shows much smaller and narrower peaks and the first peak is found within $r = 2$ Å. The magnitude of peaks is small and oscillations remain quite visible for large r.

The RDF profiles of Linear at 1 atm (left) in Figure 4.10(c) shows a very strong peak at $r \approx 5$ Å, and instantaneous RDF profiles show almost no difference from the time averaged RDF profile, indicating a small level of fluctuations. In

contrast, at 10 000 atm (right), the RDF shows the largest fluctuation among all cases in Figure 4.10, especially at small r.

4.2.4 Increasing pressures

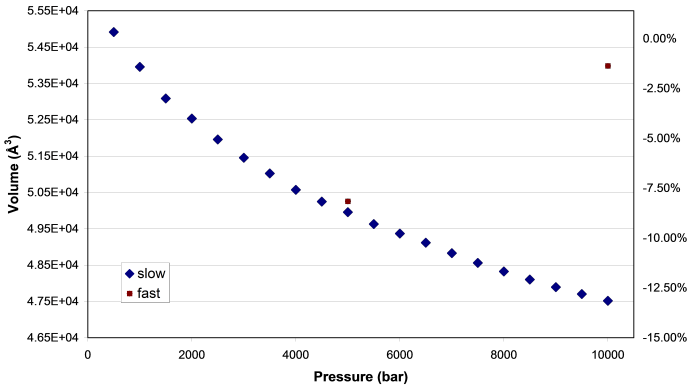

Figure 4.11: Volumes of simulation system with different path.

The systems at different density were obtained by pressurising the first equilibrium system (0.1 MPa, 300 K). High pressure conditions were achieved in two different ways: one is to increase the pressure gradually step by step (presented as blue symbols) and the other is to increase the pressure abruptly (presented as red symbols). When $P = 1$ GPa pressure is achieved, systems through two different paths had different densities as shown in Figure 4.11. It shows that increasing pressure requires more care at higher pressures.

3-D diffusion coefficients are calculated for each DCMP systems. There

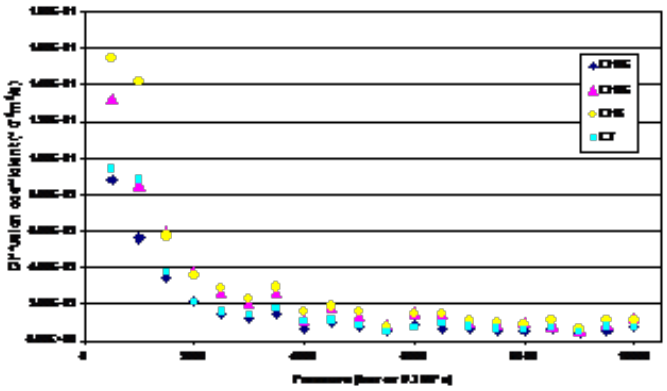

Figure 4.12: Diffusion coefficients of atom types of DCMP at different pressures. Diffusion coefficients are in 10^{-9}m^2/s and pressure in 0.1 MPa.

are four different types of carbon units; CH_1E, CH_2E, CH_3E, and CT (C). The diffusion coefficients for each types are shown in Figure 4.12. The graph shows that the diffusivity of particles reduces significantly at over 200 MPa, but not much after 500 MPa.

The RDFs of CT particles in DCMP at a range of pressures, $P = 500$ atm to $P = 10000$ atm are shown in Figure 4.13. The first peaks of $P = 5000$ atm, $P = 7500$ atm, and $P = 10000$ atm are located near $r = 6$ Å and the first peak of $P = 500$ atm is away from these peaks, near $r = 6.5$ Å. For the following peaks and troughs, the three higher pressures follow a similar trend.

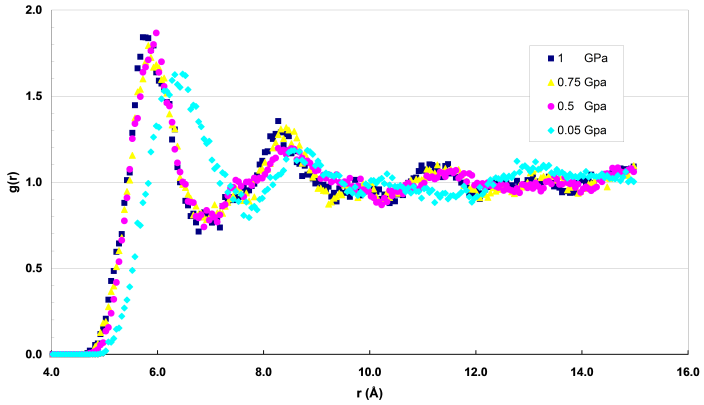

Figure 4.13: RDF of CT in DCMP molecules at different pressures. Interatomic distance r is in Å.

4.2.5 Further equilibrating

Starting configurations for each pressure case were prepared by gradually increasing the pressure from a lower value. When the target pressure was reached, each simulation system was then heated briefly to 1000 K then cooled back to 300 K. This heat treatment was to relax any residual stress within the simulation system, hence checking the quality of equilibration. The molecular structures before and after the heat treatment are compared for 1 atm and 10 000 atm.

Figure 4.14 represents the 2D-RDF contour plots of the DCMP molecule pairs as a function of centre of mass distance and relative angles between the orientations of molecules before (Figure 4.14(a)) and after (Figure 4.14(b)) the heat treatment. The heat treatment does not change the RDF contours much and

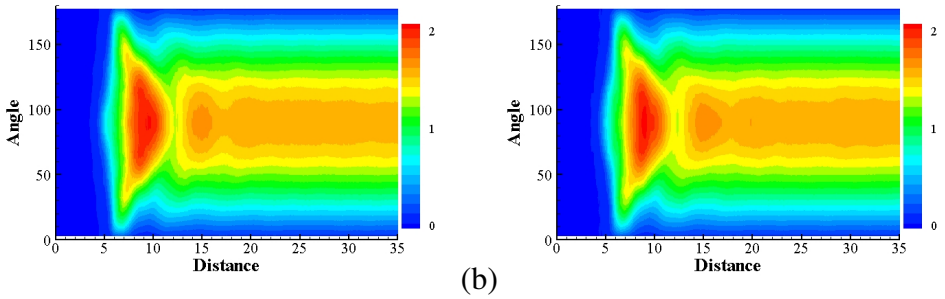

(a) (b)

Figure 4.14: Orientation of DCMP molecules at 1 atm. (a) before and (b) after the heat treatment. For heat treatment it was briefly heated to 1000 K and then simulated at 300 K. Distance is in Åand angle in degrees.

Figure 4.14 shows broadly similar characteristics before and after the heat treatment. They both have a peak at $r \approx 7$ Å, and the most populous angles lie around 90°. The highest peak (Figure 4.14(a)) is slightly lower than that after the heat treatment (Figure 4.14(b)). A small number of molecules are seen at around the distance of 12 Å and at 70°, but overall trends remain similar after the heat treatment.

Simulation results for DCMP at 10 000 atm before (left) and after (right) the heat treatment are compared in Figure 4.15. Figure 4.15(a) shows 2D contour plots of the DCMP molecule pairs as a function of centre of mass distance and relative angles between the orientations of molecules. The plot before the heat-treatment on the left shows that most populous distance for the DCMP molecule pairs is between $r = 7$ and $r = 11$ Å and they spread over a wider range of angles. At $r = 10$ Å, more pairs are found to be perpendicular to each other than parallel.

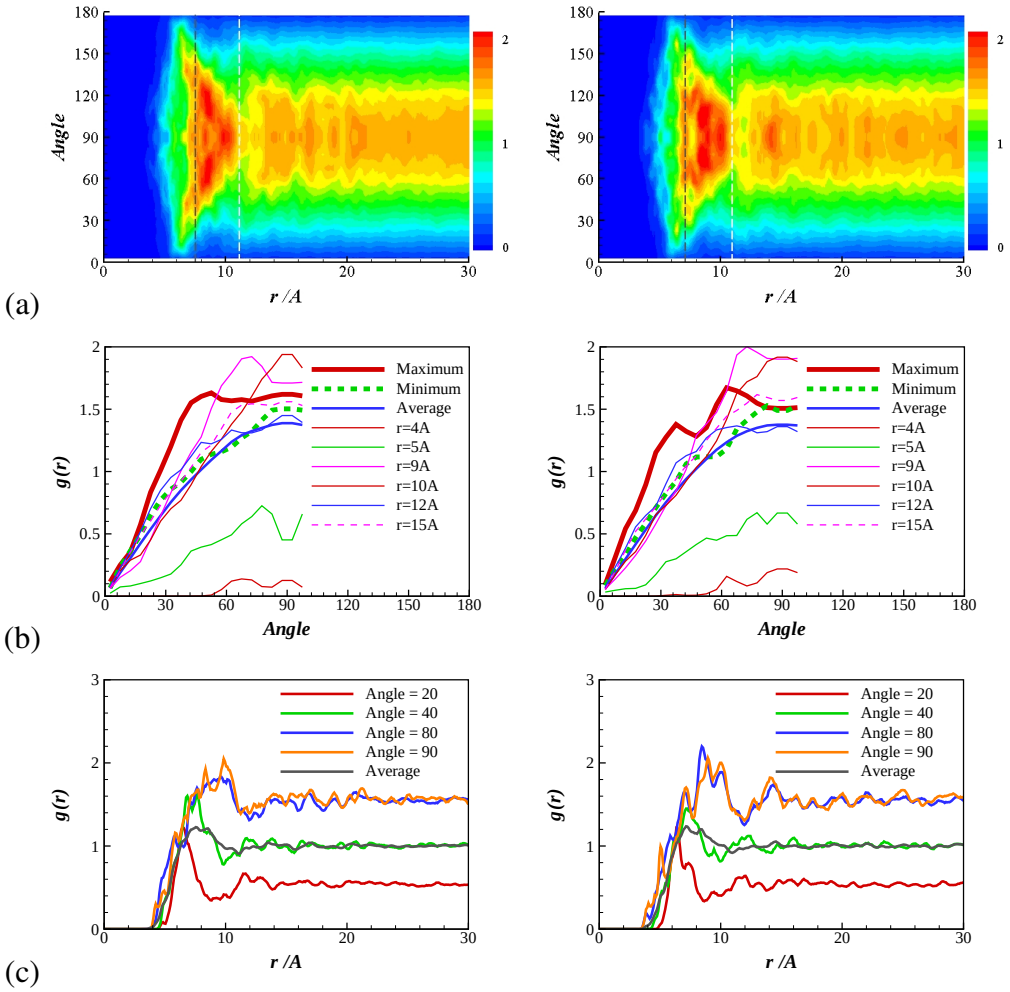

Figure 4.15: Distribution of DCMP molecule pairs at 10 000 atm. Before (left) and after (right) 'heat treatment' of (a) 2D contours, (b) distribution of angles at constant r, and (c) RDFs at constant angle are shown. Distance is in Å and angle in degrees.

There are distinctive peak patterns along the 90° axis. The position of the first trough remains at the same distance.

The distributions of molecule pair angles at a distance are shown in Fig-

ure 4.15(b). There are a small number of molecule pairs of 60° or 90° at $r = 4$ Å. Before the 'heat treatment' shown on the left, green line cut at $r = 5$ Å show low valley around 90°, whereas all the lines on the 'after' plot on the right show uniform pattern of more molecule pairs along 90°. At their most populous distances, before-plot shows the highest peak at around 45° then a plateau until 90° and after-plot has two peaks at around 30° and around 60° then a same level of plateau to 90°.

There are no DCMP pairs at closer than $r = 3$ Å for both cases shown in Figure 4.15(c). The population of pairs perpendicular to each other have the highest peak at around $r = 10$ Å and the second peak at $r = 8$ Å, whereas 'after' has the highest peak at around $r = 9$ Å and the similar sized peak at just under 10 Å. 'After' also has another significant peak near $r = 14$ Å. In the 'after' plot, 80° and 90° lines are very similar. The pair parallel to each other have the peaks at a smaller distances of $r = 6$ Å for both 'before' and 'after'.

Figure 4.16 shows 2D plots of the population of Dumbbell molecule pairs as a function of distance and angle. Same as Figure 4.15, plots on the left are before the heat treatment and on the right after. As the Dumbbell molecules do not have hindering methyl-hooks. As a result, molecules can be located closer to each other. The 2D contour plots start at a much closer distance compared to the plots for DCMP. The earliest peaks are observed around $r = 1$ Å and $\theta = 90°$. The

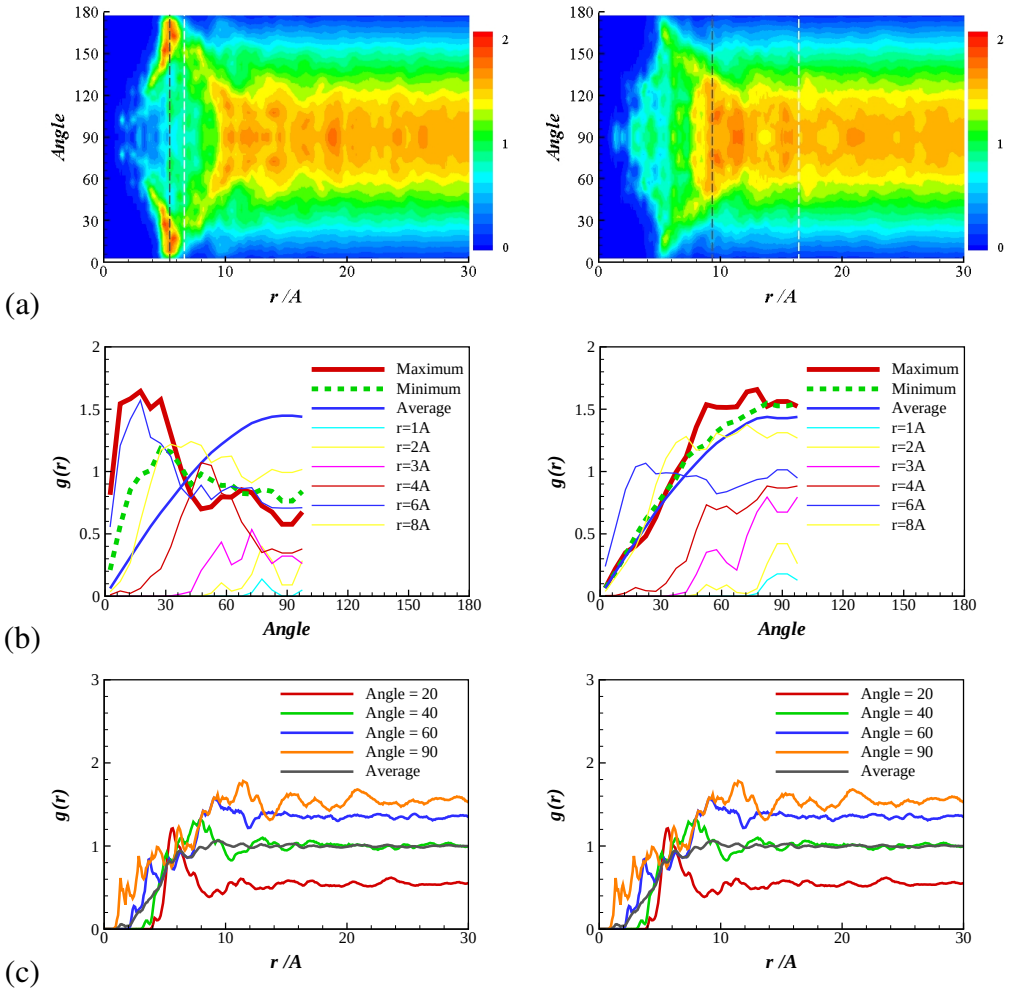

Figure 4.16: Distribution of Dumbbell molecule pairs at 10 000 atm. Before (left) and after (right) 'heat treatment' of (a) 2D contours, (b) distribution of angles at constant r, and (c) RDF at constant angle are shown. Distance is in Å and angle in degrees.

pairs parallel to each other are found between $r = 5$ Å and $r = 6$ Å on the 'before' plot, but they spread out and the red areas disappeared on the 'after' plot.

Figure 4.16(b) shows the distribution of relative angles of Dumbbell molecule

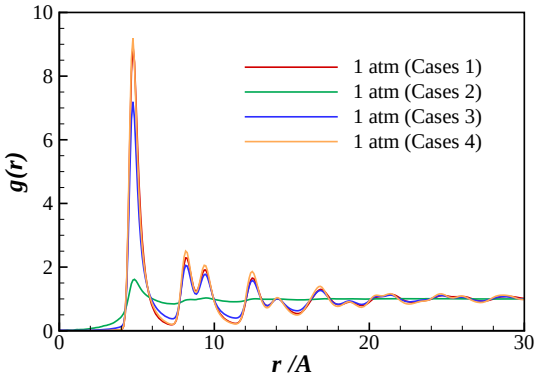

Figure 4.17: RDF of Linear at 1 atm. R_g is in Å. Case 1 was simulated at 300 K, Case 2 was 'cooling' simulation at 300 K soon after heated to 1000 atm, Cases 3 and 4 were further simulated at 300 K.

pairs. As seen in Figure 4.16(a), the 'before' plot on the left shows that there are more pairs parallel to each other compared to DCMP pairs. There are peaks near $\theta = 0^\circ$ and a trough near $\theta = 90^\circ$ on the 'before' plot. The thick red line is the angle distribution at $r = 5$ Å and the highest peak is near 15° with a much lower second peak near 70°. In the 'after' plot on the right, this trend has been shifted. Now the maximum taken from $r = 9$ Å shows that Dumbbell pairs prefer to be perpendicular to each other. For both 'before' and 'after', $\theta = 90^\circ$ is prefered at close distances of $r < 3$ Å.

The RDF profiles of Linear molecules at 1 atm are shown in Figure 4.17. Case 1 is the original simulation at 300 K. Then the system was heated to 1000 K and Case 2 was the 'cooling' of 3 ns run at 300 K. It shows a very distinctive pat-

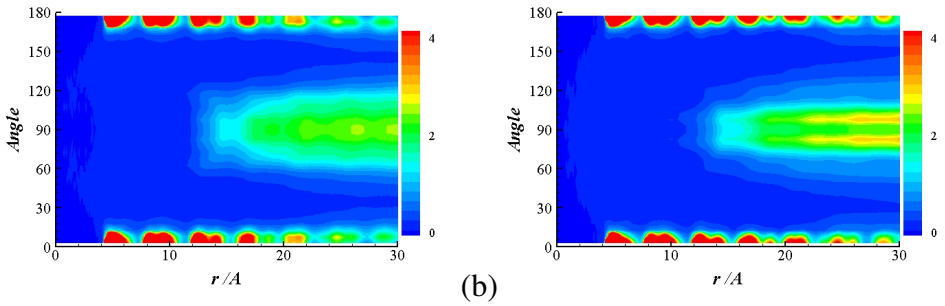

Figure 4.18: Contour maps of probability density of distance and angle between a pair of Linear molecules at 1 atm (a) before and (b) after heat treatment. Distance r is in Å and angle in degrees.

tern due to the residual energy. At the end of 3 ns run at 300 K, the configuration was used for Cases 3 and 4. The RDF plots of Cases 1, 2 and 3 are similar to each other indicating that the system was at equilibrium without the heat treatment.

2D contour plots of Linear at 1 atm in Figure 4.18 show periodic and parallel stacking of Linear molecules. Periodic peaks along 0° and 180° are observed. The peaks are strongest at close distances. After 15 Å, minor peaks along 90° are also found. Two maps are similar to each other apart from the area around 90° at $r > 20$ Å.

The RDF of Linear at 10 000 atm is shown in Figure 4.19. Case 1 started at 300 K. After 2 ns run, the system was heated to 1000 atm for 100 ps and cooled to 300 K for 100 ps. Then from this configuration Case 2 started. Case 3 started with the end configuration of Case 2 all at 300 K. The peak shown before 'heat

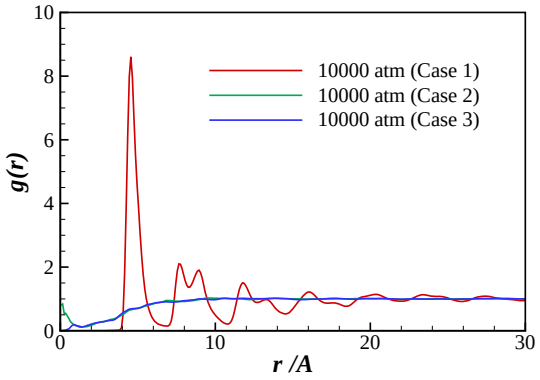

Figure 4.19: RDF of Linear at 10 000 atm. R_g is in /Å. Case 1 was simulated at 300 K, then the system was heated to 1000 K for 100 ps and cooled to 300 K for another 100 ps. Then Cases 2 and 3 were simulated at 300 K.

treatment' (Case 1) has disappeared after (Cases 2 and 3) suggesting that heat treatment is needed to achieve non-regular arrangement of Linear molecules at very high pressure.

Figure 4.20 shows 2D plots of distribution of Linear molecule pairs as a function of centre of mass distance and relative angles. The plots on the left show before the heat treatment and after the heat treatment on the right. The 'before' plots show very high concentration of parallel alignment compared to the 'after' plots on the right. On the left, the first high peaks appears at between $r = 4$ Å and $r = 6$ Å and they are close to parallel to each other. Then there is a gap of 0.5 Å, and another parallel peak at between $r = 7$ Å and $r = 10$ Å and this pattern is repeated. For $r > 12$ Å, secondary peaks of perpendicular pairs develop. In the

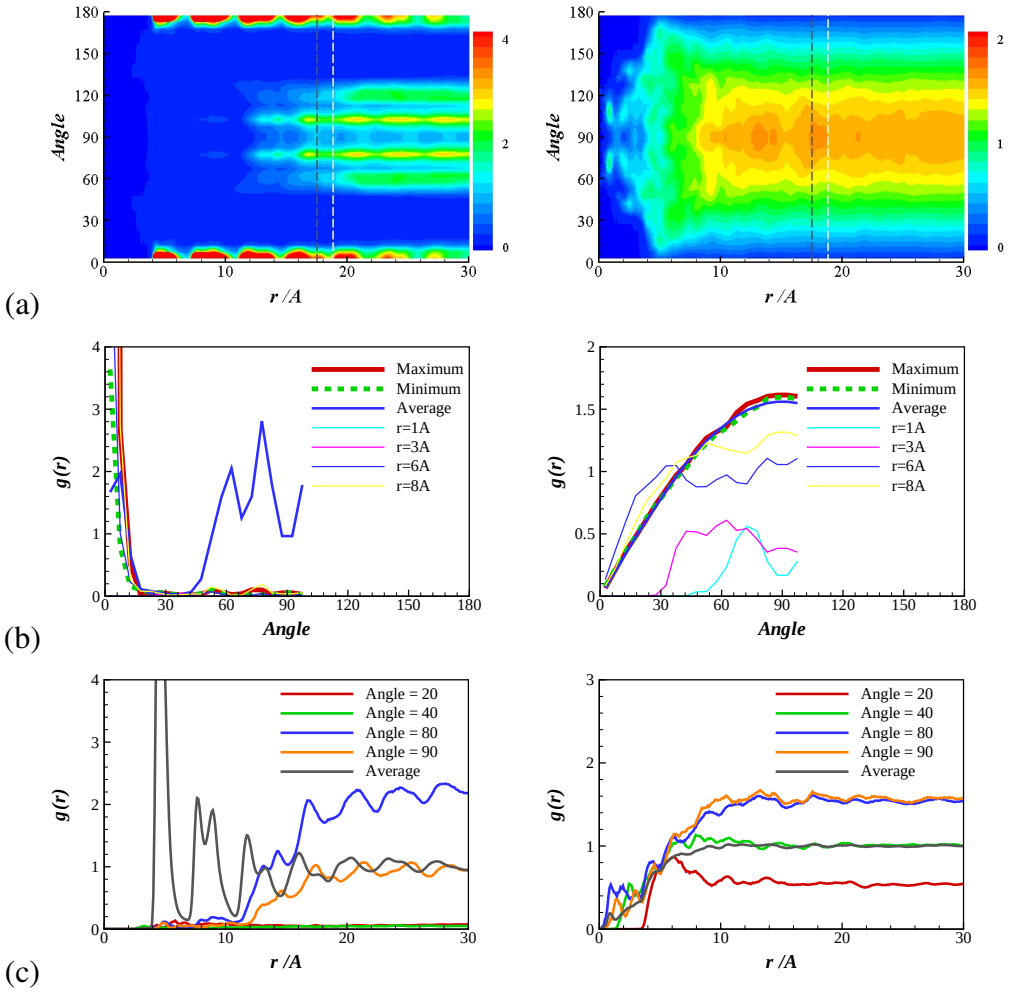

Figure 4.20: Contour plots of probability density of distance and angle between a pair of Linear molecules at 10 000 atm before (Case 1, left) and after (Case 3, right) heat treatment. (a) 2D contours, (b) RDFs at constant r, and (c) RDFs at constant angles. Distance r is in Å and angle in degrees.

plot on the right, main peaks are along 90° and distribution is more spread over all angles.

This is better shown in Figure 4.20(b). Before the heat treatment (left), there

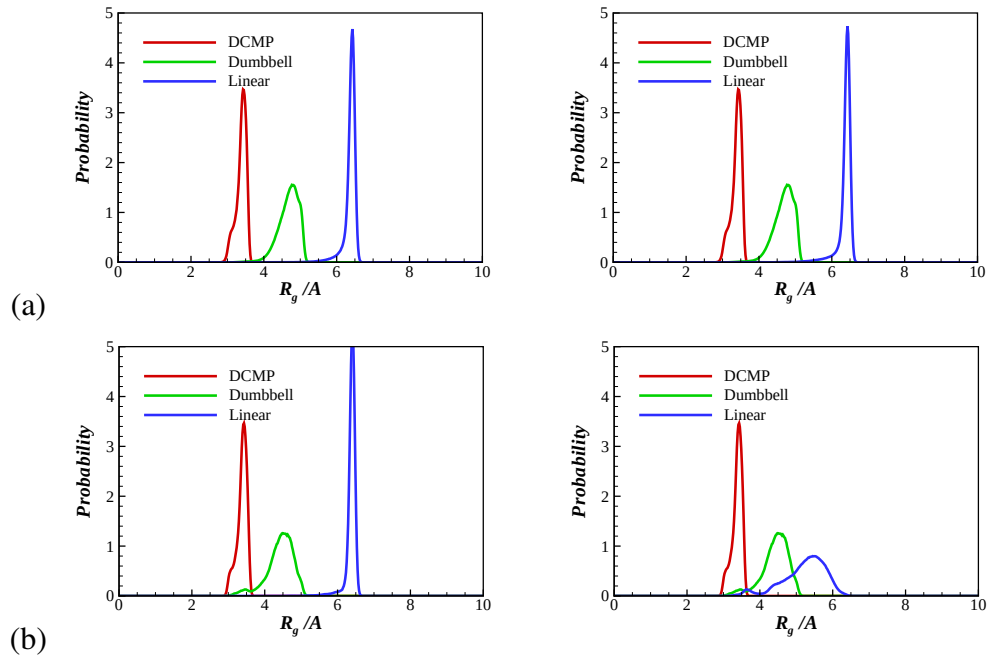

Figure 4.21: Radius of gyration (R_g) of DCMP, Dumbbell and Linear before (left) and after (right) heat treatment at (a) 1 atm and (b) 10 000 atm. R_g is in Å.

are very large peaks at $\theta < 10^\circ$, then minor peaks around 50° and 80°. After heat treatment shown on the right, the maximum line taken at $r = 17.5$ Å has a normal distribution along the angles. At $r = 6$ Å, the peak is more spread over the angles. There are pairs found even at $r = 1$ Å and they are mostly about 70° to each other. Another point to note is in the left plot of Figure 4.20(b), the average does not show a smooth normal peak unlike the 'after' plot on the right. Figure 4.20(c) also suggests that just gradually pressurising the system to a pressure as high as 10 000 atm is not an effective way of achieving a relaxed system, and instead heating up was needed.

Figure 4.21 shows the change in radius of gyration (R_g) before and after the heat treatment. Figure 4.21(a) shows R_g of DCMP, Dumbbell, and Linear at 1 atm before (left) and after (right) the heat treatment. Before, the peaks of DCMP, Dumbbell, and Linear lie at 3.3 Å, 4.7 Å, and 6.4 Å with the heights of 3.6, 1.6, and 4.6 respectively. There is little change in the distribution of R_g after the heat treatment at 1 atm. The peaks remain at the same place and the height of peaks stay the same, indicating that the system was at equilibrium before the heat treatment.

Same plots at 10 000 atm before (left) and after (right) are presented in Figure 4.21(b). On the left, DCMP has the highest peak at 3.3 Å with a height of 3.6. Dumbbell has its highest peak at about 4.5 Å and now develops a second peak at 3.5 Å. Linear shows a very high single peak at $r = 6.3$ Å. This distribution of R_g of DCMP and Dumbbell remain the same before and after the heat treatment. For DCMP, there is little change with pressure. The peak maintains the same shape and position. Dumbbell has developed a second peak at 10 000 atm and the height of the highest peak is reduced slightly. The largest change is seen with Linear molecules. The single distinctive peak observed before the heat treatment becomes broad and low after the heat treatment. The centre of the highest peak has moved to $r = 5.5$ Å with a height of 1 and there is a second peak appearing at $r = 3.6$ Å.

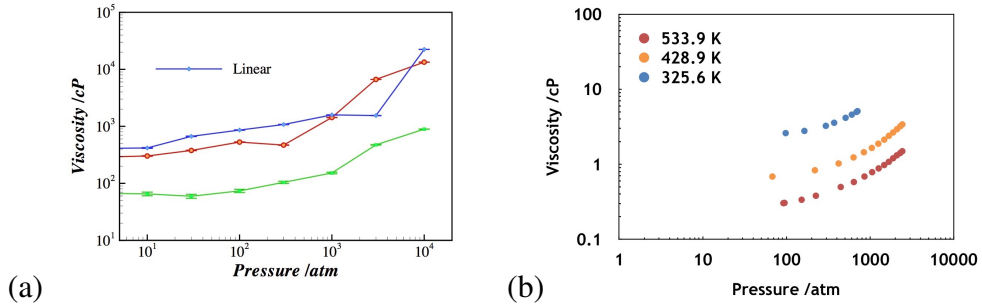

(a) (b)

Figure 4.22: (a) Viscosity of Linear in this study and (b) viscosity of *n*-octadecane by Baled *et al.*[89].

4.2.6 Using CHARMM force field under high pressure

The CHARMM force field was developed under ambient condition.[86–88] Therefore extra care is required when transferring these parameters for use in high pressure simulations. The CHARMM force field is commonly used in biological research including proteins and lipids. The pressure conditions of these studies are typically low. As a result, there are few relevant high pressure studies by experiment or simulation. Baled *et al.*[89] measured the viscosity of *n*-octadecane under relatively high pressure. The simulation results of Linear, which is also octadecane but modelled with united atoms, were compared with this data in Figure 4.22.

MD simulations using CHARMM32 produced relatively higher values of viscosity. The experiment was carried out at higher temperatures 325.6 K, 428.9 K, and 533.9 K whereas the MD simulations presented here were performed at 300 K.

Physical liquids solidify under high pressure, and increased temperature was required to keep them liquid to measure viscosity. The viscosity decreases when temperature increases as expressed in Equations (3.35)-(3.37). The viscosities obtained from MD studies increased in a similar manner as the experimental results. In Figure 4.22(a), when the pressure increased from 100 atm to 1000 atm, the viscosity increased, from 860.46 cP to 1586.69 cP. On the Figure 4.22(b), at 533.9 K, when the pressure increased from 95 atm to 1059 atm, the viscosity increased from 0.305 cP to 0.784 cP.

The viscosity was calculated via Stokes-Einstein equations using radius of gyration as a diameter of the molecule. The radius of gyration, R_g, of Linear changed most and this was expected to produce the least accurate result. Therefore MD simulations with CHARMM force field can be reasonably used to understand the trend of viscosity with increased pressure.

Chapter 5

RESULTS: 2,4-DICYCLOHEXYL-2-METHYLPENTANE (DCMP)

Molecular dynamics simulations result of DCMP are presented in this chapter. Its structure and bulk properties including volume, density, and mobility at different pressures are investigated.

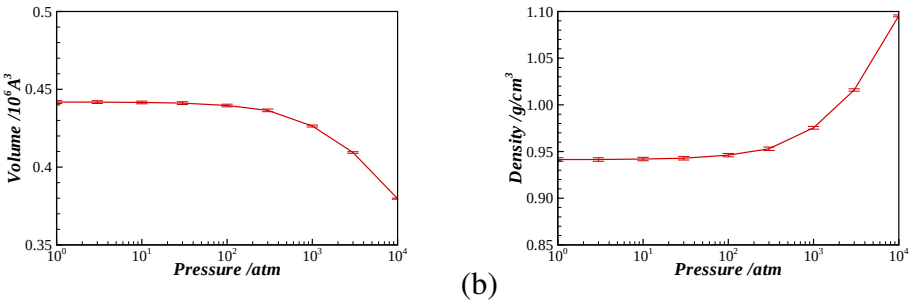

(a) (b)

Figure 5.1: Average (a) volume and (b) density trends of DCMP from 1 atm to 10 000 atm at 300 K. Volume is in 10^6 Å^3, density in g/cm^3, and pressure in atm.

5.1 Thermodynamic properties

As the first step of this experiment, equilibrium densities of DCMP for a range of pressures are compared by monitoring volume changes in NPT simulations. Figure 5.1 shows the volume and density of DCMP under different pressures. Pressures are in atm and plotted on a log-scale. The volume of DCMP changes from over 440 000 Å^3 at 1 atm to 380 000 Å^3 at 10 000 atm. This is a reduction of about 13.6%. In other words, the length of the simulation box decreased by about 5% when the pressure increased from 1 atm to 10 000 atm.

The density of DCMP shown in Figure 5.1(b) was calculated using the calculated volume and molecular mass. Since the mass is constant, the density trend is inverse to the volume. As a result of changes in the volumes, the density of DCMP in the simulation box increased from 0.94 g/cm^3 to 1.09 g/cm^3.

5.2 Transport properties

Mean square displacements (MSDs) of the centres of mass of DCMP molecules under various pressure conditions are calculated to measure the mobility of the molecules.

MSDs of DCMP at various pressures are shown in Figure 5.2. The x-axis is the time difference (Δt) in ps and the y-axis is the MSD in Å^2. Each line on this plot represents a pressure between 1 atm and 10 000 atm, with the dark red line on the top being 1 atm and the blue line at the bottom 10 000 atm. DCMP molecules at 1 atm, 3 atm, and 10 atm show similar mobility. The next three higher pressures, 30 atm, 100 atm, and 300 atm lie close together. They are slightly less

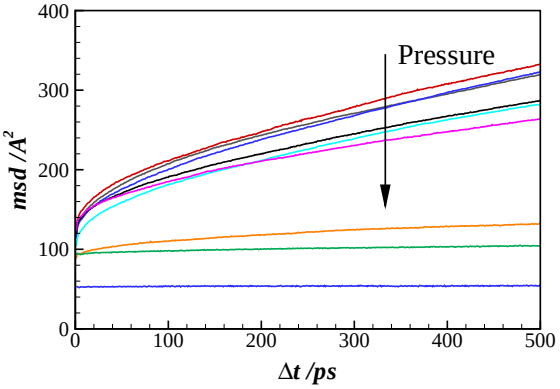

Figure 5.2: Mean squared displacement of DCMP at various pressures showing the decrease in mobility with increasing pressure. MSDs are in Å^2 and Δt in ps. The arrow indicates increasing pressure.

mobile than the first group. There is an initial unstable slop within 20 ps, then the displacement increases linearly. At 1000 atm and 3000 atm, the mobility of the molecules reduces significantly and the gradients of the lines reduce to close to zero. Unsurprisingly, molecules under 10 000 atm move the least. The MSD shows almost no change even after 500 ps and the initial MSD value is about half of that of 3000 atm system. Overall, the displacement was significantly reduced at higher pressures. The three highest pressures, 1000 atm, 3000 atm, and 10 000 atm, are separated from the rest of the lines, showing almost flat lines, indicating a very low diffusivity.

In all cases, mobilities measured by MSD are reduced when pressure is increased. MSD increases very sharply for small Δt, and then the increase in MSD slows down. After a short while, the MSDs of the molecules increases linearly. The slopes of these plots are related to the diffusion coefficients of the molecule.

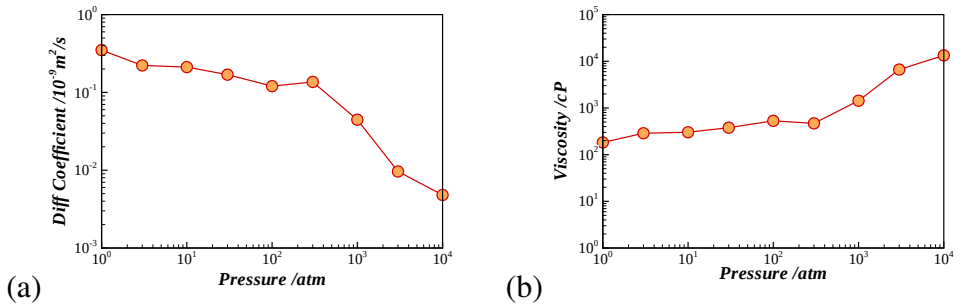

(a) (b)

Figure 5.3: Diffusion coefficient and viscosity of DCMP as a function of pressure. Pressure is in atm, diffusion coefficients in 10^{-9}m^2/s, and viscosity in cP.

Diffusion coefficients are calculated using the slope of the MSD plots in Figure 5.2 and Equation (3.47). The slope was determined using the least squares fitting on the data points $\Delta t < 500$ ps. The MSD points of $\Delta t < 100$ ps were also ignored in the fitting.

$$\langle r(t) - r(0)|^2 \rangle = 6Dt + C. \tag{5.1}$$

Figure 5.3 shows the diffusion coefficients and viscosity of DCMP as a function of pressure. The diffusion of DCMP at 1 atm is about 0.2×10^{-9} m^2/s and the diffusivity decreases gradually until $P = 300$ atm. Beyond $P = 1000$ atm, the diffusivity drops significantly to 0.005×10^{-9} m^2/s at 10 000 atm.

The viscosity of DCMP is estimated from the Stokes-Einstein relation, assuming the molecules that are hollow spherical molecule of the same mass and the same moment of inertia. Figure 5.3(b) shows this viscosity. Please note that both pressure and viscosity are on a log-log scale. The viscosity of DCMP increases as pressure increases, and the rate of increase is greater at pressures above $P = 300$ atm. As viscosity is inversely proportional to diffusion coefficient according to the Stokes-Einstein relation, the viscosity trend against pressure of DCMP is roughly inverse to the trends in the diffusion coefficients. It is estimated that at 10 000 atm, the viscosity of DCMP is over 10 000 cP. This is significantly lower than the values predicted by Equation (3.49) in Chapter 2.2.2.

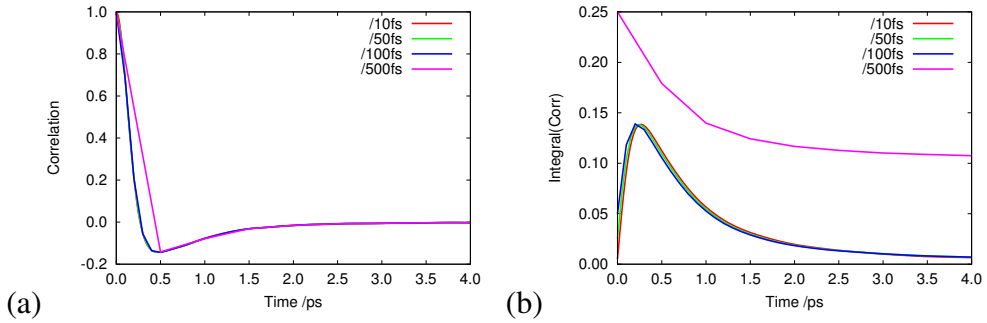

Figure 5.4: Data resolution effect on the velocity time correlation of DCMP at 1 atm. (a) Velocity time correlations with different time interval and (b) integrals of the correlations. The time difference Δt is in ps.

Transport coefficients can be calculated from equilibrium correlation functions. Diffusion coefficients are also calculated from Equation (3.46).

$$D = \frac{1}{3}\int_0^\infty dt \langle \mathbf{v}_i(t) \cdot \mathbf{v}_i(0) \rangle.$$

First, the data resolution for calculating the velocity correlation was tested. The velocity time correlation of molecules was calculated at the intervals of 10 fs, 50 fs, 100 fs, and 500 fs. Figure 5.4 shows that an interval of 500 fs to be too large to accurately capture the correlation at 1 atm but 10 fs, 50 fs, and 100 fs gives similarly accurate. The interval, Δt, of 50 fs was chosen.

The diffusion coefficients of DCMP at 1 atm, 1000 atm, 3000 atm, and 10,000 atm calculated from the velocity time correlation are presented in Fig-

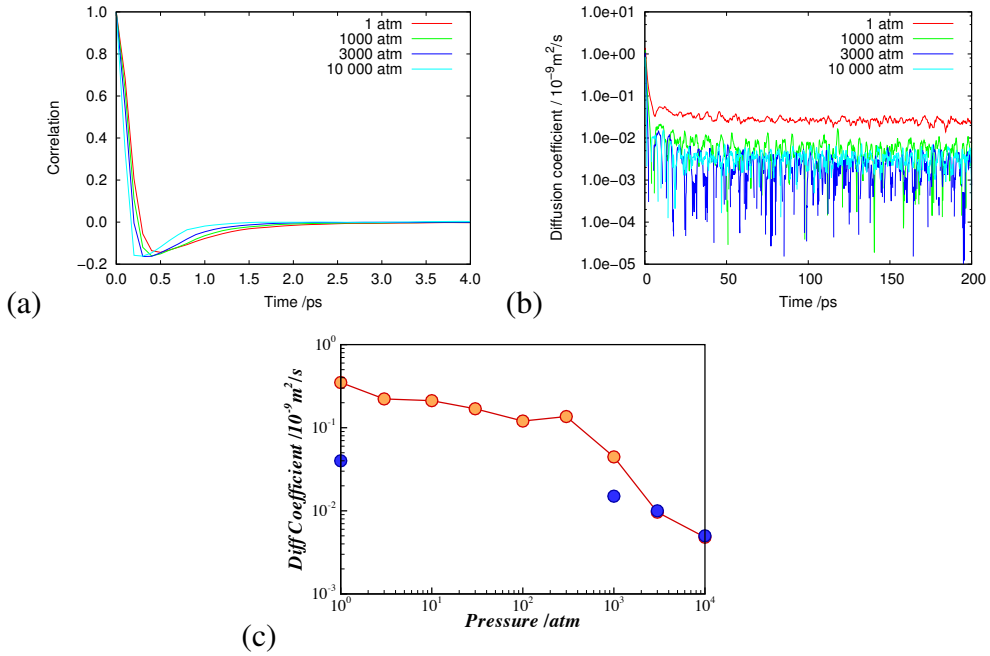

Figure 5.5: Diffusion coefficients from the velocity time correlation of DCMP. (a) velocity correlation function of DCMP under different pressure conditions, (b) diffusion coefficients calculated using the Green-Kubo relation (equation (3.46)), and (c) comparison of two methods. Orange circles are diffusion coefficients from the mean-squared displacement and blue circles from the viscosity correlation function. Pressure is in atm, the coefficients in $10^{-9}\mathrm{m}^2/\mathrm{s}$.

ure 5.5. The correlation died out in about 2 ps for all pressures presented as can be seen in Figure 5.5(a). Figure 5.5(b) further shows dying out of the correlations. The velocity correlation decays more slowly at 1 atm than at higher pressures. The diffusion coefficients calculated from the velocity correlations are comparedand with the diffusion coefficients from the mean-squared displacements in Figure 5.5(c). The diffusion coefficient at 1 atm is smaller than the diffusion coefficient calculated the by previous method where as the other pressure cases show

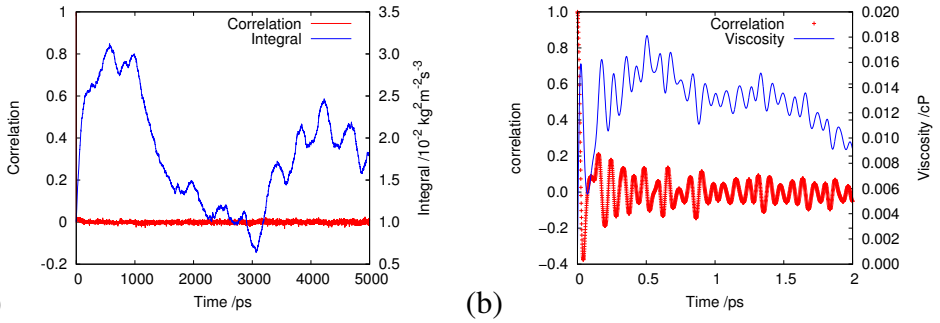

Figure 5.6: Stress tensor time correlations (red) and viscosity (blue) for (a) 5 ns and (b) the first 2 ps. Time is in ps, the integral in 10^{-2} kg^2/m^{2}s^3 (therefore viscosity in cP).

a similar scale.

The viscosity η can be calculated from stress tensor time correlations with

$$\eta = \frac{V}{k_B} \int_0^\infty dt \langle \mathbf{p}_i(t) \cdot \mathbf{p}_i(0) \rangle, \tag{5.2}$$

where V is volume of the system, k_B is the Boltzmann constant, $\mathbf{p}_i$ is the stress tensor of a particle i.

The viscosity of DCMP at 1 atm calculated from Equation (5.2) was shown in Figure 5.6. The simulation was performed over 30 ns. Figure 5.6(a) shows the stress tensor correlation of the first 5 ns in red. In this scale, the correlation looks flat with little fluctuation. However, the integral of it presented in blue diverges widely moving above and below zero values with time. This is also observed in

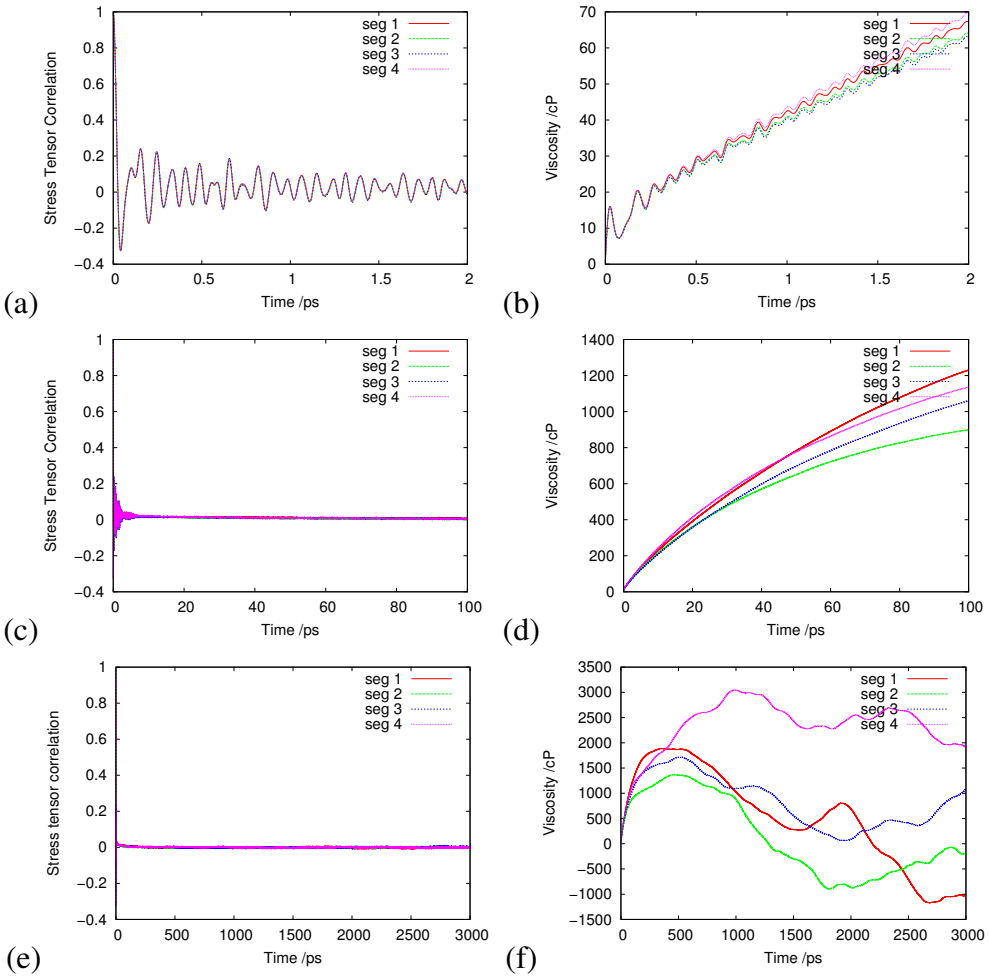

Figure 5.7: Stress tensor time correlations and viscosities of (a),(b) 2 ps, (c),(d) 100 ps, and (e),(f) 3 ns.

Figure 5.6(b), which is a close up. Figure 5.6(b) shows the stress tensor correlation and the viscosity of the first 2 ps and the fluctuation of the correlation is more visible. It seems that calculating equilibrium viscosity this way requires much longer simulation for molecules of this size. The first 10 ns data was discarded in calculating viscosity.

Figure 5.7 shows the stress tensor time correlation function of DCMP at 1 atm and the viscosity calculated from it. Segments are selected from different section of a 30 ns simulation. The stress correlations of different segments in Figures 5.7(a), (c), and (e) seem to show reasonable agreement. In Figure 5.7(b), the viscosities from each segment are close to each other. They start deviating in Figure 5.7(d) and in Figure 5.7(f) in 3 ns time scale, they behave very differently. This illustrates the difficulty of calculating viscosity via the Green-Kubo relations.

5.3 Structure

Structural properties, such as the radial distribution function, the radius of gyration, the angles between molecules, and the angles between rings of the molecules as defined in Chapters 5.3.2 and 5.3.3, are analysed for the DCMP molecules in this chapter. Also, an attempt has been made to link these properties to the properties.

5.3.1 Radial distribution functions

Radial distribution functions (RDFs) of DCMP at all pressures are presented in Figure 5.8(a). The RDFs of this figure indicate that the first peaks for all pressures

are at around $r = 8$ Å. All but the two highest pressures follow a similar trend. The first peak of 3000 atm moves inwards, and that of 10 000 atm is shows two peaks around $r = 8$ Å. The trough of 10 000 atm also has a "double-dip". The RDF of DCMP at 10 000 atm is less well defined compared to the lower pressure systems.

RDFs of DCMP at 1 atm and 10 000 atm at a close range of $0 < r < 12$ Å are shown in Figure 5.8(b). DCMP at 1 atm and at 10 000 atm follow a similar trend, although under high pressure the molecules come closer to each other and the RDF profile contains small fluctuations. The peaks are located at about the same distance but DCMP at 1 atm has a flatter and broader peak and DCMP at 10 000 atm appears to show two smaller peaks. DCMP at 1 atm has a smooth RDF line, whereas at 10 000 atm there are a number of smaller peaks or 'bumps'.

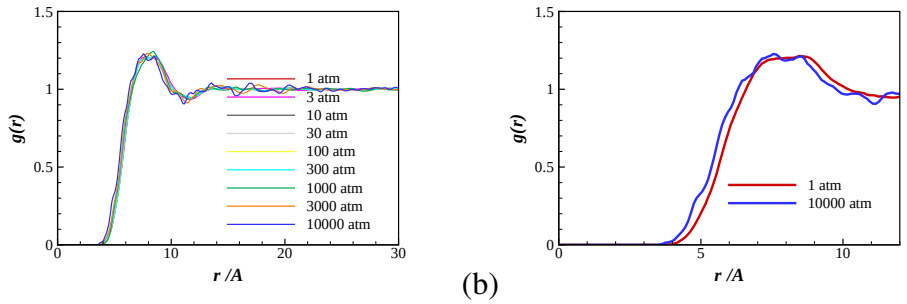

Figure 5.8: (a) Radial distribution functions and (b) the close-ups of DCMP. All pressures are plotted on the left and close-up of two extreme pressures on the right. Distance between the centres of mass of molecules, r is in Å.

5.3.2 Relative positions of molecules

The orientation of each molecule in the simulation box is defined using the moment of inertia. The directional vector is defined as the axial direction along which the moment of inertia is a minimum. Then the angle that the directional vectors of two molecules make, θ, are monitored together with the distance between the centres of mass of that molecule pair. A schematic diagram of the angle between two molecules is shown in Figure 5.9.

Figure 5.10 shows the radial distribution, $g(r,\theta)$, of molecule pairs as a function of angles and distances between the centres of mass of DCMP molecules. Green colour represent the bulk average and the concentration is scaled in red to blue from highest $g(r,\theta) = 3$ to the lowest $g(r,\theta) = 0$.

For all pressure values, the perpendicular position ($\theta = 90^{\circ}$) is the most pop-

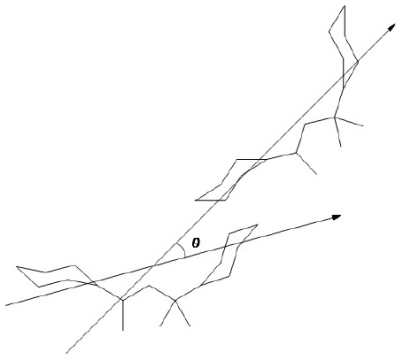

Figure 5.9: Definition of the orientation of a molecule and the angle between molecules, θ.

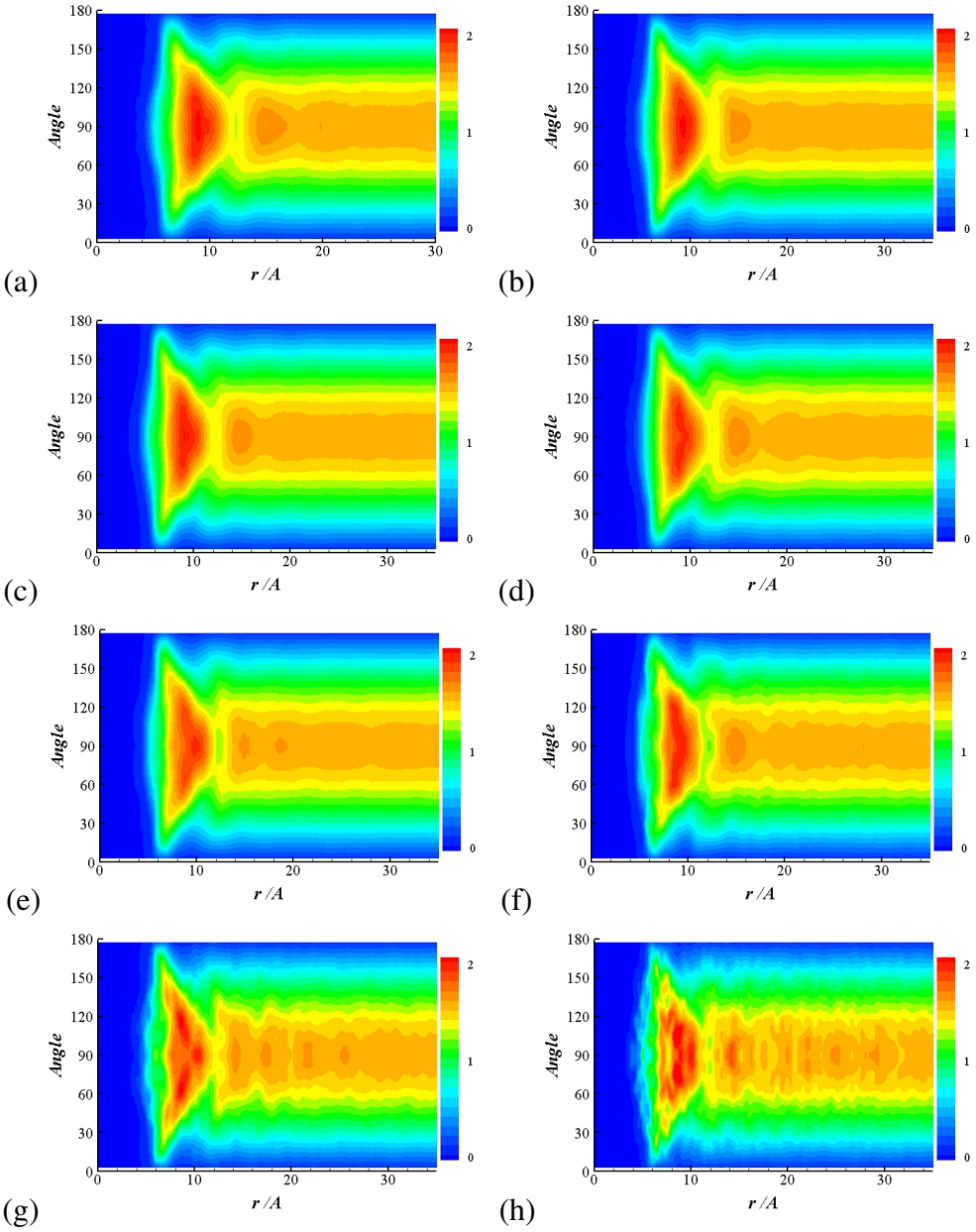

Figure 5.10: Contour plots of distance and angle of molecule pairs of DCMP at (a) 1 atm, (b) 10 atm, (c) 30 atm, (d) 100 atm, (e) 300 atm, (f) 1000 atm, (g) 3000 atm and (h) 10 000 atm. The red is of the highest density and the blue the lowest. Distance r is in Å and angle in degrees.

ulous. DCMP at 1 atm (Figure 5.10(a)) shows that the concentration is the highest at a distance of about $r = 9$ Å and inter-molecular angle of $\theta = 90^\circ$. There are D-shaped contour lines formed around the local maximum. When DCMP molecules are about $r = 6$ Å apart, they can be at angles between 30° and 150° with each other, but a pair with $r > 9$ Å tends to be perpendicular to each other, although molecule-pairs are found to be at less than 30° as well. For all r values, there are more pairs at the perpendicular position, but there is a 'gap' along $\theta = 90^\circ$as well at about $r = 12$ Å. This will be further discussed later. The second most populous area is found at around $r = 15$ Å and $\theta = 90^\circ$. One pronounced trough is found at about $r = 12$ Å and $\theta = 90^\circ$. It is less common for a pair to be in a parallel position.

The overall pattern remains the same as the pressure increases, with the peaks moving inwards slightly, and for $P > 1000$ atm, the contour lines contain small-scale oscillations. As the pressure increases further, three local maxima become more pronounced in place of a single maximum. For example, at $P = 3000$ atm, the three peaks are clearly seen at ($r = 9$ Å, and $\theta = 60^\circ$), ($r = 9$ Å, and $\theta = 120^\circ$), and ($r = 11$ Å, and $\theta = 90^\circ$). The $P = 1$ atm plot in Figure 5.10(a) shows only two peak areas along the r direction, but the $P = 3000$ atm plot in Figure 5.10(g) shows 6 peaks, the farthest being at around $r = 25$ Å. $\theta = 90^\circ$ is still the most populous angle at longer distances, but distances between $r = 8$ and $r = 10$ Å,

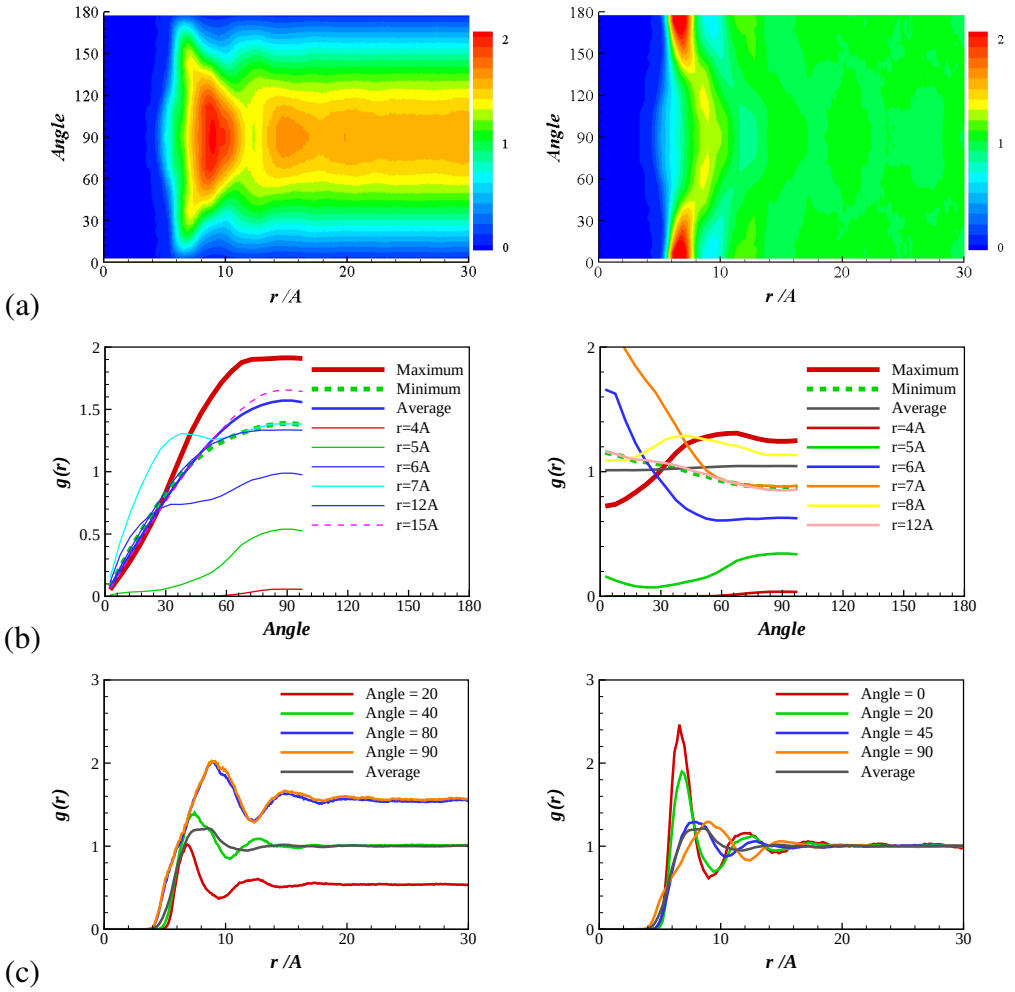

Figure 5.11: Distribution of distance and angle for DCMP at 1 atm. (a) 2D contours, (b) RDF at constant r, and (c) RDF at constant angles.

with $\theta = 60^\circ$ or 120° are preferred. The $P = 10\,000$ atm plot in Figure 5.10(h) is even fuzzier although the overall pattern is broadly similar. In other words, the molecule pairs take more varied angles with each other. Although $\theta = 90^\circ$ is still preferred, the preference is less pronounced. They may stack any way they can to release the energy from the pressure.

Figure 5.11 shows two different ways of looking at the distribution of DCMP molecule pairs. In the left-side plot, the population was binned by angles (y-axis) as well as centre of mass distance (x-axis). In the right-side plot, the molecule pairs (y-axis) were binned by $\cos\theta$ values. The left hand side plot in Figure 5.11(a) shows the most populous area as red, whereas the right hand side plot shows the highest concentration sites as red. The most molecular pairs are found in the area around $r = 9$ Å and 90°, but the probability of finding a DCMP pair is the highest for $6 < r < 8$ Å and $0 < \theta < 30°$. The DCMP pairs at 1 atm which are parallel or close to parallel to each other are most likely to be found at the inter-molecular centre of mass distances about $6 < r < 8$ Å and then around $r = 12$ Å. The DCMP pairs that are perpendicular are most likely to be found at a distance of about $8 < r < 10$ Å. For large r values, the preference is less pronounced.

Figure 5.11(b) shows how $g(r)$ of DCMP at 1 atm behaves as a function of angle at different distances. The thick blue line is the average over $20 < \theta < 30$. On the left, the average line (blue) is bell shaped. The 'maximum' line that goes through the highest peak point of $r = 9.5$ Å is the most populous at $6° < \theta < 90°$ section. The minimum is through the $r = 12$ Å line where the fist trough lies. This line has a similar curve as the average line, except the peak is lower where the molecules are perpendicular to each other. On the left, the average is a flat line of $g(r) = 1$ as expected. The $r = 6$ and 7 Å lines that go through the red area in

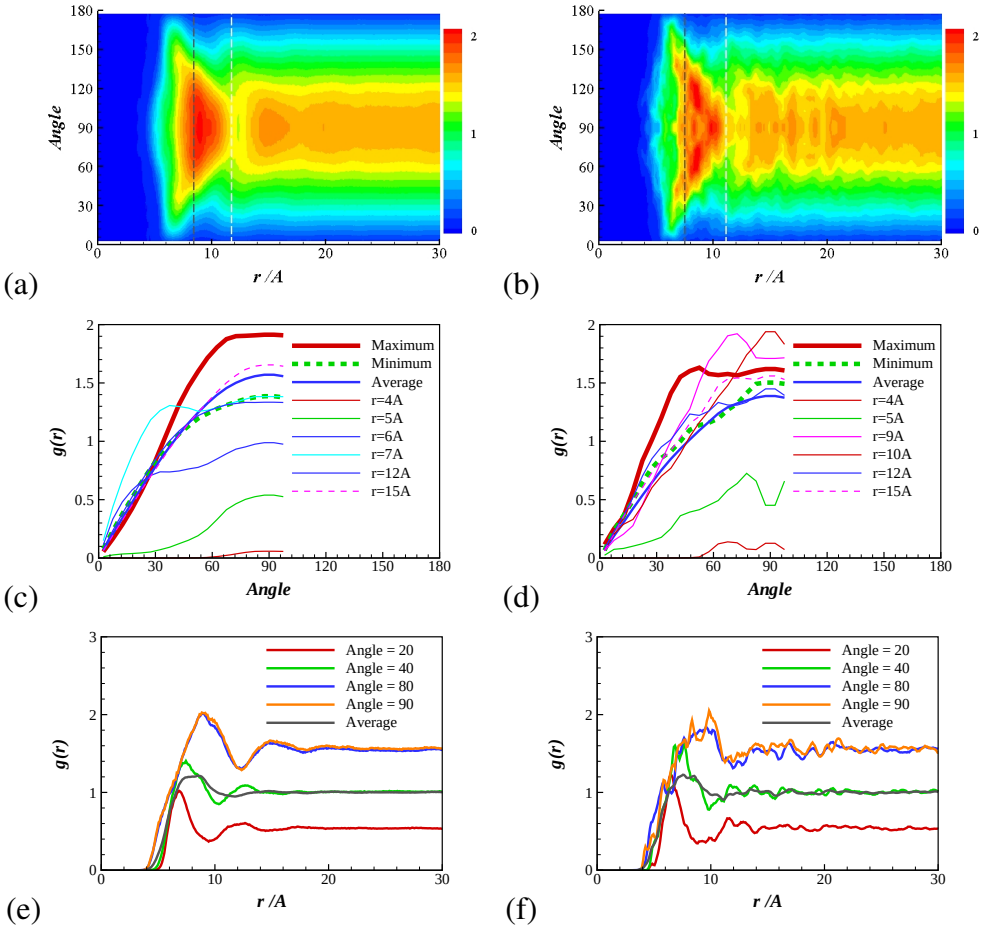

Figure 5.12: Relative orientation and distance of DCMP molecules at 1 and 10 000 atm. Distance between the centre of molecules is in Å and angle between the molecules in degrees.

Figure 5.11(a) show that the most probable position for a pair of DCMPs is a parallel position. They both have the highest $g(r)$ peak near 0°(or 180°).

Figure 5.11(c) show the $g(r)$ plot at several angles. The plots on the right show that smaller angles of 0° and 20° have the first peak at $r = 7$ Å, the fist trough at $r = 9$ Å, and the second peak around $r = 12$ Å. The pairs at $\theta = 45°$

prefer to be at $r = 9$ Å. Further out, the distance shows no preference.

The pair angles and centre of mass distances of DCMP at 1 atm and at 10 000 atm are compared in Figure 5.12. Contour plots on the left are for DCMP pairs at 1 atm and on the right for DCMP pairs at 10 000 atm. Angles are binned by the pair angle, θ, rather than $\cos\theta$. Cross sections of Figure 5.12(a) along a constant distance are plotted in Figure 5.12(c). Again, the thick blue line is the average over $20 < \theta < 30$. Examination of the cross section along the distance where the first peak lies shows there is no pair parallel to each other and as the angle increases, the number of pairs increases gradually. There are more molecule pairs at 60° or larger. The first trough distance also has a similar angular distribution, having a peak at near $\theta = 90°$. At $r = 4$ Å and $r = 5$ Å, $g(r)$ has peaks at $\theta = 90°$. The cross section at $r = 7$ Å shows that molecule pairs at $r = 7$ Å are found over all angles, with small peaks around $\theta = 30°$ (and 150°) and the second level peak or a plateau, yet lower than the average line, found around $\theta = 90°$. There are more than an average number of molecule pairs at this distance. This flips back to $\theta = 90°$with a peak at $r = 15$ Å. By $r = 15$ Å, the distribution of the angles become very close to the bulk average distribution. Figure 5.12(e) shows the RDF at several angles. The average line in grey is the RDF of molecular pairs. The lines for $\theta = 80°$ and 90° have the highest $g(r)$, *i.e.*, they are the most popular relative angles with peaks near $r = 90$ Å. The $\theta = 40°$ is close to the average RDF

and the peak is located at about $r = 7$ Å. $\theta = 20^\circ$ is less popular and the molecule pairs are mostly separated by $r = 6$ Å.

The 1D RDF profiles of Figure 5.12(b) at 10 000 atm calculated along constant r values are shown in Figure 5.12(d). At the first RDF peak of $r = 8$ Å, the angles between 30° and 150° are the most popular. The average of angle distribution is similar to the average at 1 atm with lower height. The RDF profile at $r = 4$ Å has small peaks at $\theta = 70^\circ$, 90°, and 110°. The RDF profile at $r = 5$ Å has peaks at $\theta = 80^\circ$ and 100°. These lines show less than the average number of DCMP pairs. The $r = 9$ Å RDF profile has a similar shape as the $r = 5$ Å RDF profile, but peaks are close to $\theta = 70^\circ$ and 110°. The RDF profile at $r = 10$ Å shows a single peak at $\theta = 90^\circ$. At 10 000 atm, the most popular angle between DCMP pairs is $\theta = 80^\circ$ and 90°, too. The shape of the RDF profile is less 'clean' but overall, the peaks are at about $r = 9$ Å. The next popular angle is $\theta = 40^\circ$ and the peak is located at $r = 7$ Å. There are less than average number of pairs at $\theta = 20^\circ$, mostly found at around $r = 6$ Å.

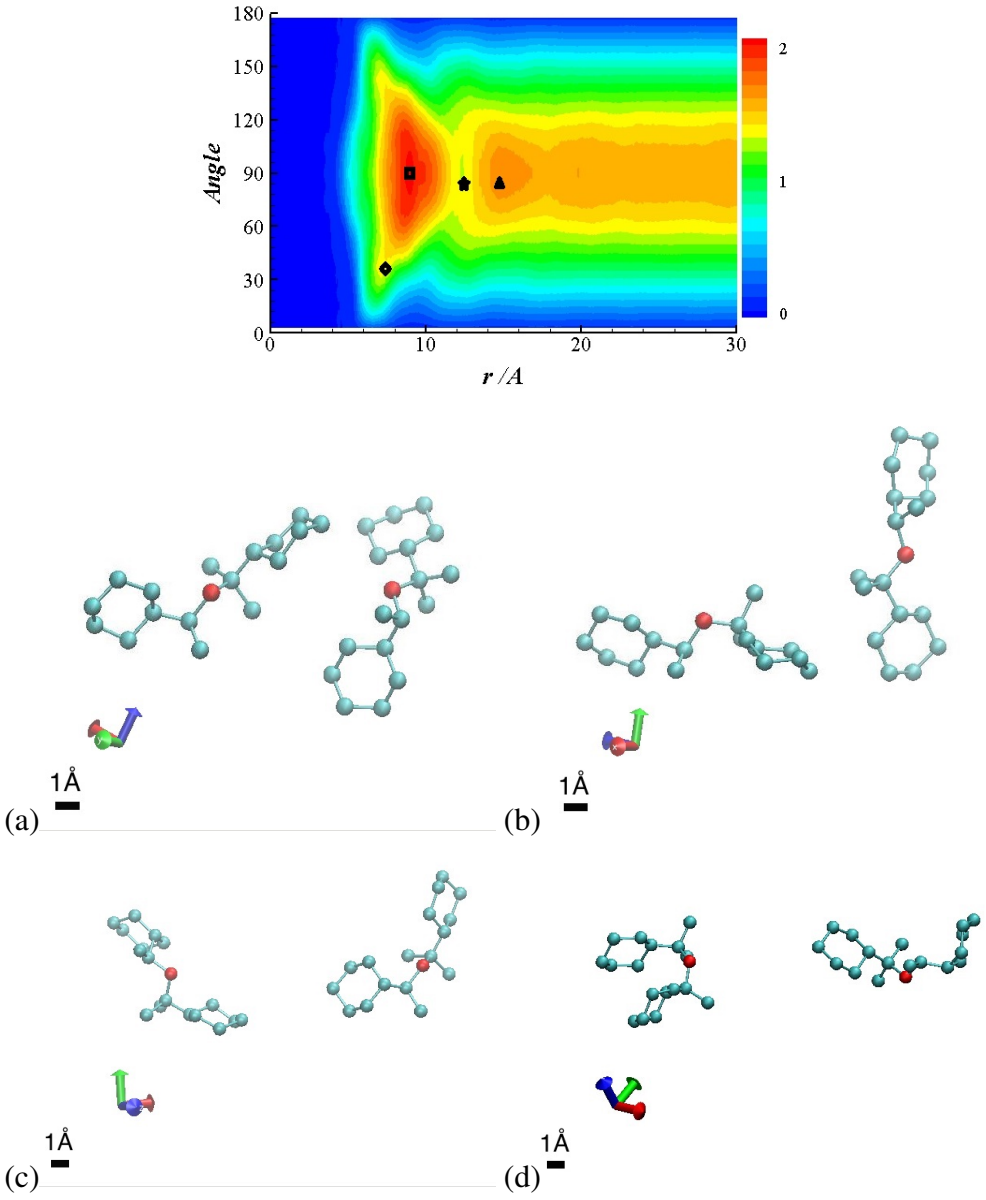

Figure 5.13: Example molecule pairs at 1 atm for selected points in the 2D RDF contour plot. Locations marked as (a) diamond (7.45 Å and 42.5°), (b) square (8.95 Å and 82.5°), (c) star (12.35 Å and 87.5°), and (d) triangle (14.85 Å and 88.5°). Red spheres are the united atoms nearest to the centre of mass of the molecule.

Snapshots of some molecule pairs taken using VMD[90] are presented in Figure 5.13 in order to highlight the distinctive shape of different DCMP molecules. DCMP molecules are coloured green and the united atom nearest to the centre of mass of each molecule is coloured red. The molecular pairs in Figure 5.13(a) are separated by $r = 7.5$ Å and angle of $\theta = 40°$, marked as a diamond in the 2D RDF plot. Both molecules are stretched and the distance between the two rings in the molecule is large compared to a U-shape molecule such as the molecule on the left in Figure 5.13(d). Apart from the pair in Figure 5.13(a), all the pairs are perpendicular to each other. The pair in Figure 5.13(b), marked as a square, is located at $r = 9$ Å and $\theta = 80°$. This is the most popular inter-molecular arrangement at this pressure. The pair in Figure 5.13(c), marked as a star, is at $r = 12.3$ Å and at $\theta = 90°$, which is a local minimum in the 2D RDF map. The pair in Figure 5.13(d), marked as a triangle, is located at $r = 15$ Å and $\theta = 90°$.

Figure 5.14 shows snapshots of some DCMP pairs at 10 000 atm. Figure 5.14(a) is an example of the position marked as a square in the 2D RDF plot. The centres of mass of the molecule pair are located 8.55 Å apart and they are at $\theta = 60°$. The pair marked as a diamond shown in Figure 5.14(b) is located at $r = 8.5$ Å and $\theta = 90°$. The pair in Figure 5.14(c), marked as a star, is located at $r = 6.7$ Å apart with the angle of $\theta = 20°$. The molecules in these pairs are relatively stretched with a flat shape, compared to the molecules on the left in Figure 5.14(d). In the

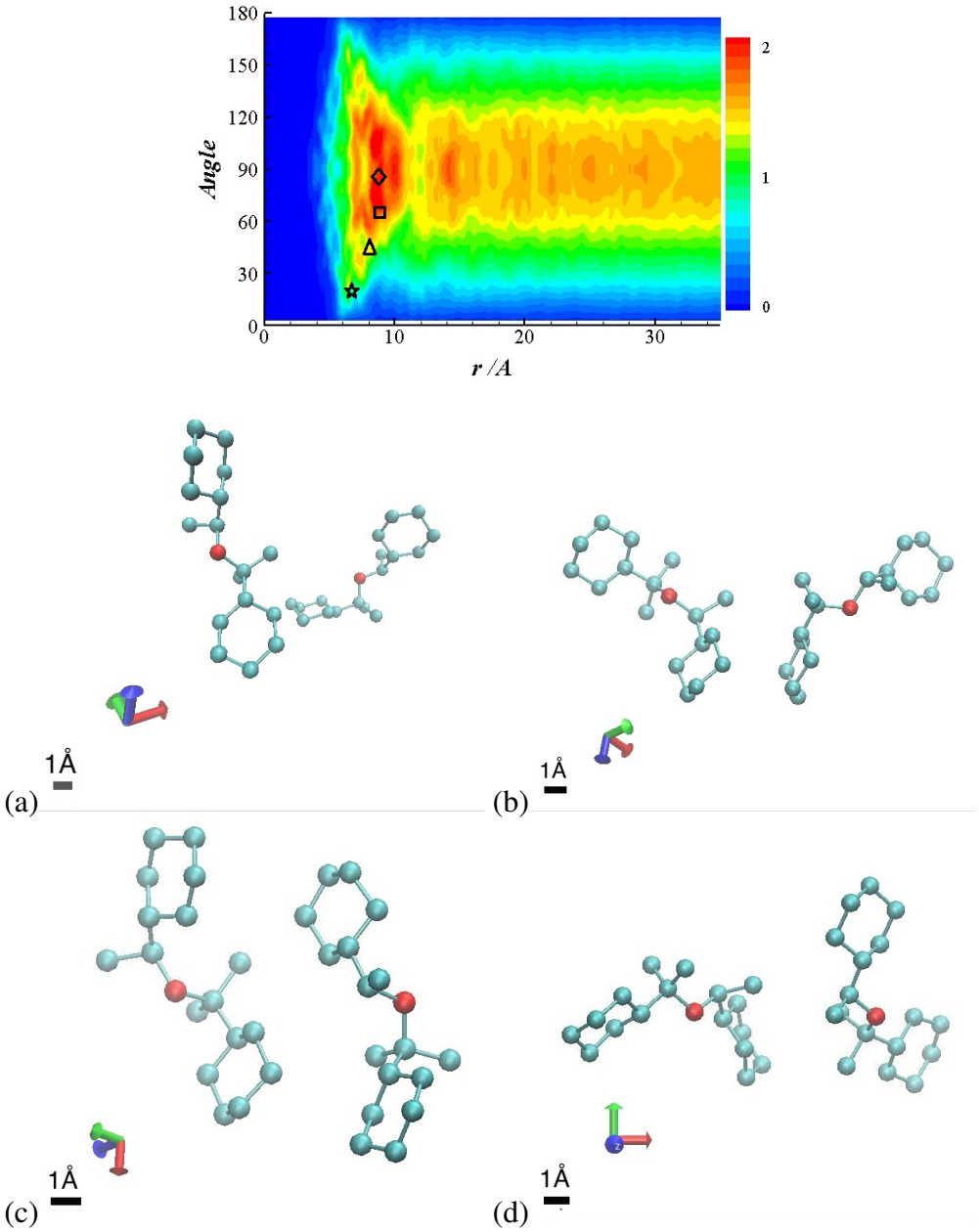

Figure 5.14: Example molecule pairs at 10 000 atm for selected points in the 2D RDF contour plot. Locations marked as (a) square (8.55 Å and 62.5°), (b) diamond (8.55 Å and 87.5°), (c) star (6.70 Å and 20.0°), and (d) triangle (8.0 Å and 45.0°). Red spheres are the united atoms nearest to the centre of mass of the molecule.

last figure, the pair is at $r = 8$ Å and $\theta = 45^\circ$ and both molecules are U-shaped. These show some of the different ways of alignment that molecular pairs can take. The first two inter-molecular arrangements are more popular than the last two.

5.3.3 Relationship between two rings in the same molecule

Similar to the previous section, angles and distances between the two rings in one DCMP molecule are charted in this section.

The planes for each ring are defined as follows:

1. Take a cyclohexyl ring of carbon numbered 1-6 as in Figure 5.15. A cyclohexyl ring is most likely to be in a chair-, a boat-form, or something in-between, which means four carbons are likely to be located on a plane while the other two carbons are off the plane.

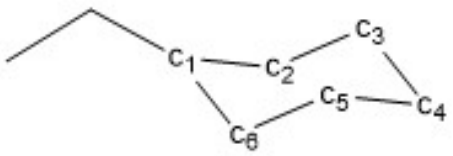

Figure 5.15: Numbering of cyclohexyl-ring.

2. Then, select a set of four carbons on the opposite side of the ring, for example, C_1, C_2, C_4, and C_5. Measure how closely these four carbons are positioned from a plane.

3. A plane was defined using three carbons (C_1, C_2, and C_4). And, another plane was defined using C_1, C_2, and C_5. The relative angle between these two planes was calculated, and this relative angle was used to define the flatness of the set of four carbons.

4. Steps 2 and 3 were repeated for the other two sets of four carbons: $C_2-C_3-C_5-C_6$ and $C_3-C_4-C_6-C_1$.

5. Of these three sets of four carbons, the four-carbon set with the smallest relative angle was chosen to finally define the orientation of the cyclohexyl ring.

6. Also the centre of mass of each ring provided the coordinate for the distance measurement.

Figure 5.16 shows how the angle, θ, between the rings in one molecule is defined. The distance between the centres of mass and the relative angle between the two rings together will indicate the shape of the DCMP under pressure.

Distance and angle between two cyclohexyl rings in DCMP are plotted in

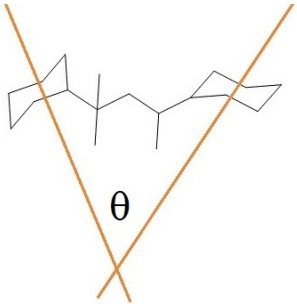

Figure 5.16: Definition of the angle between two rings in the same molecule.

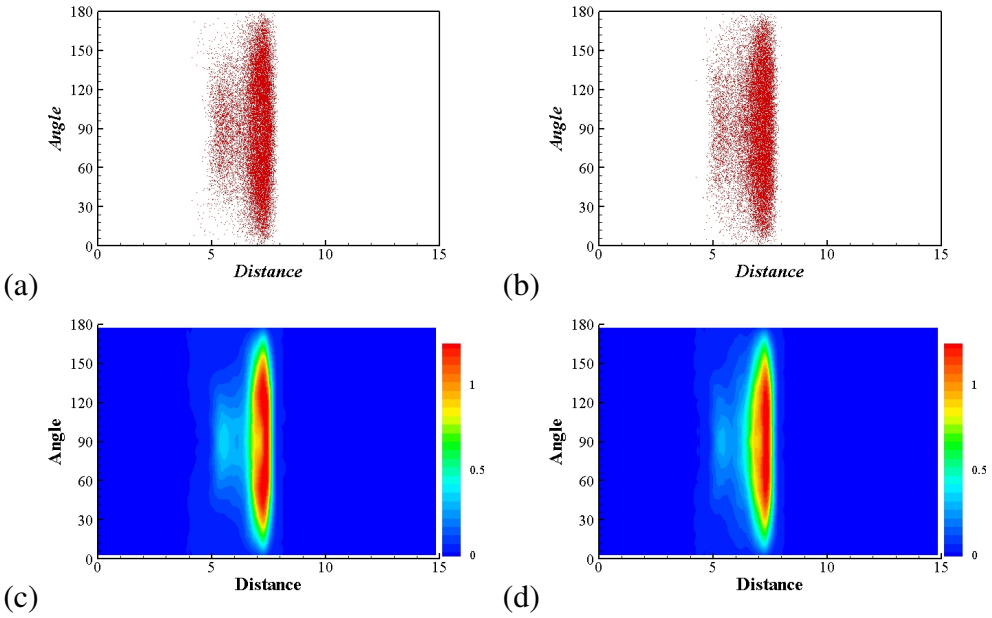

Figure 5.17: Scatter and contour plots of the ring separation distance (r_s) and the relative angle (θ) at 1 atm ((a),(c)) and at 10 000 atm ((b),(d)). Distance is in Å and angle in degrees.

Figure 5.17. On the left are plots for the DCMP rings at 1 atm. At the top are scattered plots, and at the bottom are the 2-D contour plots. The most number of rings are at a distance between $r = 5$ and $r = 8$ Å and they are spread over

a wide range of angles. Considering there is a bias for $\theta = 90^\circ$, this shows that the probability of rings being parallel to each other is higher than being perpendicular. DCMP at 1 atm shows peaks around $\theta = 60^\circ$ (and 120°). This peak is lessened at 10 000 atm and a small difference is observed along $\theta = 90^\circ$. The distance between two rings are fixed to length of freely-jointed five carbon chain, theoretically having a maximum of $r = 10.78$ Å.

The 2-D contour plots for all pressure conditions are presented in Figure 5.18. The ring distance and angle are not significantly changed by increasing pressure. It appears that due to the complex and compact structure of DCMP, there is little scope for the cyclohexyl rings in DCMP to move further. Integration of this 2D plot over the angles resulted in a 1-D RDF. Figure 5.19 shows the RDF of the ring-ring distances at different pressures. At 1 atm, the RDF is peaked at about $r = 7.2$ Å with a plateau at $5.4 < r < 6.5$ Å. The distance between two centres of mass varied from just over $r = 4$ Å to $r = 8$ Å. There is little change in the RDF profiles between different pressures. The height of the peak is reduced slightly and plateau becomes smaller at 10 000 atm than at lower pressures. Again, this shows that the complex structure of DCMP limits the distance between rings.

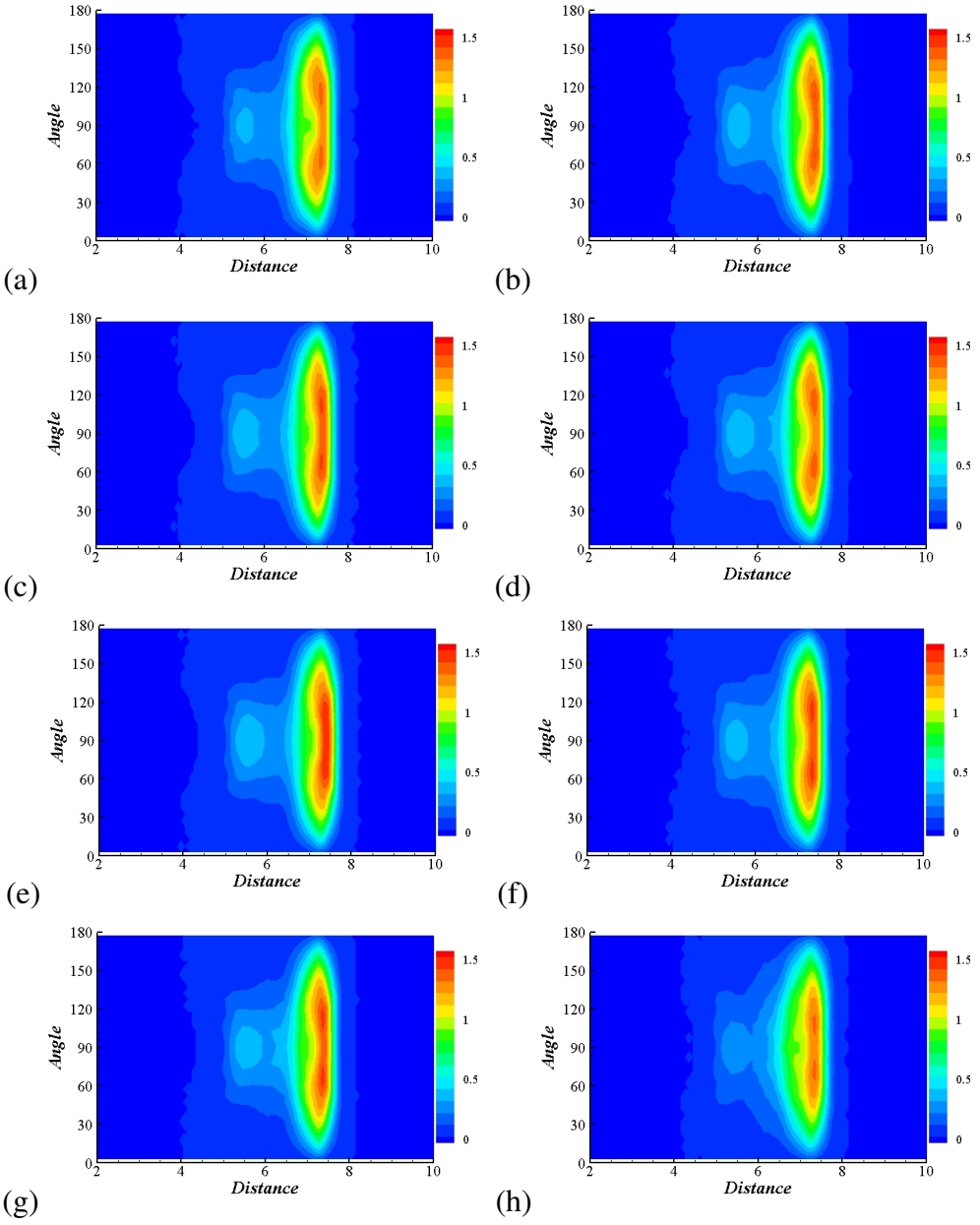

Figure 5.18: Contour plots of the ring separation distance (r_s) and the relative angle (θ) for DCMP at various pressures. (a) 1 atm, (b) 3 atm, (c) 10 atm, (d) 30 atm, (e) 100 atm, (f) 300 atm, (g) 1000 atm, (h) 10 000 atm.

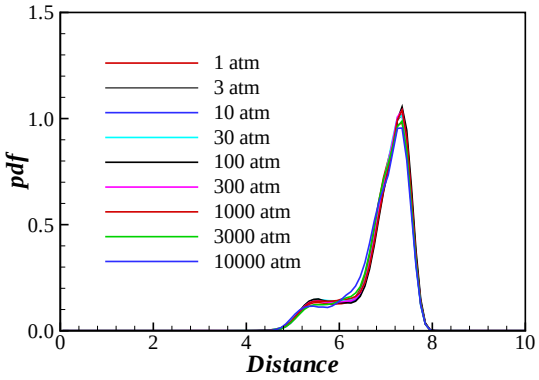

Figure 5.19: RDF of two cyclohexyl rings of a DCMP molecule at various pressures.

5.3.4 Distance and angle between rings in the system

Distances and relative angles between a cyclohexyl ring in one molecule and all other rings in the system except the one which is on the same molecule as the first reference ring were monitored. There are 2000 cyclohexyl rings in the simulation box, and there are 1999 pairs to consider. The centres of mass of rings were used to measure the distance between rings, and the angle between the normal vector of the ring plane was used to measure angles between them. The definition of the angle is presented in Figure 5.20. The blue and red lines indicate the normal vectors of the 'ring-plane' and the angle, θ, is the relative angle between these two.

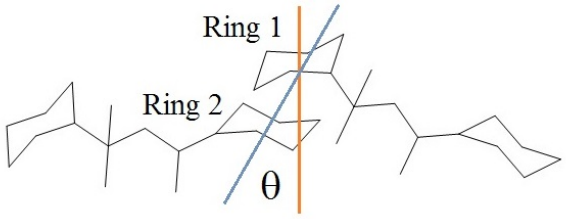

Figure 5.20: Definition of the relative angle of two rings in different molecules.

Figure 5.21 shows the distribution of rings in the simulation system as a function of distance and relative angles. There are more pairs at around $r = 6$ Å, but for $r > 10$ Å the probability is almost random over all angles. There is very little change when the pressure increases, and the little preference observed earlier weakens. Unlike Figure 5.18, the distance can reach as far as half the simulation box length since these are the distances between the rings in different molecules.

These 2D plots are integrated over all angles and plotted in Figure 5.22. As seen in the 2D plots, there is little change in the RDF profiles as the pressure increases. The peaks move inward as expected, and for 10 000 atm there is an additional smaller first peak at $r = 6$ Å.

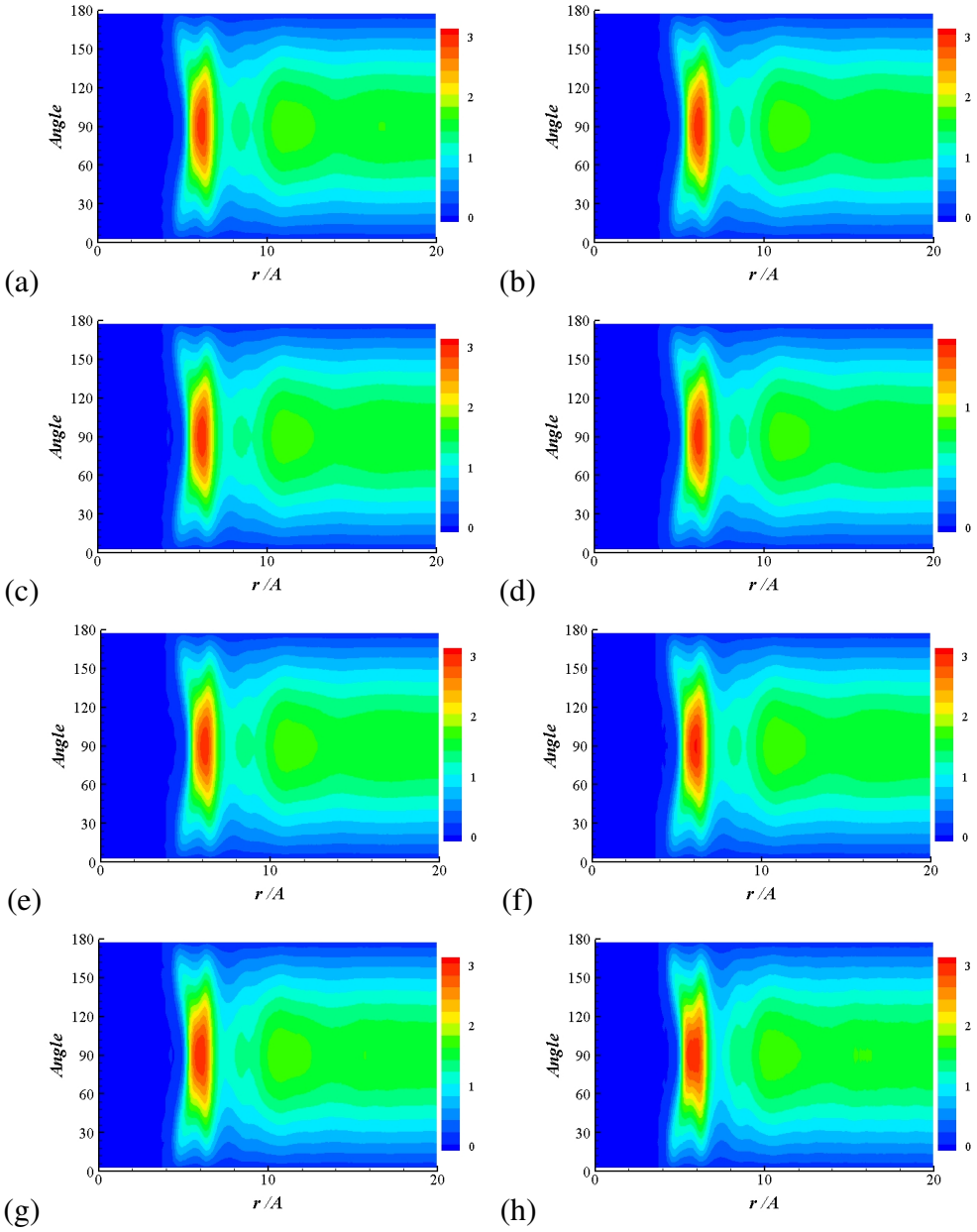

Figure 5.21: Contour maps for distance and angle of two rings of different DCMP molecules. (a) 1 atm, (b) 3 atm, (c) 10 atm, (d) 30 atm, (e) 300 atm (f) 1000 atm, (g) 3000 atm, and (h) 10 000 atm.

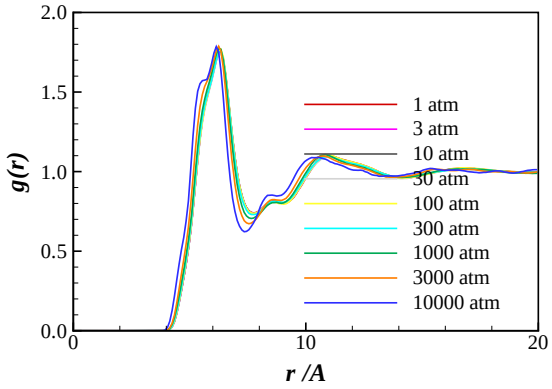

Figure 5.22: RDF for all angles of two rings from different DCMP molecules at various pressures.

Chapter 6

RESULTS: BULK PROPERTIES

Thermodynamic and transport properties of DCMP, Dumbbell, and Linear calculated from the simulations are presented in this chapter. Volume changes as a function of pressure and the subsequent density changes are calculated. Viscosities of three molecular motifs are estimated via the Stokes-Einstein relations from the self-diffusion coefficient and the radius of gyration.

6.1 Thermodynamic properties

Volume and density changes of DCMP, Dumbbell, and Linear as the simulations evolve are shown in Figure 4.9 (Chapter 4.2.3). The volume of the simulation box

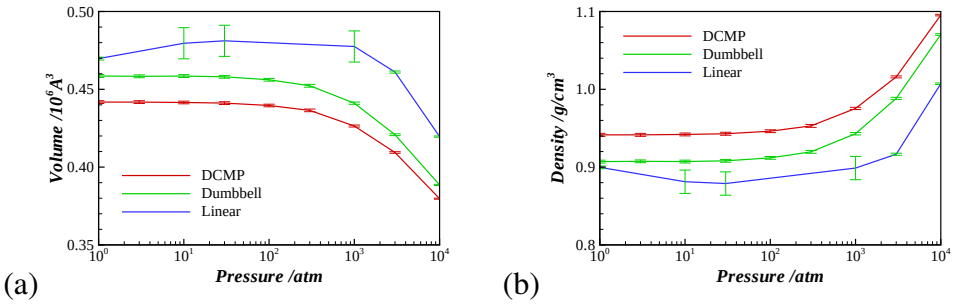

Figure 6.1: (a) Average volumes and (b) density trends of DCMP, Dumbbell, and Linear under pressures of 1 atm to 10 000 atm at 300 K. Volume is in Å^3, density in g/cm^3, and pressure in atm.

settled down fairly quickly in the time frame of the simulations and was smaller at a higher pressure. Averaged values are plotted in Figure 6.1.

Figure 6.1 shows the volume and density of DCMP and comparison molecules Dumbbell and Linear as a function of pressure. All volumes decrease as the pressure increases. Linear has the largest volume over the pressure range, and DCMP the smallest. This trend corresponds to the data in Table 4.1. The volume difference between DCMP and Dumbbell is reduced more than by half as the pressure changes from 1 atm to 10 000 atm. The volume of DCMP reduces by about 13%, of Dumbbell by 15%, and Linear by 13%. Changes in density are around 17% overall, and the change of Dumbbell is the largest.

Estimated densities of DCMP, Dumbbell, and Linear at the standard condition using data from Table 4.1 are tabulated in Table 6.1. The density of DCMP

Table 6.1: Simulation box volume and density of DCMP, Dumbbell, and Linear at the standard condition estimated from Table 4.1.

	DCMP	Dumbbell	Linear
Box Volume, 10^6 Å^3	0.4754	0.4859	0.5410
Density, g/cm^3	0.8735	0.8563	0.7814

is highest under all pressures and that of Linear the smallest. This trend is the same as experimental data in Table 6.1. However, the simulation overestimates the densities.

6.2 Transport properties

6.2.1 Mean squared displacements

Mean squared displacements (MSDs) of the centres of mass of molecules are calculated to measure the mobility of the molecules.

MSDs of DCMP, Dumbbell, and Linear at different pressures are shown in Figure 6.2. Each figure contains MSD at various pressures. In all cases, mobilities measured by MSD are reduced at higher pressures. During the first few ps, the collision between the molecules are not completely random and show parabolic behaviour. After a short while, the MSDs of molecules increase linearly. The slopes of these plots are related to the diffusion coefficient of each molecule.

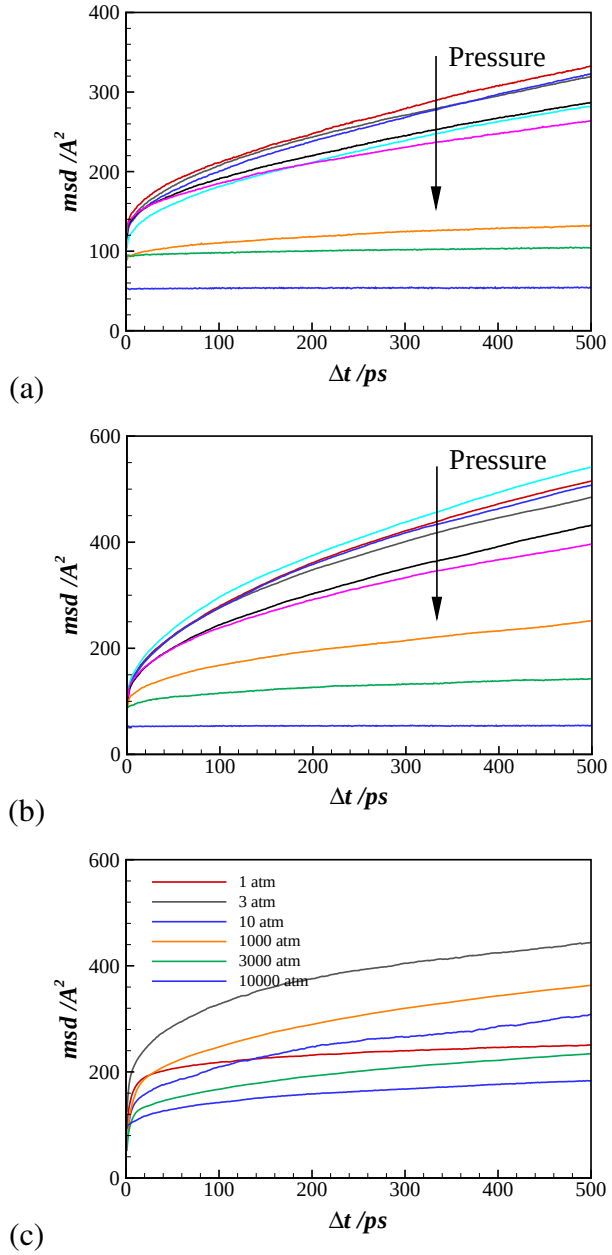

Figure 6.2: Mean squared displacement of (a) DCMP, (b) Dumbbell, and (c) Linear at various pressures. MSDs are in Å^2 and Δt in ps. The arrows indicate increasing pressure.

Figure 6.2 shows the MSDs for all three molecular motifs. Please note that the range of the coordinate for the DCMP is smaller than the range for the other two plots. As explained in the previous chapter, grouping of MSD lines of DCMP can be seen in Figure 6.2(a). At high pressures ($P \geq 1000$ atm), the mobility of the molecules reduces significantly and the gradients of the lines come close to zero. Unsurprisingly, molecules under 10 000 atm move the least. The movement is almost flat even after 500 ps and the initial MSD value is about half of that of 3000 atm system.

Dumbbell molecules in Figure 6.2(b) exhibit of similar trend as DCMP. Plots for 1 atm to 300 atm have similar behaviour, with 100 atm and 300 atm having slightly lower mobility. The MSD profiles for the first four low pressures of 1 atm, 3 atm, 10 atm, and 30 atm behave similarly, while 100 atm and 300 atm profiles are close together. Then the mobility of Dumbbell at 1000 atm reduces significantly. The mobility of Dumbbell at 10 000 atm is also close to zero, showing a near flat MSD line.

The mobility of Linear is lower than expected. The mobilities do not show a consistent trend with pressure. For example, the MSD at 3 atm is higher than that of 1 atm. MSD is the lowest at 10 000 atm which has a higher gradient than that of DCMP or Dumbbell at the same pressure. This may suggest that Linear molecules stretched to a flatter shape and made the movement easier.

6.2.2 Diffusion coefficients

Diffusion coefficients D are calculated from the slope of the MSD plots in Figure 6.2 using Equation (3.47). Figure 6.3 shows the diffusion coefficients as a function of pressure. The diffusion coefficient of DCMP at 1 atm is about $D = 0.2 \times 10^{-9}$ m^2/s and it holds this level of diffusivity up to $P = 300$ atm. Then for $P > 1000$ atm, the diffusivity drops significantly to $D = 0.005 \times 10^{-9}$ m^2/s at 10 000 atm. Dumbbell has a higher level of diffusivity compared to DCMP at all pressures. The diffusivity drops from 1000 atm. At 10 000 atm, the diffusivity of Dumbbell is about 10 times higher than that of DCMP. Diffusivity of Linear at 1 atm is lower than DCMP or Dumbbell. The diffusivity of Linear does not have same trend as DCMP or Dumbbell and it is the lowest at 1 atm. This remains at

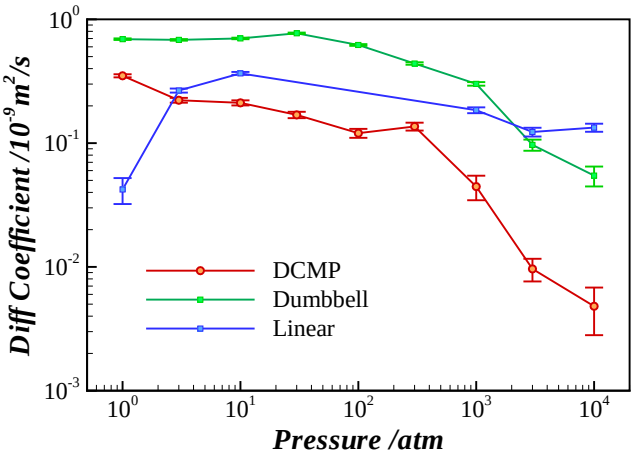

Figure 6.3: Diffusion coefficients of DCMP, Dumbbell, and Linear as a function of pressure. Pressure is in atm and the diffusion coefficient in 10^{-9}m^2/s.

the same order of magnitude with change of pressure where as the diffusion coefficient of DCMP decreases by two orders of magnitude from 1 atm to 10 000 atm.

DCMP has a more complex structure than Dumbbell or Linear. That may explain why the diffusion coefficient of DCMP is lower than diffusion coefficient of Dumbbell. Linear has an even lower diffusion coefficient. The diffusivity of Linear is the lowest at 1 atm suggesting that the long shape of Linear prevents it from moving freely.

6.2.3 Viscosities

Viscosities of DCMP, Dumbbell, and Linear are estimated from Stokes-Einstein relations, assuming that the molecules are hollow spherical molecules of the same mass and moment of inertia. Figure 6.4 shows the viscosities of the three molecular motifs. At 1 atm, Linear has the highest viscosity followed by DCMP and Dumbbell in that order. The viscosity of DCMP increases as pressure increases, and the rate of increase is greater after $P = 300$ atm. It is estimated that at $P = 10\,000$ atm, the viscosity of DCMP is over 10 000 cP. The viscosity of Dumbbell increases as pressure increases as well. However, the level of increase is smaller and it does not show a significant change in the rate of increase unlike DCMP. The viscosity of Linear also increases with increasing pressure. The vis-

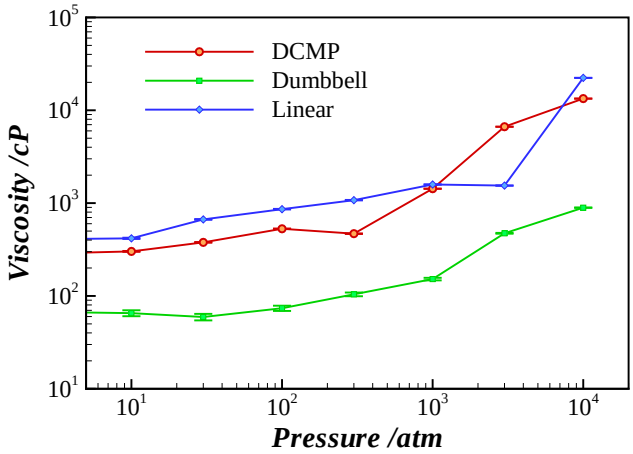

Figure 6.4: Viscosities of DCMP, Dumbbell, and Linear as a function of pressure. Pressure is in atm and viscosity in cP.

cosity of Linear is in the order of 10^3 cP at $P = 1$ atm and increases by more than an order of magnitude at $P = 10\,000$ atm.

As viscosity is inversely proportional to diffusion coefficient, the trends in viscosity against pressure for DCMP and Dumbbell are roughly inverse to their diffusion coefficients' trends. However, the viscosity trend of Linear differs from this, suggesting a reduction in R_g at high pressures. This will be further discussed in a later chapter.

Chapter 7

RESULTS: STRUCTURE ANALYSIS

Structural properties, such as the radial distribution function, the radius of gyration, the angles between molecules, and the angles between rings of the molecules are analysed in this chapter. It is also attempted to link these properties to the properties in the previous chapter.

7.1 Radial distribution functions

Radial distribution functions (RDFs) of the three molecular motifs at all pressures are presented in Figure 7.1. The DCMP plots in Figure 7.1(a) indicate that the first peaks for all pressures are at around $r = 8$ Å. All but the two highest pressures follow a similar trend. The first peak for $P = 3000$ atm moves inwards, and the peak of $P = 10\,000$ atm shows two local maxima around $r = 8$ Å. The trough of $P = 10\,000$ atm has a "double-dip" as well. The RDF of 10 000 atm is less well defined compared to the lower pressure systems.

Radial distribution functions (RDFs) of the three molecular motifs at all pressures are presented in Figure 7.1. The DCMP plots in Figure 7.1(a) indicate that the first peaks for all pressures are at around $r = 8$ Å. All but the two highest pressures follow a similar trend. The first peak for 3000 atm moves inwards, and the peak of 10 000 atm shows two local maxima around $r = 8$ Å. The trough of 10 000 atm has a "double-dip" as well. The RDF of 10 000 atm is less well defined compared to the lower pressure systems.

Dumbbell profiles in Figure 7.1(b) start from very small r values. This corresponds to the distance between the centres of mass. With Dumbbell being a relatively long 'string' of carbon single bonds with cyclohexyl rings on both end, this may allow for the centres of mass of two Dumbbell molecules to approach

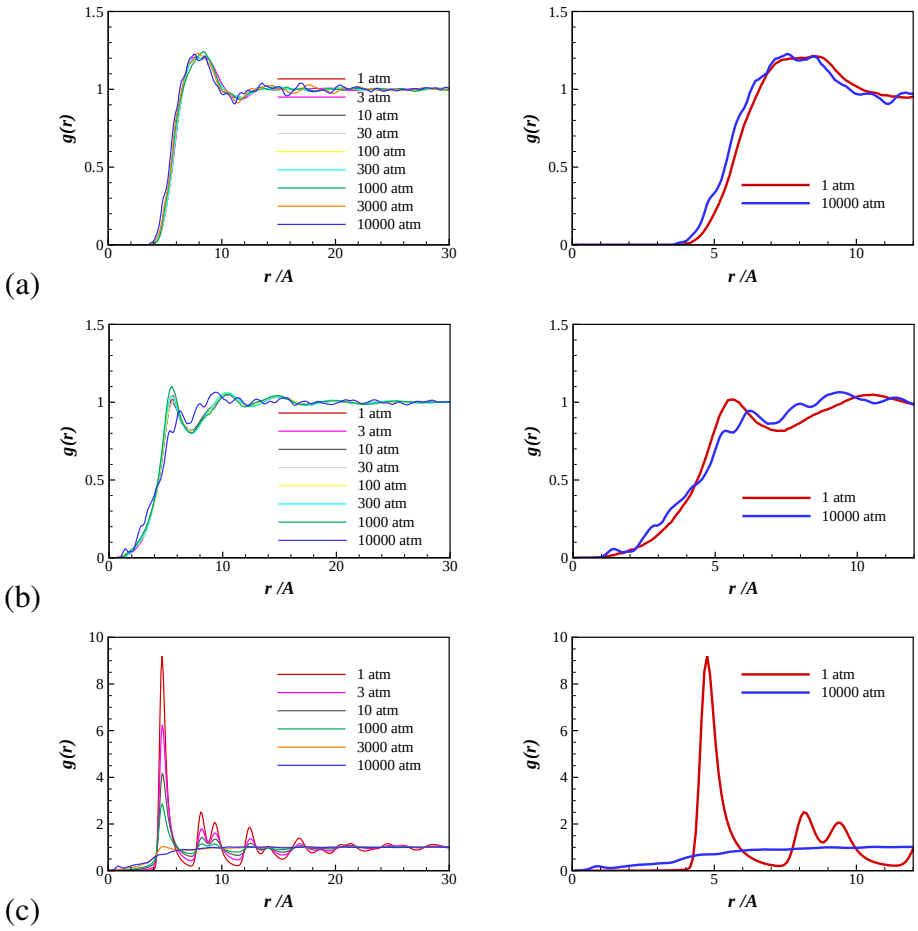

Figure 7.1: Radial distribution functions and their close-ups of (a) DCMP, (b) Dumbbell and (c) Linear. All pressures are plotted on the left and close-up of two extreme pressures on the right. Inter-molecular centre of molecule distance, r is in Å.

close to each other. At all pressures, the centres of molecules can come as close as $r = 1$ Å from each other. Dumbbell molecules at $P = 10\,000$ atm can come even closer to each other, but the peak is smaller than the distance where all other RDF profiles have the first peaks. There is a small peak at around $r = 1$ Å, and another

near $r = 3$ Å, whereas most of the pressures have the first peak at around $r = 6$ Å. Also, Dumbbell at $P = 10\,000$ atm has small oscillations for all r values.

In contrast, Linear molecules have a very defined RDF and the first peaks are very pronounced as shown in Figure 7.1(c). At $P = 1$ atm, the distribution of the centres of mass at around $r = 5$ Å is about 9 times higher than the bulk average. As pressure increases the height of the first peaks reduces, while the position of the peaks remain the same until $P = 1000$ atm. The differences between systems at high and low pressures are better shown in Figure 4.10 in Chapter 5. At $P =$ 3000 atm, the RDF profile shifts dramatically to a very low, broad one, and the profile at $P = 10\,000$ atm shows a plateau rather than a peak after $r = 6$ Å.

The short distance region ($r < 12$ Å) of RDFs at $P = 1$ atm and $P = 10\,000$ atm is shown in Figure 7.1. The shape and height of peaks are broadly similar between the different pressure conditions, with the lower pressure profile being smoother and the higher pressure profile containing small oscillations. Centres of mass of DCMP are located closer to each other at $P = 10\,000$ atm than at $P = 1$ atm, but the difference is rather small. The RDFs of 1 atm and 10 000 atm at a close range from $r = 1$ Å to $r = 12$ Å are shown in Figure 7.1. DCMP at $P = 1$ atm and at $P = 10\,000$ atm follows a similar trajectory, although under high pressure the molecules come closer to each other and the RDF line is less defined. The peaks are located at the same distance but $P = 1$ atm has a broader peak

while $P = 10\,000$ atm shows two smaller peaks. 1 atm has a smooth RDF profile, whereas 10 000 atm has a greaters number of smaller peaks or 'bumps'.

Dumbbell shows some difference between 1 atm and 10 000 atm. The RDF profile at $P = 1$ atm has smooth peaks and troughs with the first peak at near $r = 6$ Å, whereas the RDF at $P = 10\,000$ atm shows small oscillations. While the highest peak at $P = 1$ atm is at around $r = 5$ Å, the peak for $P = 10\,000$ atm is near $r = 9$ Å with multiple small peaks superimposed. The height of peaks is lower than that of DCMP or Linear, indicating that the centres of mass of Dumbbell molecules are well spread except very close distances. Also the nearest non-zero $g(r)$ distance is much closer than that of other molecules.

Linear shows the largest differences in RDFs between different pressure cases, as shown in figure 7.1. The RDF profile at $P = 1$ atm shows a dominant peak at about $r = 5$ Å, with the height over 9, then smaller peaks at around $r = 8.5$ Å and 9.5 Å. All these three peaks are much larger than 2, whereas the amplitude of the first peaks of DCMP and Dumbbell are less than 1.5. The RDF of Linear at 10 000 atm shows a much broad distribution with the first peak or a 'bump' being at about $r = 0.5$ Å.

7.2 Radius of gyration

The distribution of the radius of gyration, R_g, is shown in Figure 7.2. Two pressure conditions are considered: $P = 1$ atm (Figure 7.2(a)) and $P = 10000$ atm (Figure 7.2(b)). The R_g peak of DCMP is the smallest at about $R_g = 3.5$ Å, and that of Linear is the largest at about $R_g = 6.5$ Å. The R_g peak of Dumbbell lies between the two at around $R_g = 4.7$ Å. This R_g value reflects the relative length of the backbone of DCMP, Dumbbell, and Linear, Linear being the longest alkane. DCMP is the most compact of the three and has the shortest backbone. The R_g values of Linear and DCMP show a very sharp peak each whereas R_g of Dumbbell has a wider and lower peak. All molecule types have one distinctive peak with a spread of $\Delta R_g = 1$ - 2 Å. At $P = 10000$ atm, DCMP shows a similar R_g shape as at $P = 1$ atm, but Dumbbell has developed a smaller second peak at around $R_g = 3.5$ Å. The biggest change occurs for Linear. Now the R_g has the broadest peak among the three and there is a new peak formed at about $R_g = 3.5$ Å and a less distinctive peak at around $R_g = 5.5$ Å. This is due to Linear being a long chain alkane. This behaviour can be found in long polymer chains due to their flexible nature. Change in R_g implies that the shape of the molecule has changed from a long thin shape to more round and compact one.

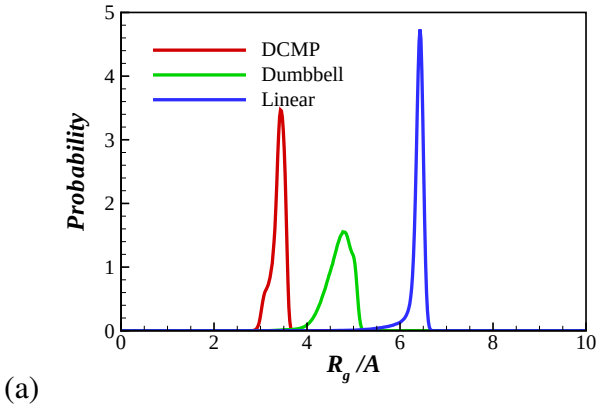

(a)

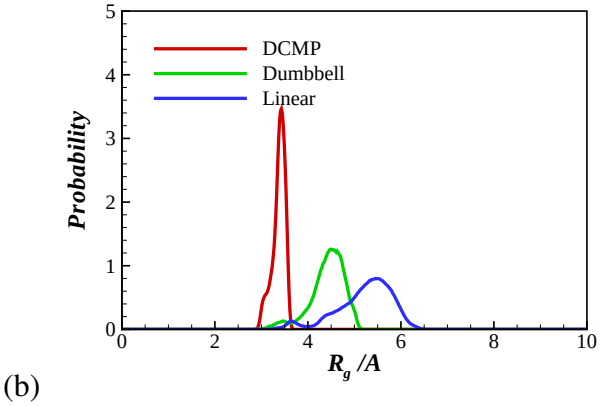

(b)

Figure 7.2: Distribution of radius of gyration, R_g, of DCMP, Dumbbell, and Linear molecules at (a) 1 atm and (b) 10 000 atm. R_g is in Å.

7.3 Relative positions of molecules

The relative positions of DCMP molecules in the simulation box are compared with Dumbbell and Linear.

7.3.1 Effect of methyl 'hooks'

Similar to Figure 5.10, the distribution of Dumbbell molecule pairs as a function of angles and centre of mass distances are presented in Figure 7.3. Red, blue, and green colours represent the highest, the lowest, and the bulk average frequency.

There are two peaks or preferred areas from ($r = 4$ Å and $\theta = 50^\circ$) to ($r = 6$ Å and $\theta = 10^\circ$). Dumbbell pairs prefer parallel angles when they are less than $r = 6$ Å apart. At around $r = 8$ Å, all angles larger than 30° have equal probability. For $r > 8$ Å, the pairs prefer to be at $\theta = 90^\circ$. This pattern remains the same until $P = 1000$ atm. At $P = 10\,000$ atm, the small peak at a close distance almost disappears and disperses into yellow dots along $r = 6$ Å.

DCMP and Dumbbell at $P = 1$ atm are compared in Figure 7.4. More DCMP molecule pairs are found at around $r = 9$ Å and $\theta = 90^\circ$, and the probability of finding a pair at large distances is uniform. Dumbbell has most populous area around $r = 6$ Å in the parallel position ($\theta = 90^\circ$). Also the centre of mass distance of Dumbbell pair can be as small as $r = 1$ Å. As shown in Figure 7.4(c), the 'maximum' line for the DCMP pair at about $r = 9$ Å shows consistently higher $g(r)$ than the average of blue line for $\theta > 30^\circ$. Looking at $r = 7$ Å distance, $\theta = 30^\circ$ is preferred to 60°, and there is another peak at $\theta = 90^\circ$. Figure 7.4(d) shows a lower 'maximum' peak of Dumbbell at $r = 10.5$ Å. This thick red line is

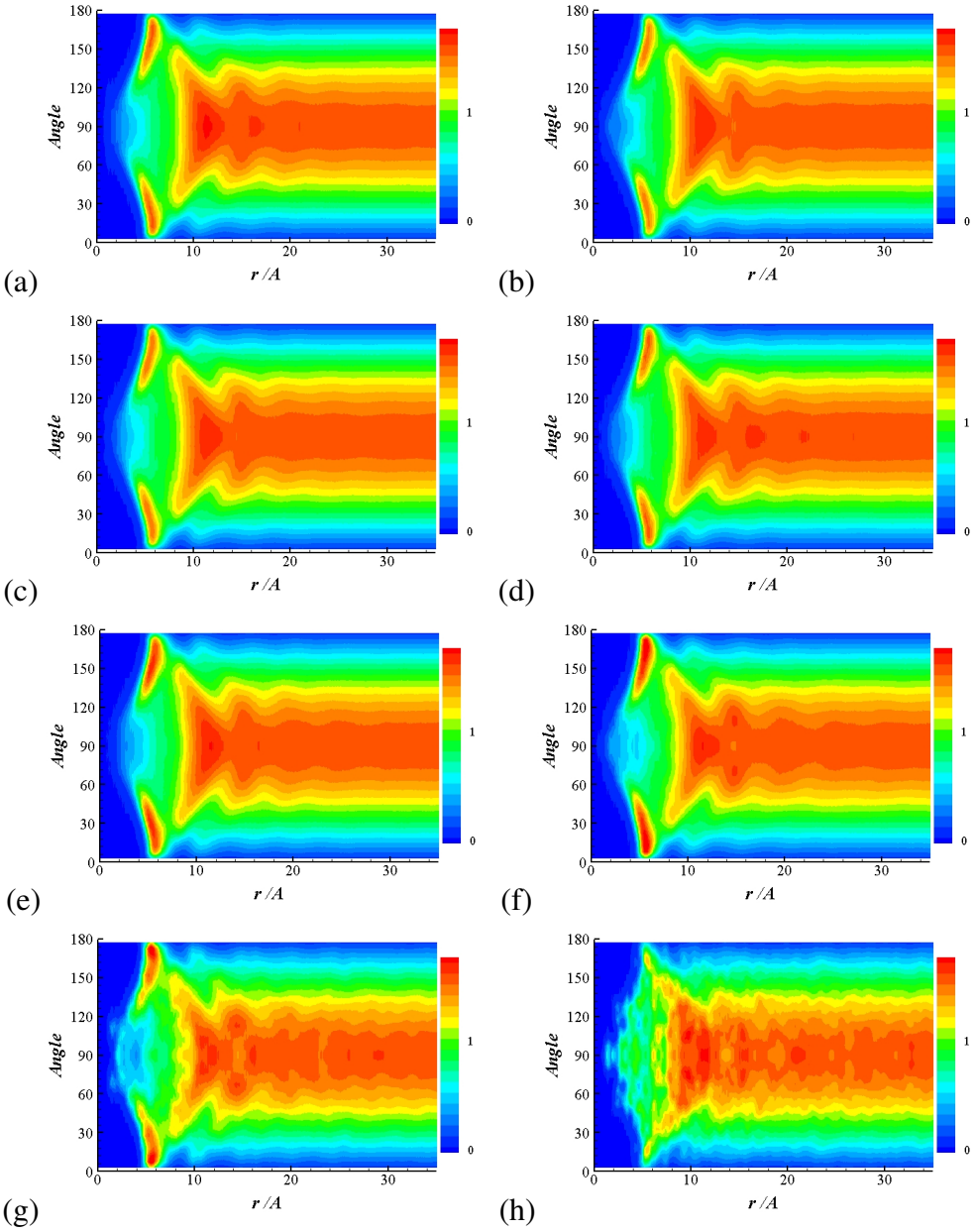

Figure 7.3: Contour maps of distance and angle of a pair of Dumbbell molecules at (a) 1 atm, (b) 10 atm, (c) 30 atm, (d) 100 atm, (e) 300 atm, (f) 1000 atm, (g) 3000 atm, and (h) 10 000 atm.

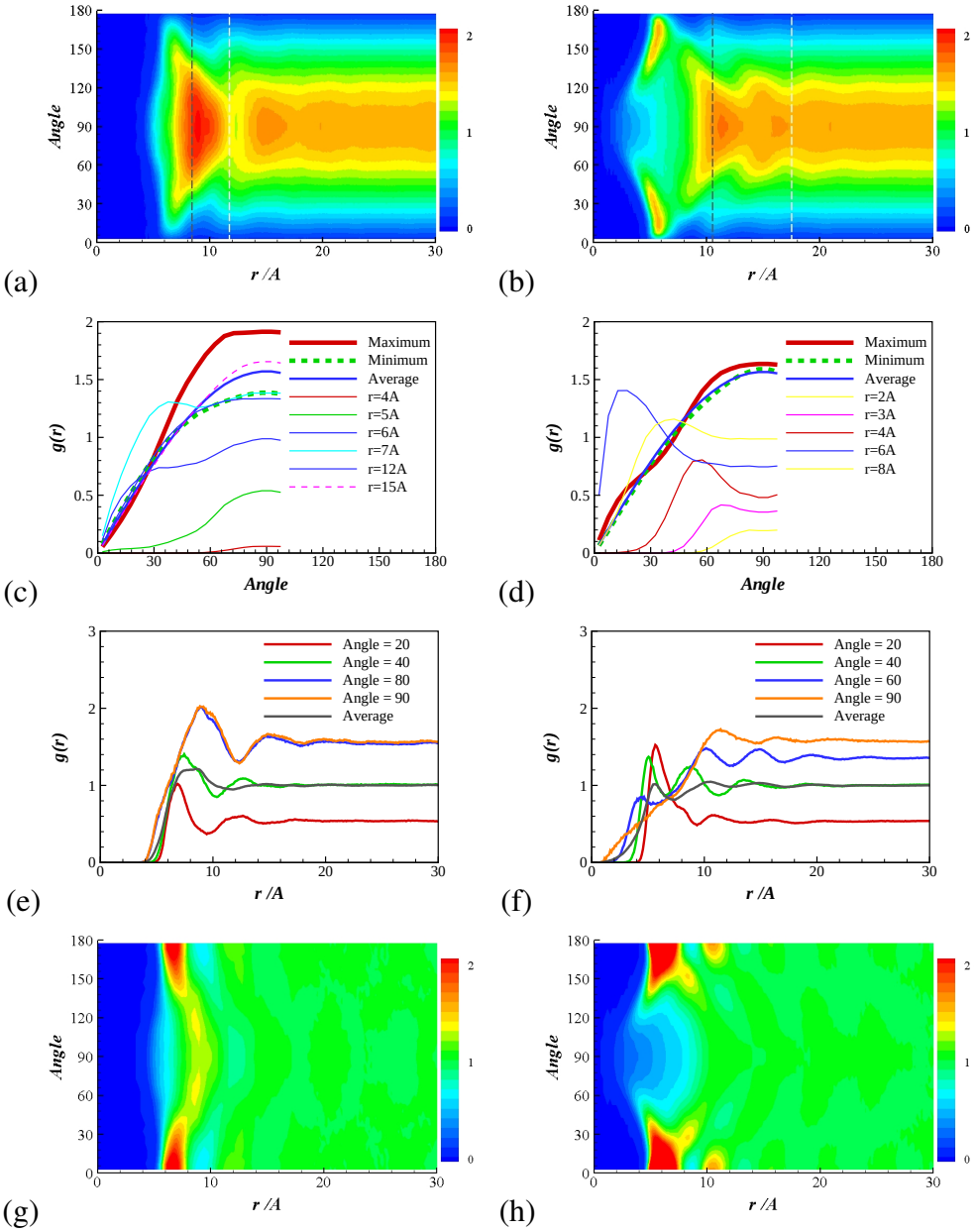

Figure 7.4: Distance and relative angles of DCMP (left) and Dumbbell (right) molecules at $P = 1$ atm. Distance between the centre of molecules in Å and angle between the molecules in degrees.

very similar to the average line.

However, the $g(r)$ profile at the 'maximum' distance is slightly higher than the average line between $\theta = 0^\circ$ and $\theta = 30^\circ$, then lower than the average between $\theta = 30^\circ$ and $\theta = 50^\circ$, and then higher between $\theta = 50^\circ$ and $\theta = 90^\circ$. Figure 7.4(e) indicates molecular pairs at $\theta = 90^\circ$ occur mainly at about $r = 9$ Å and then at about $r = 15$ Å. The profile at $\theta = 20^\circ$ has the first peak near $r = 6$ Å and the second peak near $r = 12$ Å. Dumbbell molecules can move much closer to each other as seen in Figure 7.4(f). Molecule pairs at $\theta = 90^\circ$ can be as close as $r = 1$ Å although the first peak is at $r = 11$ Å. Please note that this distance is the centre of mass distance and should be interpreted with care, but Dumbbell which has a longer, therefore more flexible backbone, can have a wide range of r values. Otherwise angled pairs have the first peaks at closer distances. The RDF profiles at $\theta = 20^\circ$ and $\theta = 90^\circ$ have less prominent second peaks, and $\theta = 60^\circ$ has a higher second peak than the first peak.

Concentration of the molecule pairs are shown better using cosine-bins in Figures 7.4(g) and 7.4(h). It becomes clearer that at $P = 1$ atm, DCMP pairs prefer $r = 6$ - 8 Å and $\theta = 0^\circ$. Perpendicular pairs begin to show at similar distances, but slightly closer or farther than this. The peak for $\theta = 90^\circ$ is located at $r = 8$ - 9 Å. Dumbbell also has the main preferred area along parallel position, but at closer distances of $r = 5$ - 8 Å. Then there is the second peak area near $r = 10$ Å.

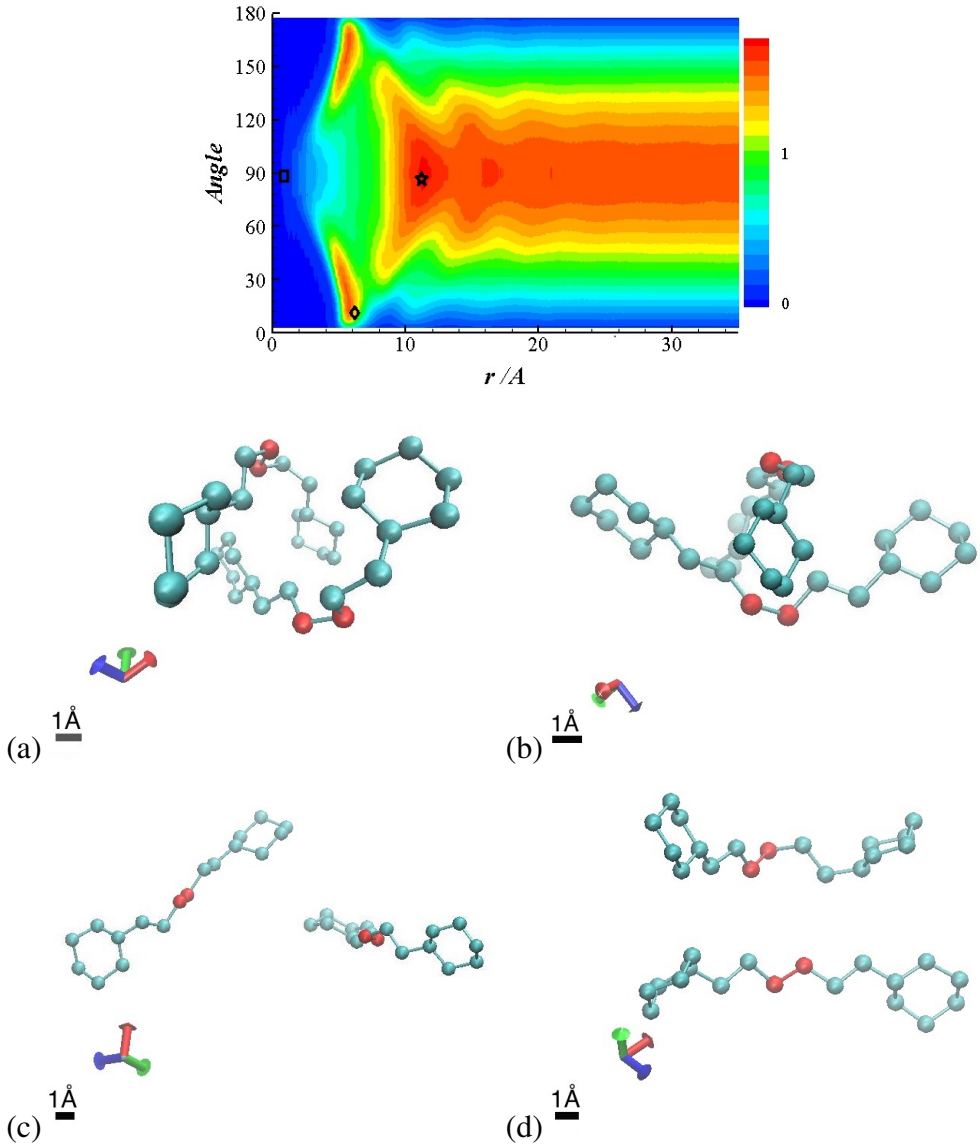

Figure 7.5: Dumbbell molecule pairs of selected points from the 2D contour plots at $P = 1$ atm. (a) and (b) square (1 Å and 90°), (c) star (11 Å and 90°), and (d) diamond (6 Å and 12°).

Perpendicular pairs are found in a much nearer region compared to DCMP. The

nearest pairs are located at $r < 4$ Å. There is ripple-like pattern along the $\theta = 90^\circ$ line.

Selected Dumbbell molecule pairs at $P = 1$ atm are presented in Figure 7.5. Dumbbell molecules are coloured green and the two united atoms in the middle of a molecule are marked red. Figures 7.5(a) and 7.5(b) show pairs whose centre of mass distances are less than $r = 2$ Å. They bend slightly and rings are in alternating corners to accommodate the other molecule and lie at $\theta = 90^\circ$ to each other. On the contrary, the pair in Figure 7.5(c) is at $\theta = 90^\circ$ but each molecule is straighter. This Dumbbell pair is taken from the most popular area marked with a star in the 2D RDF plot. The parallel pairs (marked with a diamond) are mostly found at around $r = 6$ Å. An example is shown in Figure 7.5(d).

DCMP and Dumbbell molecules at $P = 10000$ atm are compared in Figure 7.6. Still, $\theta = 90^\circ$ is popular for DCMP pairs but now the peak area looks like a cluster of smaller peaks in Figure 7.6(a). In Figure 7.6(b), the nearest peak located at $r = 6$ - 7 Å and in the parallel region is disappeared. Compared to DCMP in Figure 7.6(c), RDF profiles in Figure 7.6(d) show that the angles and distances of Dumbbell molecular pairs are scattered over a wider range than at $P = 1$ atm. Dumbbell pairs are found at shorter distances than DCMP pairs as shown in Figures 7.6(e) and 7.6(f). The nearest distance that DCMP pairs are found is about $r = 4$ Å whereas Dumbbell pairs can come as near as $r = 1$ Å

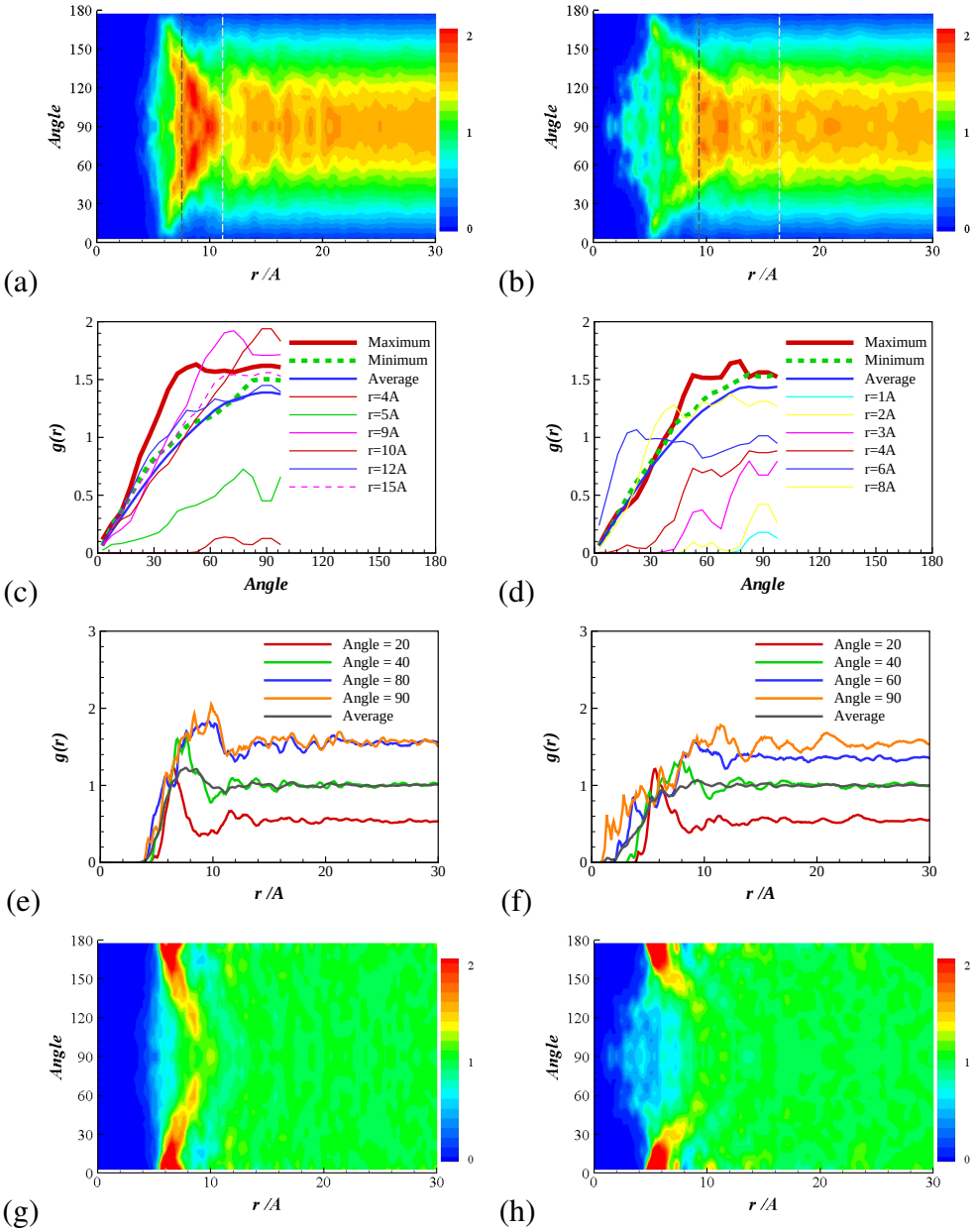

Figure 7.6: Distance and relative angles of DCMP (left) and Dumbbell (right) molecules at 10 000 atm. Distance between the centre of molecules in Å and angle between the molecules in degrees.

of each other. Using cosine-bins, Figure 7.6(g) shows that DCMP pairs are most concentrated at around $r = 6$ Å and in the parallel region ($\theta = 90^\circ$). These peak angles are becoming larger with increasing r. Also the height of peaks are becoming smaller. The hot spot for Dumbbell is found at around $r = 5$ - 6 Å and $\theta = 0$ - 20°. This hot spot is not as large as in the DCMP molecules. Ripple-like patterns are observed at small distances for both molecules.

Selected Dumbbell molecule pairs at $P = 10000$ atm are shown in Figure 7.7. A pair located closest to each other, marked with a square in the 2D plot, is shown in Figure 7.7(a). When the molecules are close, they tend to bend to reduce the contact area as observed at $P = 1$ atm. In this case, one is folded and the other is almost straight. The Dumbbell pair shown in Figure 7.7(b) is also perpendicular to each other. This pair lie further away from each other at around $r = 9.4$ Å, and both molecules are relatively straight. Figure 7.7(c) is a pair from the area marked with a triangle. They are about $r = 8$ Å apart and $\theta = 70^\circ$. Again, both molecules are relatively straight. The parallel pair in Figure 7.7(d) look similar to the pair in Figure 7.5(d), but are still not parallel to each other.

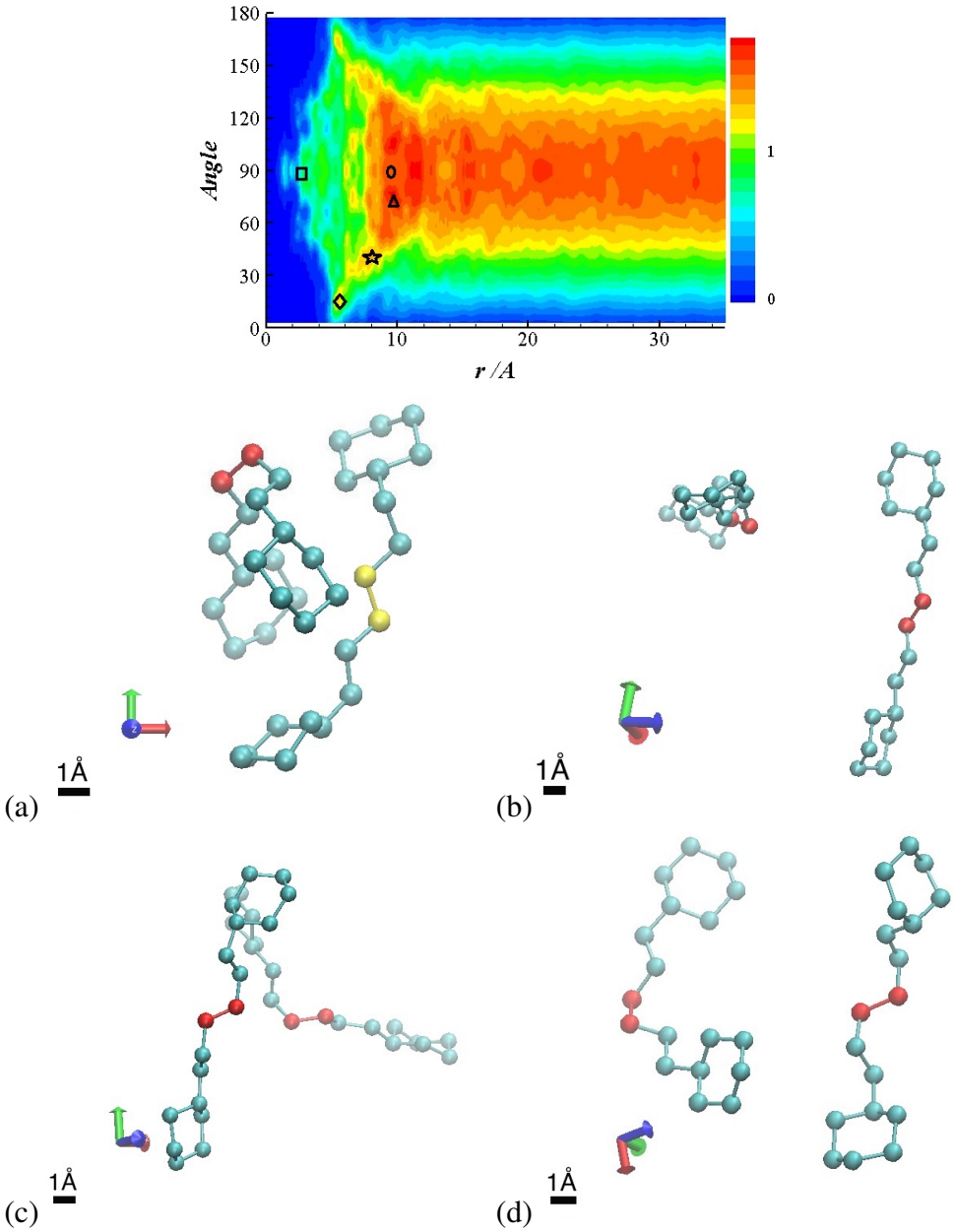

Figure 7.7: Example of Dumbbell molecule pairs for selected points from the 2D contour plots at $P = 10000$ atm. (a) square (3 Å and 90°), (b) circle (9.4 Å and 90°), (c) triangle (10 Å and 70°), and (d) star (8 Å and 45°).

7.3.2 Effect of cyclohexyl rings

Linear molecules do not have cyclohexyl rings like DCMP or Dumbbell molecules, and show rather different pairing characteristics. Distribution of Linear pairs as a function of centre of mass distance and angles between the molecules are presented at different pressures in Figure 7.8. At $p = 1$ atm, there are two distinctive regions, and the parallel arrangements are preferred from $r = 4$ Å all the way to $r = 30$ Å. These areas have regular occurrence, suggesting a lining up of the molecules. The same red hot spots are seen at perpendicular positions at distances for $r > 16$ Å. At short distances of $r < 12$ Å, almost all molecules are parallel

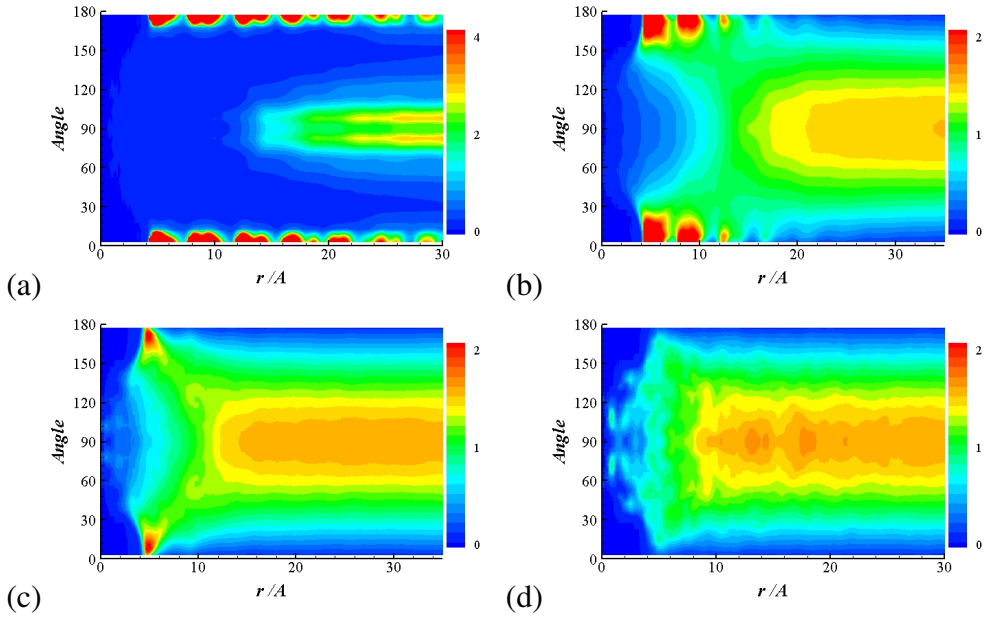

Figure 7.8: Contour plots of distance and angle of a pair of Linear at (a) 1 atm, (b) 1 000 atm, (c) 3 000 atm and (d) 10 000 atm.

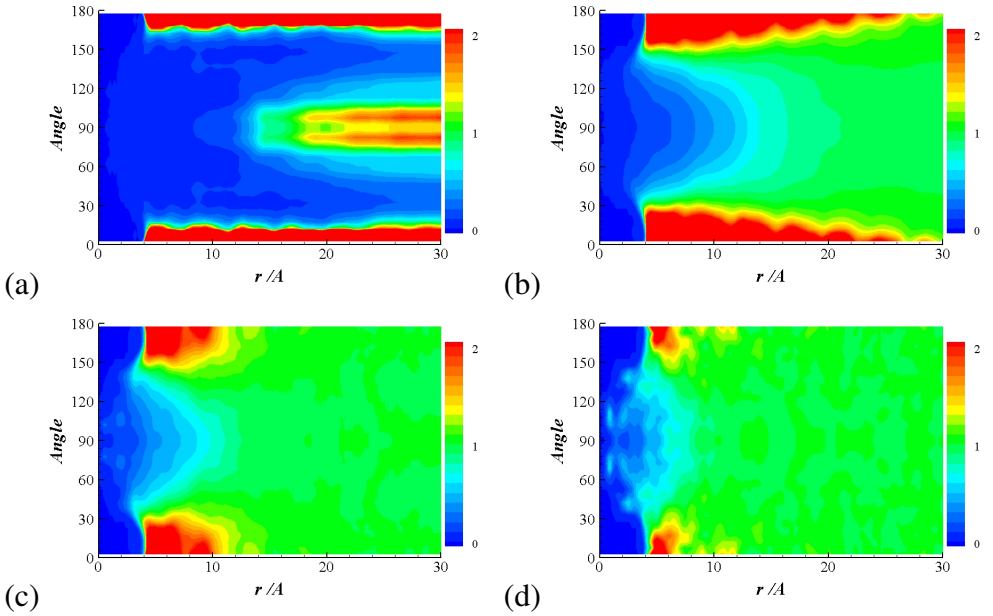

Figure 7.9: Contour plots of Linear molecular pairs as a function of distance and angle using cos-bins at (a) 1 atm, (b) 1 000 atm, (c) 3 000 atm, and (d) 10 000 atm.

to each other. For $r > 16$ Å, they are either perpendicular or parallel, but not in-between.

This strong preference weakens as the pressure increases: the high probability region at large distances disappears and the perpendicular peaks weaken too; more intermediate angles appear. At 3000 atm, red spots remain only at a distance of $r = 5$ Å distance. The preference is even weaker at $P = 10000$ atm, and all hot spots are disappeared. For $5 < r < 9$ Å, the RDF profile has the average concentration of molecular pairs. The RDF profiles are also drawn using cosine-bins in Figure 7.9. The preference for the parallel alignment at lower pressures is more

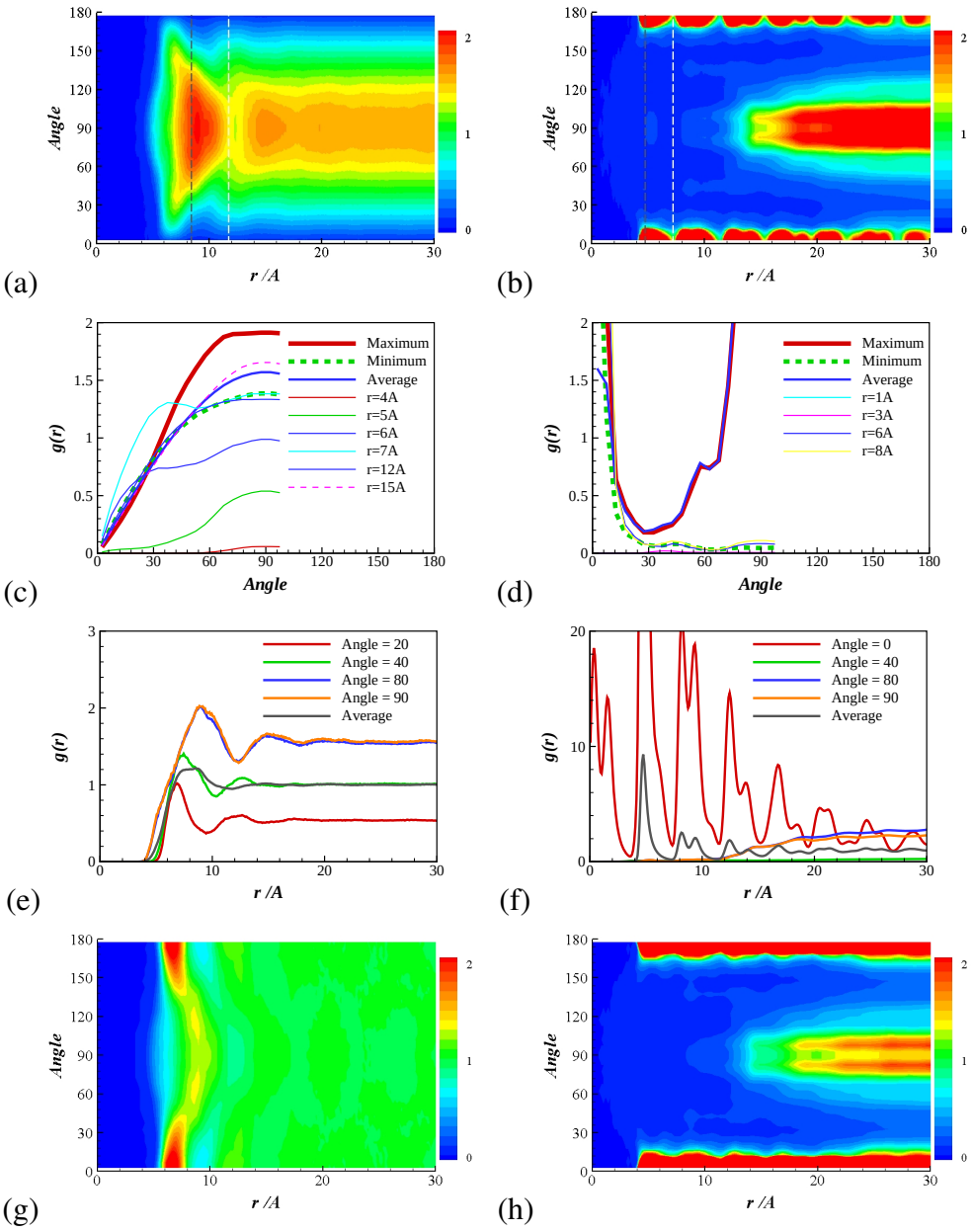

Figure 7.10: Contour plots of molecule pair distance and relative angles of DCMP (left) and Linear (right) at $P = 1$ atm. Distance between the centre of molecules in Å and angle between the molecules in degrees.

prominent.

Figure 7.10 compares the RDF at $P = 1$ atm of DCMP and Linear. At $P = 1$ atm (Figure 7.10(a)), red peaks are present as a band at all distances, and for $r > 14$ Å the secondary peaks appear along $\theta = 90^\circ$. There is a very strong 'exclusion' zone where no Linear pairs are found. As the pressure increases, the red area disappears gradually. The blue areas are also reduced and show ripple-like patterns as in DCMP and Dumbbell. At $P = 3000$ atm the red peak patterns look similar to DCMP or Dumbbell, having peak areas at $r = 4$ - 10 Å and $\theta = 0$ - 30°. At $P = 10000$ atm, the red peak areas are much smaller and the pairs are found at much shorter distances. At the two highest pressures, pairs are found at very short distances around $\theta = 90^\circ$.

Linear molecules at $P = 1$ atm have prominent peaks along $\theta = 0^\circ$ line, unlike DCMP pairs whose strong preference decays quickly after a certain distance. There is high preference to avoid $\theta = 30^\circ$ as shown in Figure 7.10(d). $\theta = 0^\circ$ and $\theta = 90^\circ$ peaks are too high to be included in this plot. RDF values for $\theta = 40^\circ$ are almost zero in Figure 7.10(f). $\theta = 0^\circ$ case shows a periodic fluctuation. $\theta = 90^\circ$ begins to appear for $r > 11$ Å. Figures 7.10(g) and 7.10(h) are 2-D contour plots using cosine-bins. The preference of Linear molecule pairs for the parallel position at all distances over $r = 4$ Å is more visible here.

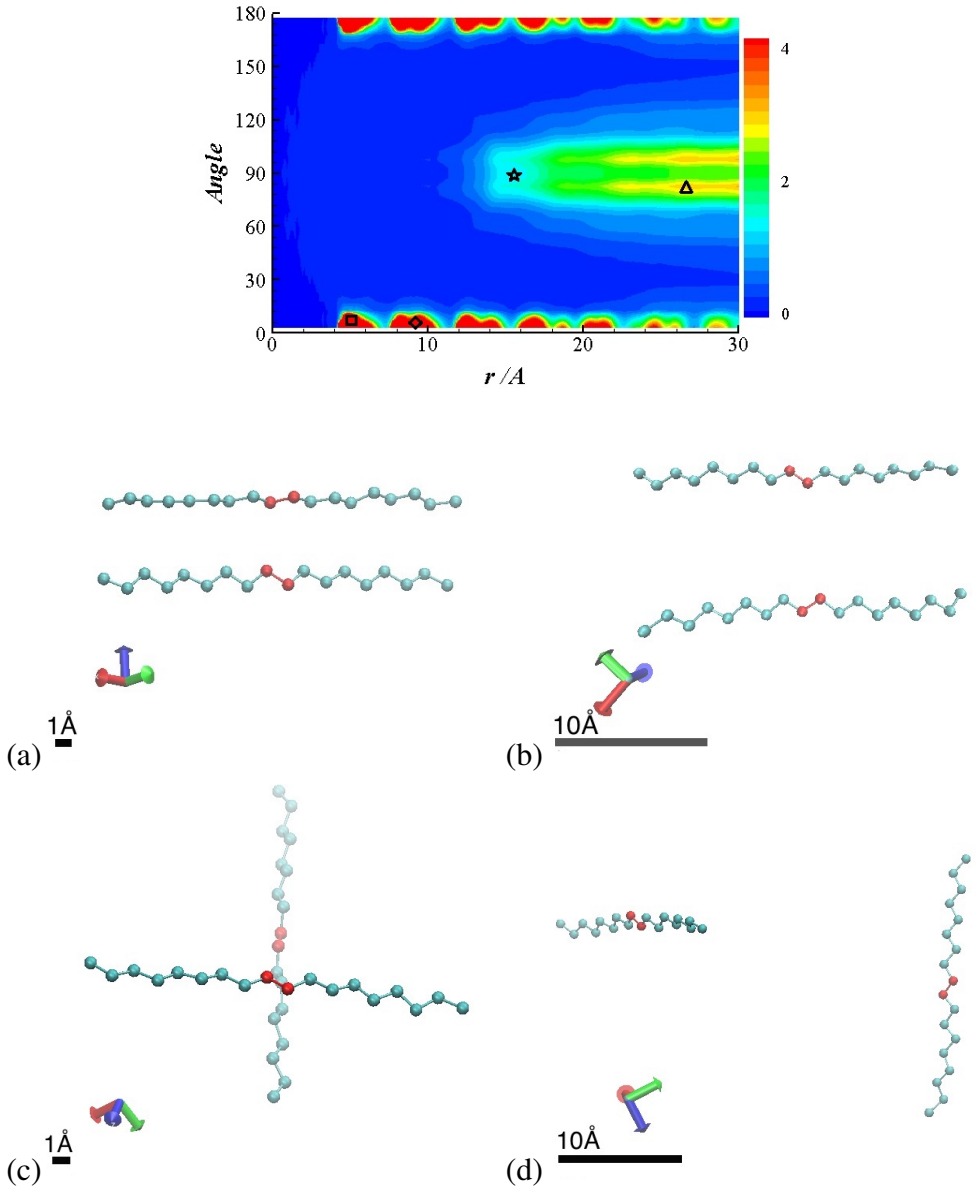

Figure 7.11: Linear molecule pairs for selected points in 2D contour plots. Linear at 1 atm. (a) square ($r = 5$ Å and $\theta = 0°$), (b) diamond ($r = 9$ Å and $\theta = 0°$), (c) star ($r = 15$ Å and $90°$), and (d) triangle ($r = 26$ Å and $\theta = 80°$)

Figure 7.11 shows example configurations of Linear molecule pairs. The

Linear pair in Figure 7.11(a) is taken from the point marked with a square near $r = 5$ Å and $\theta = 0^\circ$ in the 2D RDF plot. The two relatively straight molecules are in close proximity and parallel to each other. The pair in Figure 7.11(b) and also straight, parallel molecules, only with a larger distance. This pair is taken from the second peak area of $r = 9$ Å and $\theta = 0^\circ$. Figures 7.11(c) and 7.11(d) are taken from the $\theta = 90^\circ$ area. They are straight and shows a cross position, only with different centre of mass distances. All example molecule pairs shown here are straight, in contrast with Dumbbell molecules in the parallel position. Dumbbell molecules in the parallel position are bent slightly.

DCMP and Linear molecular pairs at $P = 10\,000$ atm are compared in Figure 7.12. Linear molecule pairs are found at very short distances. The smallest distance of a parallel pair (20°, red line in Figure 7.12(f)) is about $r = 4$ Å, but other angles plotted here are found from $r = 0$ Å. The preference of Linear pairs for the parallel position has decreased and now is confined to smaller areas as shown in Figure 7.12(h). Compared to DCMP pairs, Linear pairs have smaller and more prominent area of preference, and the light blue area at $\theta = 90^\circ$ is wider.

Snapshots from selected points in the 2D contour plot are presented in Figure 7.13. First, the pair with the shortest distance, marked as a square, is shown in Figure 7.13(a). Unlike pairs at $P = 1$ atm, the molecules are bent slightly. The distances between red atoms in the middle of molecules are not as small as

$r = 1$ Å.

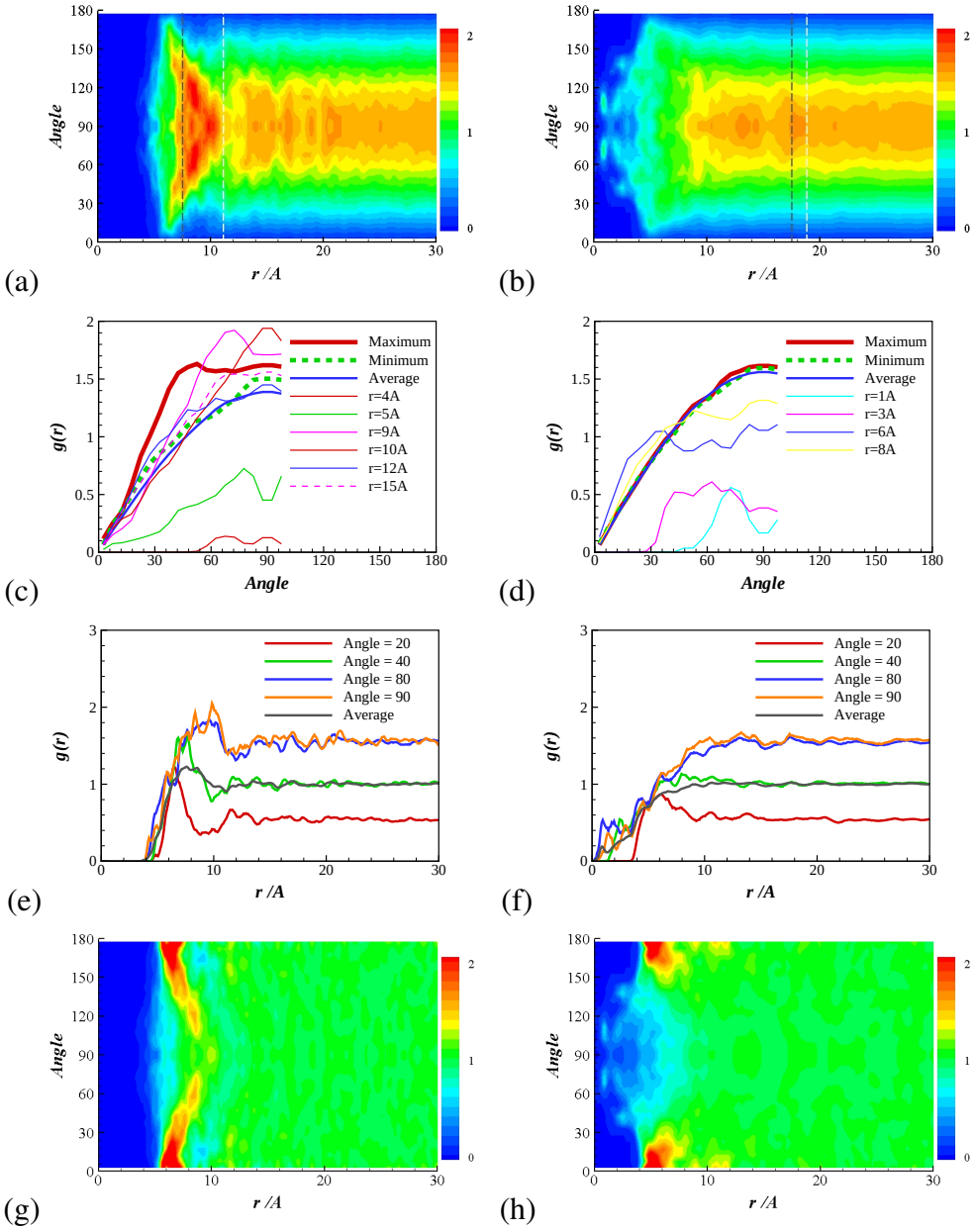

Figure 7.12: Distance and relative angles of DCMP (left) and Linear (right) molecules at $P = 10000$ atm. Distance between the centre of molecules in Å and angle between the molecules in degrees.

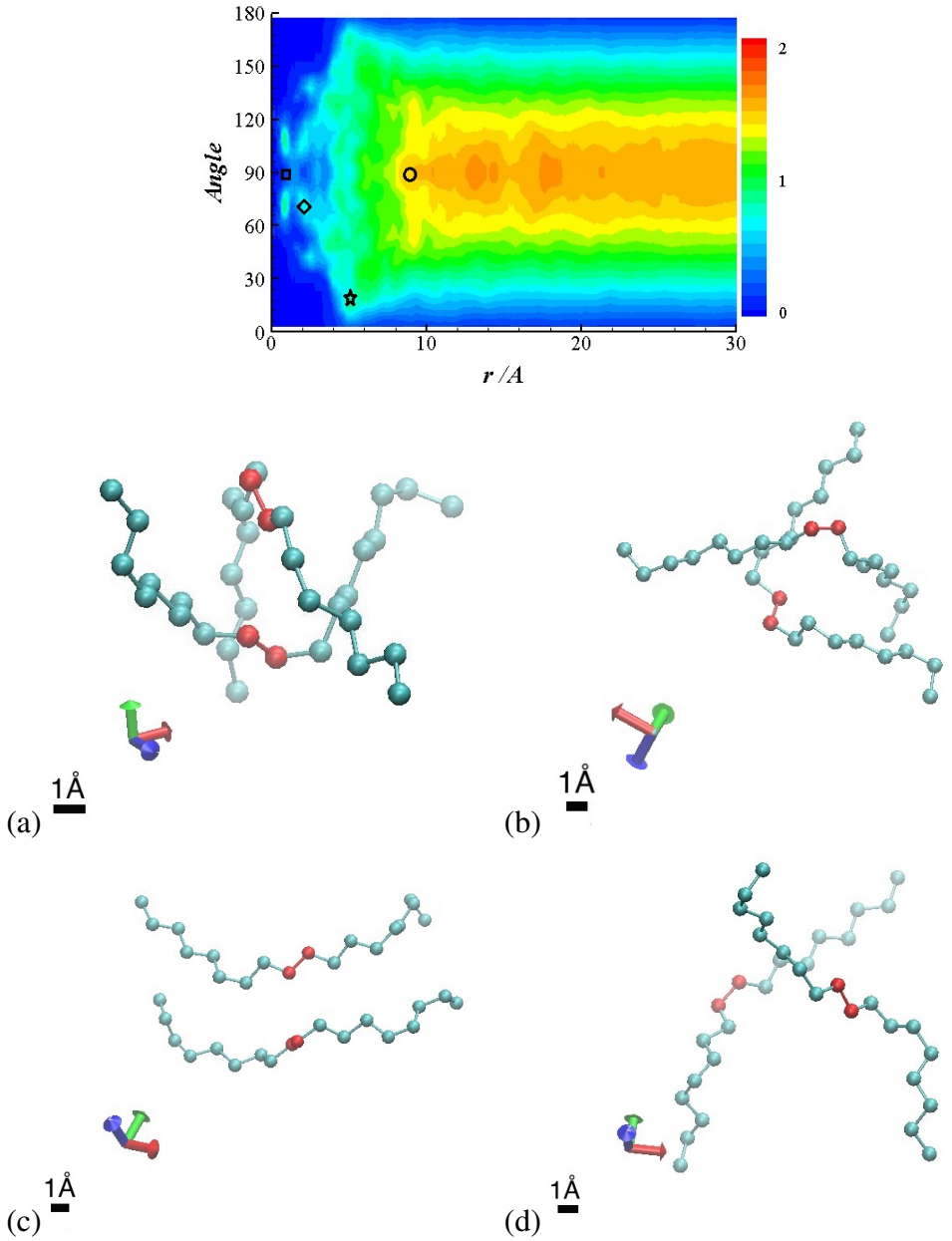

Figure 7.13: Linear molecule pair for selected points in 2D contour plots. Linear at $P = 10\,000$ atm. (a) square (1 Å and 90°), (b) diamond (2 Å and 70°), (c) star (5 Å and 20°), and (d) circle (9 Å and 90°)

The arc shape of the molecules moves the centre of mass of the molecules outside of the backbone of the molecule itself, and as a result, the distance between centres of mass becomes very small. A nearby molecule pair is presented in Figure 7.13(b). They are slightly further away from each other than the pair in Figure 7.13(a), but their overall shapes are similar. Figure 7.13(c) is taken from the point marked with a star, distance of $r = 5$ Å and $\theta = 20^{\circ}$. This is close to parallel. A molecular pair at the secondary peak area of $r = 9$ Å and $\theta = 90^{\circ}$ is shown in Figure 7.13(d). They are similar to Figures 7.13(a) or 7.13(b) but less curved.

7.4 Relationship between two rings in the same molecule

Similar to the previous section, angles and distances between the two rings in a DCMP or a Dumbbell molecule are charted. The planes for each ring are defined, and the angles between vectors perpendicular to the planes are calculated. Also the centre of mass of each ring provides the coordinate for the distance.

7.4.1 Effect of methyl 'hooks'

The Dumbbell molecule has two cyclohexyl rings on either end of hexane backbone. The distribution of ring pairs as a function of the centre of mass distance

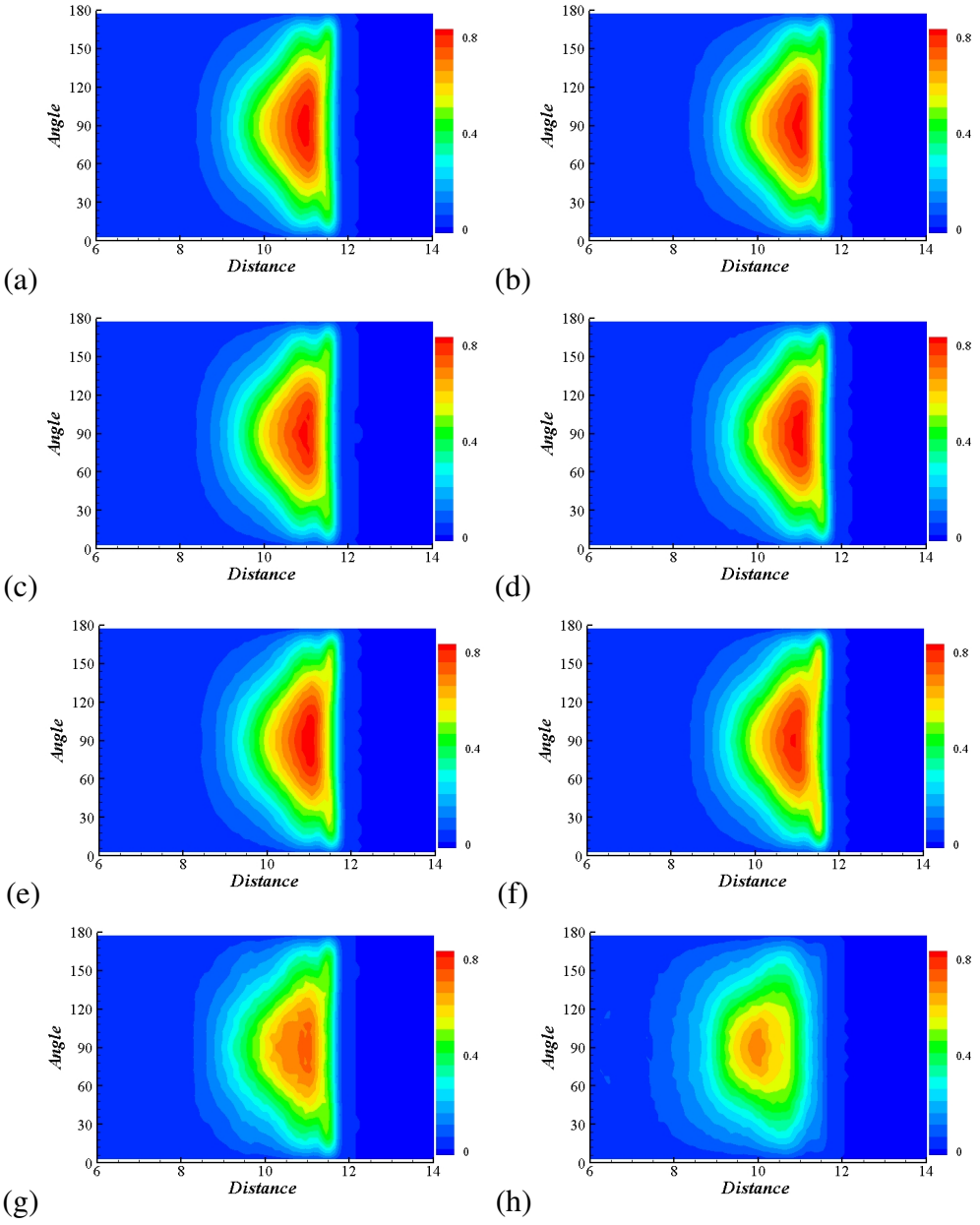

Figure 7.14: Contour plots of the ring separation distance (r_s) and the relative angle (θ) for Dumbbell at various pressures. (a) 1 atm, (b) 10 atm, (c) 30 atm, (d) 100 atm, (e) 300 atm, (f) 1000 atm, (g) 3000 atm, and (h) 10 000 atm.

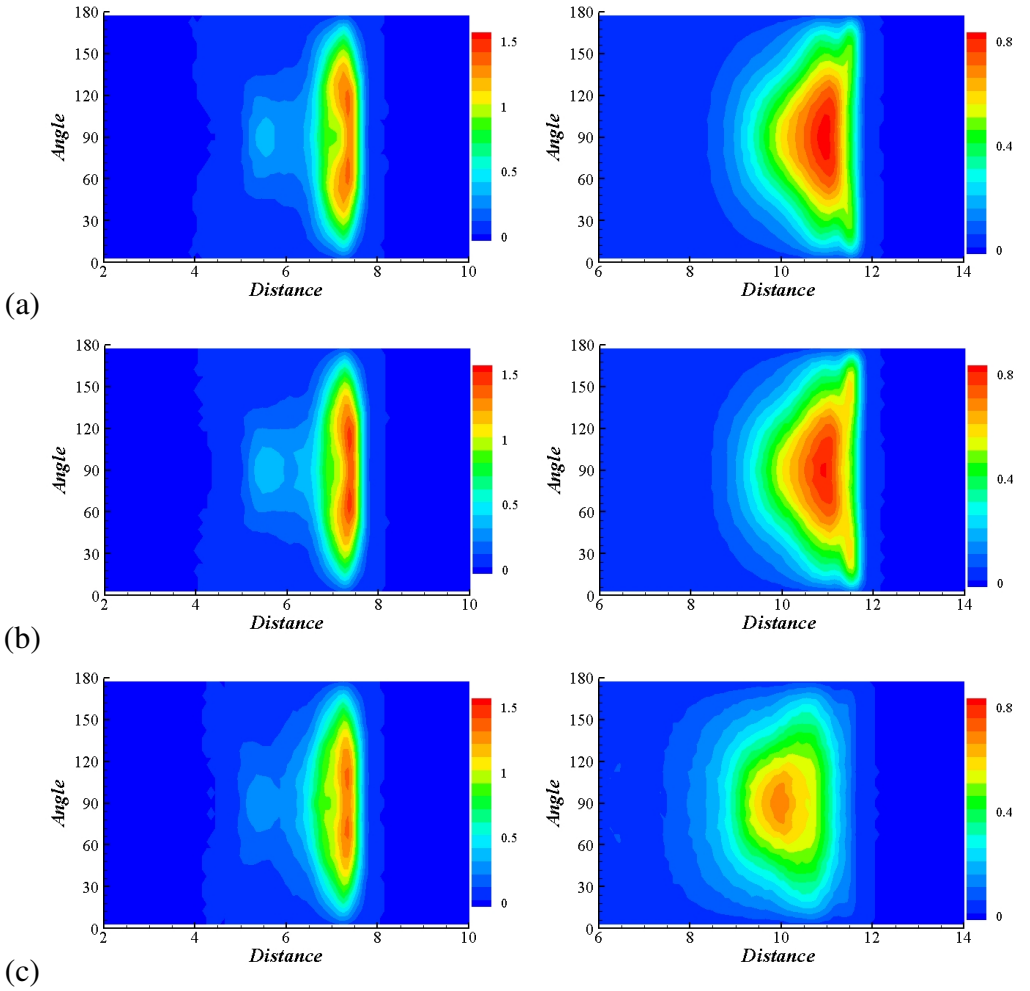

Figure 7.15: Contour plots of the ring separation distance (r_s) and the relative angle (θ) for DCMP (left) and Dumbbell (right) at various pressures. (a) 1 atm, (b) 1000 atm, and (c) 10 000 atm.

and the angles between the rings are mapped in Figure 7.14. The ring pairs are located in an inverse D-shaped area in this 2D map, centering around $r = 11$ Å and $\theta = 90°$. When the rings are closer, they prefer $\theta = 90°$, but the probability

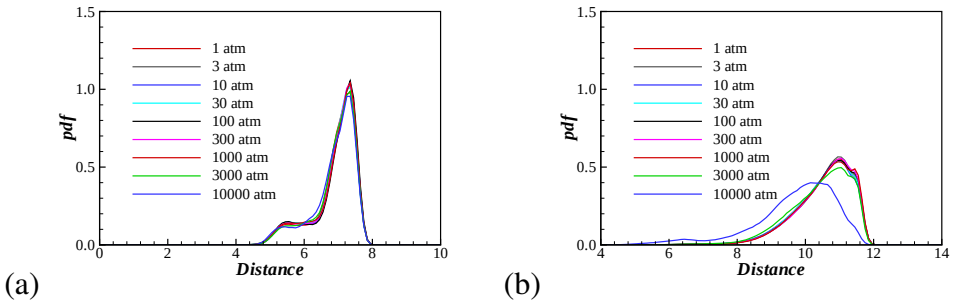

Figure 7.16: 1D pdf plots at various pressures. (a) DCMP and (b) Dumbbell.

of finding a pair at $r = 11$ Å is evenly distributed for all angles. As the pressure increases, the height of the central peak is reduced. A major change occurs between $P = 3000$ atm and $P = 10\,000$ atm: rings in the central area disperse into nearer and smaller angles.

Compared to DCMP as seen in Figure 7.15, the preferred distance between two rings is wider for Dumbbell. DCMP ring distances are concentrated at around $r = 7$ Å and Dumbbell at around $r = 11$ Å. There are four C−C bonds between cyclohexyl rings in DCMP and seven bonds in Dumbbell. The distance difference can be explained by the number of C−C bonds in two molecules. Also, there are more variations in ring distances in Dumbbell due to the simpler nature of the molecular shape, i.e. not having the methyl 'hooks'. Whereas the movement of cyclohexyl rings in DCMP is restricted by the short length of linking C−C bonds and the existence of three methyls, those in Dumbbell are freer to move.

Figure 7.16 is the 1D plot of Figure 7.15 as a function of distance. DCMP

shows little difference in ring distances but the distribution of ring distances for Dumbbell shifts under very high pressure of 10 000 atm.

7.5 Distance and angle between rings in the system

In this section, centre of mass distances and angles between a cyclohexyl ring on a molecule and all other rings in the system except the one that is on the same molecule as the first ring are monitored.

7.5.1 Effect of methyl 'hooks'

Figure 7.17 shows the 2D contour plot of rings of Dumbbell as a function of centre of mass distances and relative angles under various pressures. There are D-shaped peak areas at $5 < r < 7$ Å and $45^\circ < \theta < 90^\circ$. The nearest distance is similar for all pressures. Further peaks are observed at around $r = 11$ Å and 16 Å centred at $\theta = 90^\circ$.

The 2D contour plot of DCMP and Dumbbell under selected pressures using cosine-bins are presented in Figure 7.18. Inter-molecular cyclohexyl ring distances in DCMP and in Dumbbell are of similar order. At the nearest distances, there is a slight preference of parallel positions. The distance of $r = 4.5$ - 7.0 Å is

highly

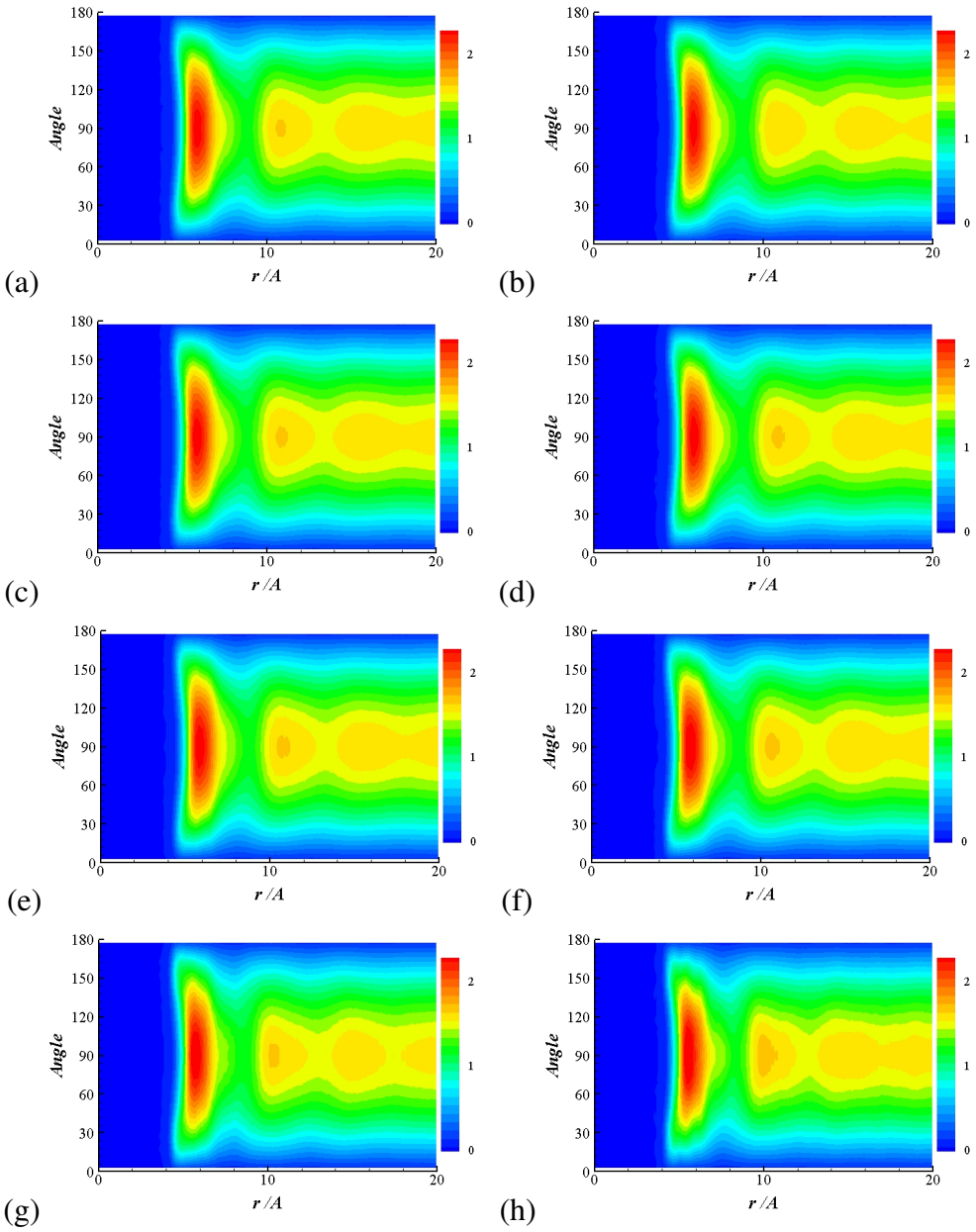

Figure 7.17: Contour maps for distance and angle of two rings of different Dumbbell molecules. (a) 1 atm, (b) 3 atm, (c) 10 atm, (d) 30 atm, (e) 300 atm, (f) 1000 atm, (g) 3000 atm, and (h) 10 000 atm.

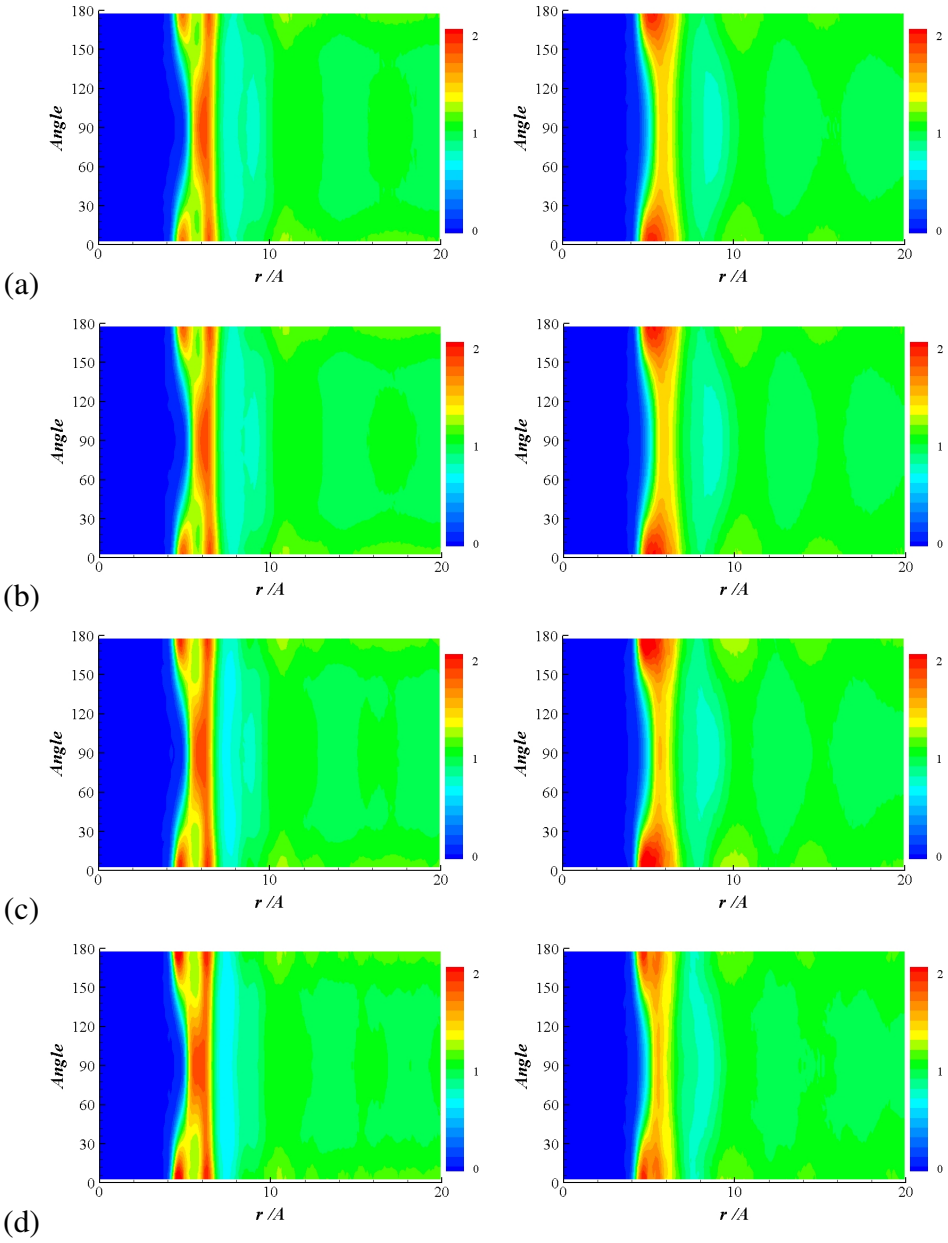

Figure 7.18: Contour maps for distance and angle of two rings of different DCMP (left) and Dumbbell (right) molecules. (a) 1 atm, (b) 300 atm, (c) 3000 atm, and (d) 10 000 atm.

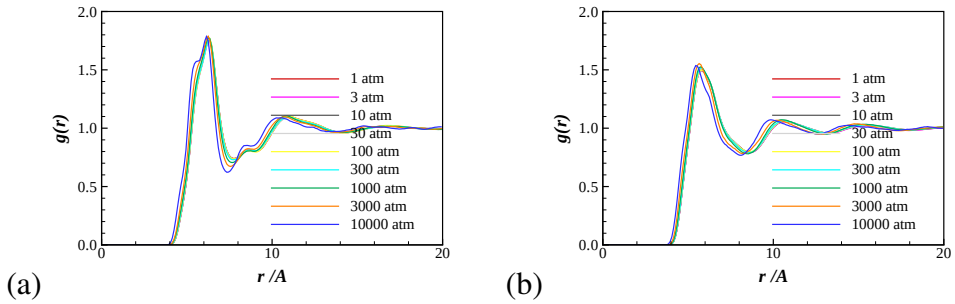

Figure 7.19: RDF for all angles of two rings from different molecules at various pressures. (a) DCMP and (b) Dumbbell.

preferred at all pressures presented. At these distances, rings at all angles exist but the parallel position is preferred. The concentration at this distance band is lessened at higher pressures and there is some evidence of the secondary peak band at $r = 8$ Å. The first concentration peak area of rings in DCMP appears near $r = 5$ Å and parallel position. Then the next closest peak area is concentrated around $r = 7$ Å but perpendicular.

When integrated over the angles as shown in Figure 7.19, the ring distance is stable over the pressure range in DCMP except for slight shift towards smaller r values as the pressure increases. Dumbbell ring distances in Figure 7.19(b) shows more changes. The RDF lines overlap between 1 atm and 1000 atm. At $P = 3000$ atm the line at the peak is lower and at 10 000 atm the peak moves in by $r = 1$ Å and the spread is wider, indicating that the rings are closer to each other than at lower pressures.

Chapter 8

SHEAR VISCOSITIES

One of the most interesting properties of DCMP in engineering applications is its shear responses. This chapter includes the shear viscosity of DCMP in comparison with that of Dumbbell under a range of pressures and shear rates. Simulation conditions with pressures ranging from atmospheric to 10 000 atm, and shear rates up to $\dot{\gamma} = 10^{12}/\mathrm{s}$ are explored. A planar shear was applied to the equilibrated simulation cells and the Freely-Jointed Chain model was used to simulate the shear response of the DCMP and Dumbbell molecules.

8.1 Viscosity of DCMP

In this study, a planar shear is applied to an equilibrated simulation cell using the Lees-Edwards boundary condition. This boundary condition requires the use of a constant volume of the simulation cell. As a result, the pressure of the simulation cell changes depending on the strength of shear applied. Details can be found in Chapter 3.1.5. Therefore we now identify the simulation conditions by the density rather than the pressure. Five density values are considered here. The densities and their corresponding zero shear pressures are presented in Table 8.1.

8.1.1 Effect of shear on the pressure

Pressure changes of DCMP with shear are shown in Figure 8.1. Nine simulations were performed with different shear ($\dot{\gamma}$) values. The overall responses of DCMP to the applied shear are similar for different densities. When the shear is applied, the pressure of the simulation cells increases steadily with the applied shear rate. However, it is found that the changes in pressure due to shear are larger

Table 8.1: The densities and their corresponding zero shear pressures.

Pressure /katm	0.5	1	2	5	10
Density /g/ml	0.96	0.97	1.0	1.05	1.10

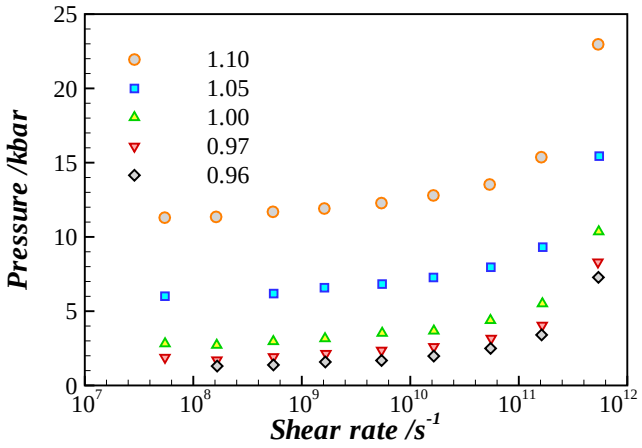

Figure 8.1: Pressure of DCMP as a function of applied shear rate. Pressure is in katm and shear rate in $1/\mathrm{s}$.

for higher density cases. For example, the pressure change for $\rho = 0.96$ g/ml is $\Delta P \approx 7$ kbar, while $\Delta P \approx 12$ katm for $\rho = 1.10$ g/ml when the shear rate increases to $\dot{\gamma} = 5.47 \times \ 10^{11}/\mathrm{s}$. This shows that the DCMP molecules experience much higher pressure than the set pressure condition suggests when there is shear as well as pressure. In particular, for the high density and large shear cases.

8.1.2 Effect of shear on the viscosity

The viscosity of DCMP is monitored during the simulation. Time evolutions of viscosity for different shear rates are presented in Figure 8.2. Figure 8.2(a) includes the simulation results of DCMP at 500 bar and at 5 000 bar with the shear rates $\dot{\gamma} = 5.47 \times 10^{11}/\mathrm{s}$ (Case 0.1) and $\dot{\gamma} = 5.47 \times 10^{10}/\mathrm{s}$ (Case 0.01). These

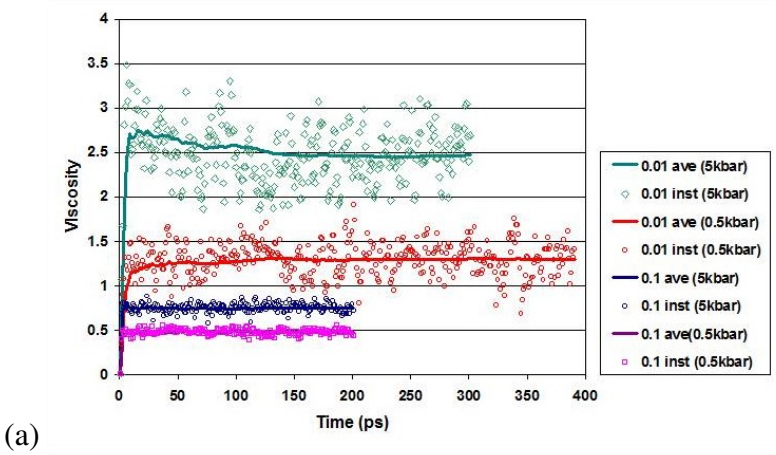

(a)

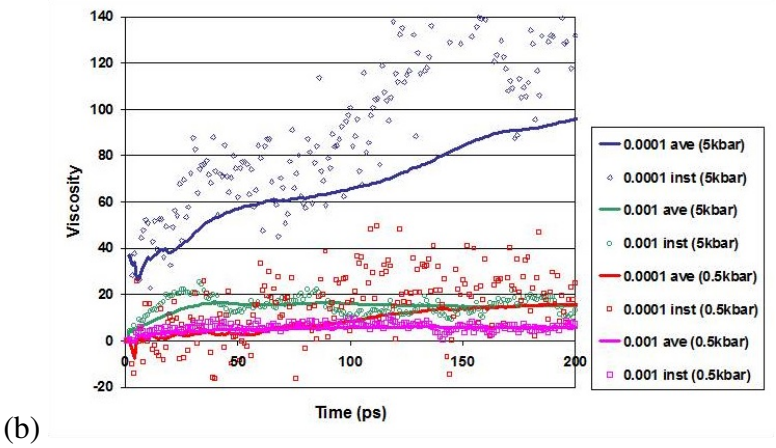

(b)

Figure 8.2: Time evolution of viscosity of DCMP. (a) Shear rates of 0.1 ($\dot{\gamma} = 5.47 \times 10^{11}/\mathrm{s}$) and 0.01 ($\dot{\gamma} = 5.47 \times 10^{10}/\mathrm{s}$) and (b) Shear rates of 0.001 ($\dot{\gamma} = 5.47 \times 10^{9}/\mathrm{s}$) and 0.0001 ($\dot{\gamma} = 5.47 \times 10^{8}/\mathrm{s}$). Pressures of 500 bar and 5 000 bar are presented. Time is in ps and viscosity in cP.

molecules with high shear rates mostly converge within 50 ps with relatively low viscosity. Figure 8.2(b) shows the time evolution of viscosity with the shear rates of $\dot{\gamma} = 5.47 \times 10^{9}/\mathrm{s}$ (Case 0.001) and $\dot{\gamma} = 5.47 \times 10^{8}/\mathrm{s}$ (Case 0.0001). These molecules with relatively lower shear rates took longer to converge and the data is noisier. Therefore, it is expected to require considerably longer calculations for

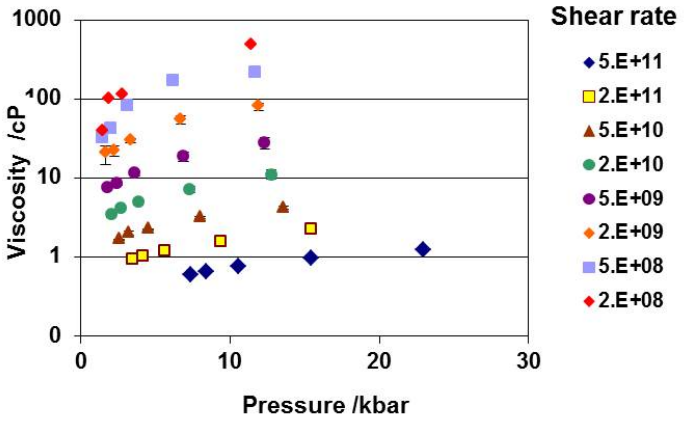

Figure 8.3: Viscosity of DCMP with shear as a function of pressure. Pressure is in kbar, viscosity in cP, and shear rates in $1/\mathrm{s}$.

the lower shear rate regions to achieve the same quality of statistics.

The viscosity of DCMP is presented as a function of pressure for a range of shear rates in Figure 8.3. As the pressure increases, the viscosity also increases as seen in earlier chapters. Also, the viscosity of a system decreases with the increased shear rate. This figure shows the pressure of a system increases and the viscosity is reduced as the shear rate is increased, from the red diamonds to the dark blue diamonds. The far right end of the data have the same density, meaning they had the same pressure before applying the shear. However, when the shear is applied, the highest shear rate of $\dot{\gamma} = 5.47 \times 10^9/\mathrm{s}$ produced almost twice as high pressure than $\dot{\gamma} = 2.38 \times 10^8/\mathrm{s}$. Also for the same pressure, the viscosity of DCMP with shear rate $\dot{\gamma} = 5.47 \times 10^9/\mathrm{s}$ is about 1 cP and the viscosity of DCMP with shear rate $\dot{\gamma} = 2.38 \times 10^8/\mathrm{s}$ is around 500 cP. We can see that under very

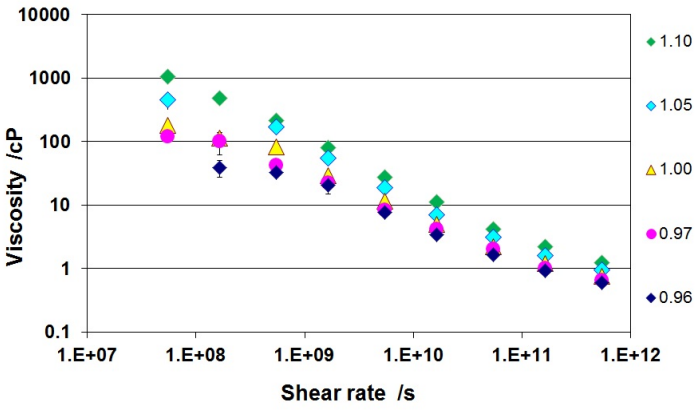

Figure 8.4: Viscosity of DCMP with shear as a function of shear rate. Shear rates is in $1/\mathrm{s}$, viscosity in cP, and density in g/ml.

high shear of $\dot{\gamma} = 5.47 \times 10^{11}/\mathrm{s}$, the viscosity of DCMP is in the region of the viscosity of water, which is 0.89 cP at 298 K.

The viscosity of DCMP is presented as a function of shear rate for a range of densities in Figure 8.4. Shear rate and viscosity are both plotted on a log scale. For all simulations with different density conditions, the viscosity is decreased steadily with the shear rate between $\dot{\gamma} = 5.47 \times 10^{7}/\mathrm{s}$ and $\dot{\gamma} = 5.47 \times 10^{11}/\mathrm{s}$. The changes in viscosity is more pronounced in the high density case. The viscosity of $\rho = 1.10$ g/ml system increased by a factor of 1000 and that of $\rho = 0.97$ g/ml system by a factor of 100. A lower density system of $\rho = 0.96$ g/ml shows greater noise level. Also, the noises are larger in the low shear rate region. Lower density systems start to show a plateau at low shear rates, which is expected for a shear thinning fluid. This is observed for the density conditions of $\rho < 1.0$ g/ml. It

appears that the lower the density, the higher the threshold shear rate where the plateau starts. The viscosity at the start of a plateau is the order of $\eta = 100$ cP for low density cases. This is in the same order of magnitude as the zero shear viscosity estimated from the Stokes-Einstein relation, which is also about $\eta = 100$ cP for low pressure systems.

8.2 Viscosity of Dumbbell

The densities and their corresponding zero shear pressures of Dumbbell are presented in Table 8.2. A similar range of density used for DCMP (Table 8.1) is considered here. Note that the density of Dumbbell is lower than that of DCMP under the same zero shear pressure and as a result, a much higher pressure at zero shear is necessary to model simulation cells of similar density.

Table 8.2: The pressures at zero shear and the corresponding densities.

Pressure /katm	0.5	1	5	7.5	12	15
Density /g/ml	0.89	0.91	0.95	1.02	1.06	1.08

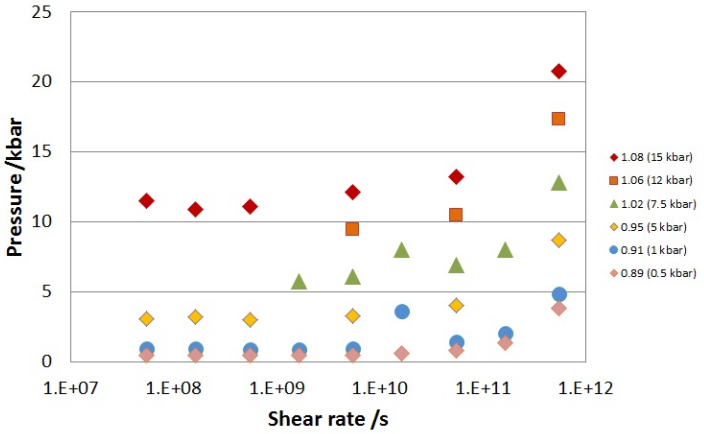

Figure 8.5: Pressure of Dumbbell as a function of applied shear rate. Pressure is in kbar and shear rate in $1/\text{s}$.

8.2.1 Effect of shear on the pressure

Pressure changes of Dumbbell with shear rate are shown in Figure 8.5. When the shear is applied, the pressure of the simulation cells gradually increases as in the DCMP results. However, the scale of change is smaller than that of DCMP. For example, the pressure change for $\rho = 0.95$ g/ml is about $\Delta P \approx 5$ kbar, while $\Delta P \approx 10$ kbar for $\rho = 1.08$ g/ml when shear rate increased to $\dot{\gamma} = 5.47 \times 10^{11}/\text{s}$.

8.2.2 Effect of shear on the viscosity

The effect of shear on the viscosity of Dumbbell is shown in Figure 8.6. The trend is broadly similar to that of DCMP. For a given shear rate, the viscosity increases as pressure increases. The viscosity is higher for lower shear rates, $\dot{\gamma} =$

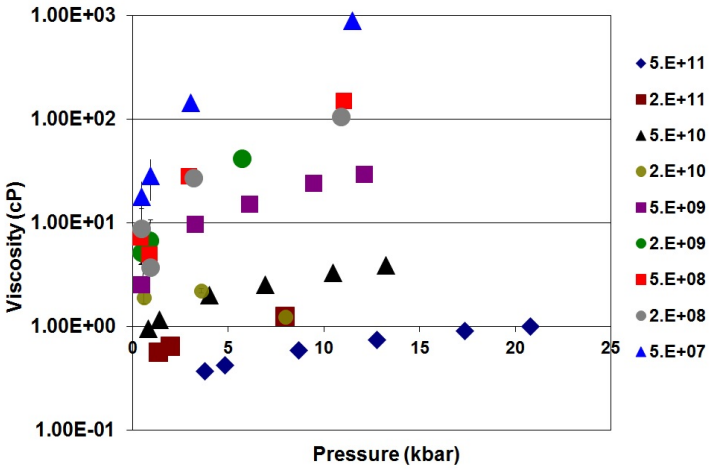

Figure 8.6: Viscosity of Dumbbell as a function of pressure.

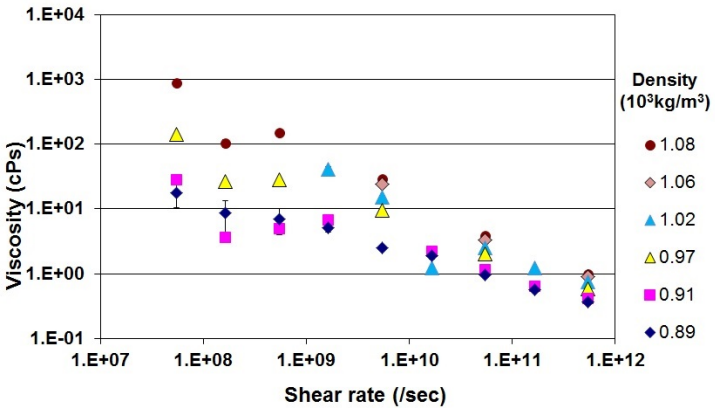

Figure 8.7: Viscosity of Dumbbell as a function of shear rate.

$5.47 \times 10^7/\text{s}$ showing the highest viscosity. The amount of change of the viscosity is also the largest for low shear rates with the viscosity for $\dot{\gamma} = 5.47 \times 10^7/\text{s}$ case increasing by two orders of magnitude.

The viscosity of dumbbell as a function of shear rate is shown in Figure 8.7. Generally the viscosity decreases as shear rate increases. High density systems have higher viscosity. The plateau at lower shear rates is less discernible in the

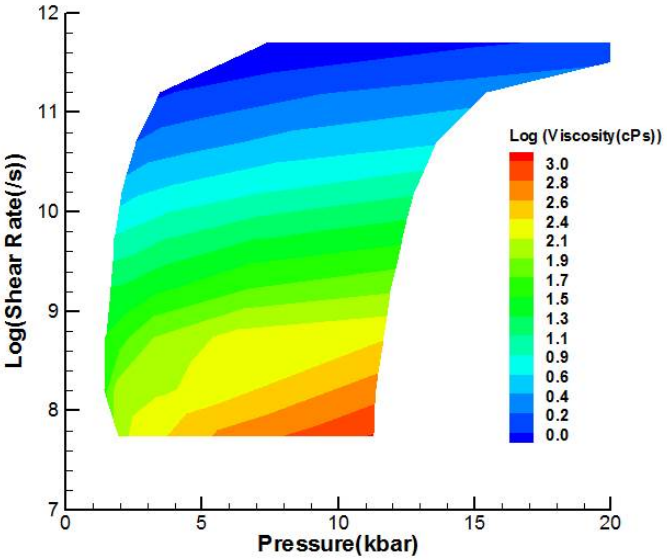

(a)

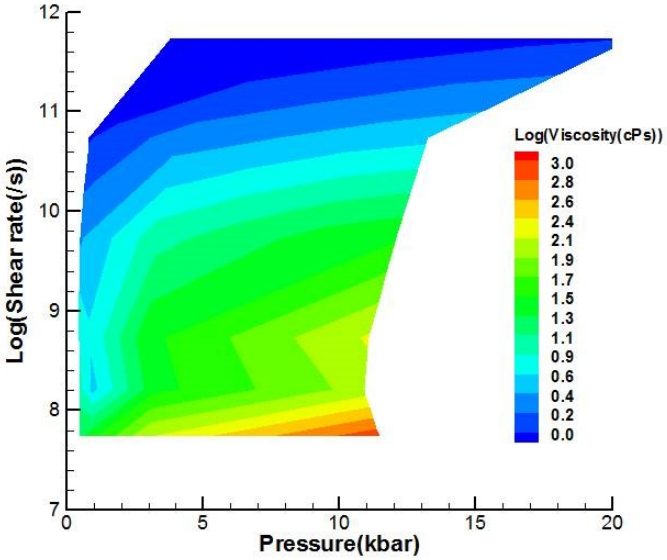

(b)

Figure 8.8: Viscosity of (a) DCMP and (b) Dumbbell as a function of pressure and shear rate.

Dumbbell case. The difference in viscosity between the highest and the lowest density cases is wider at low shear rates and narrow at high shear rates. In other words, for the shear rate $\dot{\gamma} > 10^{11}/\text{s}$, the effect of shear is strong enough to cancel the effect of the density. The viscosity of Dumbbell under shear rate $\dot{\gamma} > 5.47 \times 10^{11}/\text{s}$ is lower than that of water at room temperature, $\rho = 1$ cP.

The 2D viscosity contours of DCMP and Dumbbell for various pressure and shear rate conditions are presented in Figure 8.8. The x-axis is the pressure in kbar and the y-axis is shear rate $(/\text{s})$ in log scale. The viscosity is also plotted on a log scale and with the red colour indicating viscosity $\rho \approx 1000$ cP and the blue $\rho \approx 1$ cP.

Figure 8.8(a) shows that increasing pressure results in higher viscosity for DCMP. The highest viscosity is $\eta = 216.17$ cP at $P = 1.17$ GPa and $\dot{\gamma} < 5 \times 10^{8}/\text{s}$. The viscosity is the highest when the pressure is high and the shear rate is low. This effect is the most strong when the shear is $\dot{\gamma} < 5 \times 10^{8}/\text{s}$ for DCMP. At higher shear rates, the shear thinning effect is stronger and the change is less pronounced.

The viscosity of Dumbbell in Figure 8.8(b) shows a similar pattern as that of DCMP, showing higher viscosity in higher pressure and lower shear rate. However, it can be observed that the viscosity of dumbbell molecule is lower than that of DCMP at the low shear rate region. The viscosity reaches the same magnitude

as that of DCMP. At $\dot{\gamma} = 5.47 \times 10^7/\text{s}$, Dumbbell has viscosity of $\eta = 885.92$ cP, whereas the viscosity of DCMP $\eta = 1185.34$ cP. Again, the viscosity is the highest when the pressure is high and the shear rate is low. For $\dot{\gamma} > 10^{10}/\text{s}$ the effect of pressure was very small.

Chapter 9

CONCLUSIONS

Molecular dynamics simulations of a highly viscous Non-Newtonian fluid, 2,4-dicyclohexyl-2-methylpentane (DCMP) have been studied for a range of pressures, ranging from atmospheric to GPa range. Two additional molecular motifs, octadecane (Linear) and 1,6-dicyclohexane (Dumbbell), were also chosen to examine the effect of methyl ends and rings. It was found that gradually pressurising was not enough to achieve a well equilibrated simulation system. Further heat treatment was necessary for higher pressures. Heating the system to 1000 K and then slow cooling were applied for this purpose.

From the equilibrium molecular simulation results, it is observed that the density of liquids increases as the pressure increases. The density of DCMP and

Dumbbell exhibits a similar pattern with the pressure whereas Linear exhibits a different trend as shown in Figure 6.1. The density of DCMP and Dumbbell increases gradually with increase of pressure until $P = 3000$ atm then shows a sharp increase. The density of Linear seems lower between $P = 10$ and $P = 100$ and shows gradual increase afterwards. The density of all three molecules increases sharply after $P = 3000$ atm. The mean square displacement of molecules decreases as the pressure increases. At pressures higher than 3000 atm, the movement almost ceases for DCMP and Dumbbell. The diffusion coefficients of DCMP reduces most compared to the other two molecular motifs. The greatest change in diffusion coefficient of Linear is observed for $1 \leq P \leq 3$ atm. The coefficient remains of the same order of magnitude at higher pressures. Dumbbell shows a moderate reduction in diffusion coefficient with increasing pressure. The viscosity of each molecule is calculated using the Stokes-Einstein relations. Viscosity of DCMP is higher than that of Dumbbell, and comparable to Linear. Also viscosity changes of DCMP and Linear are larger than that of Dumbbell.

Overall, the RDFs of the centre of mass of molecule show that the first peak of Linear is the shortest. DCMP cannot approach another DCMP as close as Dumbbell or Linear does due to the compact and complex shape of the molecule. The RDF peaks of Linear change dramatically at high pressures. At ambient pressure, Linear molecules are predominantly of a stretched shape. They are mostly

parallel to each other and occasionally perpendicular pairs are found at large distances. Dumbbells are either bent to U-shaped or stretched. The radii of gyration of DCMP and Dumbbell remain at the same length with increasing pressure, whereas that of Linear is reduced significantly under high pressure.

Inter-molecule distances and angles vary with increasing pressure. At close proximity, more Dumbbell molecules are U-shaped and allow another molecule within a short distance. In contrast, DCMP molecules have little scope for this freedom. U-shaped DCMP molecules are observed but methyl hooks prevent another molecule from moving close. At high pressure, the preference for a particular distance and angle between DCMP molecule pairs does not change. At short distances, it is found that there are more Dumbbell molecules which are U-shaped. Linear molecules at $P = 10\,000$ atm have shorter R_g than at $P = 1$ atm. It appears that this hinders mobility and viscosity of the molecule at high pressure.

DCMP has a high viscosity due to its complex and compact molecular shape. The viscosity of Dumbbell increases with increasing pressure. However, Dumbbell can release the effect of pressure more effectively due to the lack of methyl hooks in DCMP and the preference of a longer backbone. Linear does not have any additional structural features such as rings or methyl ends. It is observed that Linear pairs prefer the parallel alignment to each other at a lower pressure. They tend to bend at higher pressure to accommodate the pressure, which may cause a

viscosity increase.

The effect of shear rate on the viscosity of DCMP and Dumbbell is examined. A wide range of shear rates ($5.47 \times 10^7/\mathrm{s} \leq \dot{\gamma} \leq 5.47 \times 10^{11}/\mathrm{s}$) are considered for various density conditions. It is found that the pressure of the simulation cell increases when the shear is applied. The viscosities of DCMP and Dumbbell increase as the pressure increases. The viscosity of DCMP is found to be higher than that of Dumbbell, especially at high pressure region. DCMP and Dumbbell show the shear thinning behaviour. The start of a plateau is observed for DCMP, with the viscosity of the order of $\eta = 100$ cP for low density cases. The zero shear viscosity estimated from the Stokes-Einstein relation is also about $\eta = 100$ cP for the low pressure systems.

Bibliography

[1] R. Larsson and O. Andersson, *Proc. Inst. Mech. Eng. J J. Eng. Tribol.*, 2000, **214**, 337–342.

[2] N. Ohno, *Tribol. Int.*, 2007, **40**, 233–238.

[3] R. M. Gulam, T. Takahashia and Y. Ohga, *Phys. Chem. Chem. Phys.*, 2009, **11**, 5170–5174.

[4] T. Hirayama, K. Nemoto, S. Hayase, Y. Mitsunaga, T. Matsuoka, T. Hattori and T. Kikegawa, *Tribol. Int.*, 2009, **42**, 88–92.

[5] W. W. Wood and F. R. Parker, *J. Chem. Phys.*, 1957, **27**, 720–733.

[6] B. J. Alder and T. E. Wainwright, *J. Chem. Phys.*, 1957, **27**, 1208–1209.

[7] B. J. Alder and T. E. Wainwright, *J. Chem. Phys.*, 1959, **31**, 459–466.

[8] A. Rahman, *Phys. Rev.*, 1964, **136**, A405–A410.

[9] L. Verlet, *Phys. Rev.*, 1967, **159**, 98–103.

[10] L. Verlet, *Phys. Rev.*, 1968, **165**, 201–14.

[11] J. McCammon, B. Gelin and M. Karplus, *Nature*, 1977, **267**, 585–590.

[12] A. W. Lees and S. F. Edwards, *J. Phys. C: Solid State Phys.*, 1972, **5**, 1921–1929.

[13] J.-P. Ryckaert and A. Bellemans, *Faraday Discuss.*, 1978, **66**, 95–106.

[14] J. Ramos, J. F. Vega and J. Martinez-Salazar, *Macromolecules*, 2015, **48**, 5016–5027.

[15] P. Brault and E. C. Neyts, *Catalysis Today*, 2015, **256**, 3–12.

[16] J. K. Leman, M. B. Ulmschneider and J. J. Gray, *Proteins - Structure function and bioinfomatics*, 2015, **83**, 1–244.

[17] I. Avramov, *J. Non-Cryst. Solids*, 2009, **355**, 745–747.

[18] Y. Xu and M. J. Green, *J. Polym. Sci. Part B Polym. Pys.*, 2015, **53**, 1247–1253.

[19] M. Chen, J. R. Vella, A. Z. Panagiotopoulos, P. G. Debenedetti, F. H. Stillinger and E. A. Carter, *AICHE Journal*, 2015, **61**, 2841–2853.

[20] L. Bai, S.-N. Li, Q.-G. Zhai, Y.-C. Jiang and M.-C. Hu, *Chem. Pap.*, 2015, **69**, 1378–1388.

[21] Q.-S. Liu, J. Liu, X.-X. Liu and S.-T. Zhang, *J. Chem. Thermodynamics*, 2015, **90**, 39–45.

[22] O. Skurtys, R. Andrade and F. Osorio, *LWT-Food Sci. and Tech.*, 2015, **64**, 131–139.

[23] B. C. Porto, P. E. D. Augusto, A. Terekhov, B. R. Hamaker and M. Cristianini, *Carbihydrate Polymers*, 2015, **129**, 187–193.

[24] G.-J. Guo and Y.-G. Zhang, *Mol. Phys.*, 2001, **99**, 283–289.

[25] S. Bair, *Proc. Inst. Mech. Eng. J J. Eng. Tribol.*, 2002, **216**, 139–149.

[26] S. Bair, F. Qureshi and M. Kotzalas, *Proc. Inst. Mech. Eng. J J. Eng. Tribol.*, 2004, **218**, 95–98.

[27] T. Asano, K. Matsuo and H. Sumi, *Bull. Chem. Soc. Jpn.*, 1997, **70**, 239–244.

[28] K. Uppulury, P. S. Coppock and J. T. Kindt, *J. Phys. Chem. B*, 2015, **119**, 8725–8733.

[29] D. H. de Jong, N. Liguori, T. van den Berg, C. Arnarez, X. Periole and S. J. Marrink, *J. Phys. Chem. B*, 2015, **119**, 7791–7803.

[30] O. M. Szklarczyk, E. Arvaniti and W. F. van Gunsteren, *J. Comput. Chem.*, 2015, **36**, 1311–1321.

[31] J. D. Moore, S. T. Cui, H. D. Cochran and P. T. Cummings, *J. Chem. Phys.*, 2000, **113**, 8833–8840.

[32] C. McCabe, S. Cui, P. T. Cummings, P. A. Gordon and R. B. Saeger, *J. Chem. Phys.*, 2001, **114**, 1887–1891.

[33] C. McCabe, S. Cui and P. T. Cummings, *Fluid Phase Equilibria*, 2001, **183-184**, 363–370.

[34] C. McCabe, D. Bedrov, O. Borodin, G. D. Smith and P. T. Cummings, *Ind. Eng. Chem. Res.*, 2003, **42**, 6956–6961.

[35] E. Kiran and Y. Sen, *Int. J. Thermophys.*, 1992, **13**, 411–442.

[36] A. Berker, S. Chynoweth, U. C. Klomp and Y. Michopoulos, *J. Chem. Soc. Faraday Trans.*, 1992, **88**, 1719–1725.

[37] T. A. Hunt and B. D. Todd, *J. Chem. Phys.*, 2009, **131**, 054904.

[38] T. A. Hunt and B. D. Todd, *Mol. Sim.*, 2009, **35**, 1153–1167.

[39] R. S. Payal, S. Balasubramanian, I. Rudra, K. Tandon, I. Mahlke, D. Doyle and R. Cracknell, *Mol. Sim.*, 2012, **38**, 1234–1241.

[40] H. Washizu, S. Sanda, S. Hyodo, T. Ohmori, N. Nishino and A. Suzuki, *SAE Technical Paper*, 2007, **116**, 414.

[41] H. Washizu and T. Ohmori, *Lubrication Science*, 2010, **22**, 323–340.

[42] J. C. Mauro, Y. Yue, A. J. Ellison, P. K. Gupta and D. C. Allan, *Proc. Natl. Acad. Sci. U. S. A.*, 2009, **106**, 19780–19784.

[43] C. Barus, *Am. J. Sci.*, 1893, **45**, 87–96.

[44] T. Asano, *Pure Appl. Chem.*, 1999, **71**, 1691–1704.

[45] H. Hata and T. Tsubouchi, *Tribol. Lett.*, 1998, **5**, 67–74.

[46] L. I. Kioupis and E. J. Maginn, *J. Phys. Chem. B*, 1999, **107**, 10781–10790.

[47] L. I. Kioupis and E. J. Maginn, *Chem. Eng. J.*, 1999, **74**, 129–146.

[48] J. E. Jones, *Proceedings of the Royal Society of London A: Mathematical, Physical and Engineering Sciences*, 1924, **106**, 463–477.

[49] P. J. Debye, *Chem. Phys.*, 1946, **14**, 636.

[50] W. Jorgensen and J. Tiradorives, *J. Am. Chem. Soc.*, 1988, **110**, 1657–1666.

[51] S. J. Marrink, H. J. Risselada, S. Yefimov, D. P. Tieleman and A. H. de Vries, *J. Phys. Chem. B*, 2007, **111**, 7812–7824.

[52] S. Marrink, A. de Vries and A. Mark, *J. Phys. Chem. B*, 2004, **108**, 750–760.

[53] V. Tozzini, *Curr. Opin. Struct. Biol.*, 2005, **15**, 144–150.

[54] S. Izvekov and G. Voth, *J. Phys. Chem. B*, 2005, **109**, 2469–2473.

[55] B. Arash, H. S. Park and T. Rabczuk, *Compos. Pt. B-Eng.*, 2015, **80**, 92–100.

[56] D. Case, T. Cheatham, T. Darden, H. Gohlke, R. Luo, K. Merz, A. Onufriev, C. Simmerling, B. Wang and R. Woods, *J. Comput. Chem.*, 2005, **26**, 1668–1688.

[57] M. Christen, P. Hunenberger, D. Bakowies, R. Baron, R. Burgi, D. Geerke, T. Heinz, M. Kastenholz, V. Krautler, C. Oostenbrink, C. Peter, D. Trzesniak and W. Van Gunsteren, *J. Comput. Chem.*, 2005, **26**, 1719–1751.

[58] W. L. Jorgensen, D. S. Maxwell and J. Tirado-Rives, *J. Am. Chem. Soc.*, 1996, **118**, 11225–11236.

[59] M. G. Martin and J. I. Siepmann, *J. Phys. Chem. B*, 1998, **102**, 2569–2577.

[60] B. Brooks, R. Bruccoleri, B. Olafson, D. States, S. Swaminathan and M. Karplus, *J. Comput. Chem.*, 1983, **4**, 187–217.

[61] B. R. Brooks, C. L. Brooks, III, A. D. Mackerell, Jr., L. Nilsson, R. J. Petrella, B. Roux, Y. Won, G. Archontis, C. Bartels, S. Boresch, A. Caflisch, L. Caves, Q. Cui, A. R. Dinner, M. Feig, S. Fischer, J. Gao, M. Hodoscek, W. Im, K. Kuczera, T. Lazaridis, J. Ma, V. Ovchinnikov, E. Paci, R. W. Pastor, C. B. Post, J. Z. Pu, M. Schaefer, B. Tidor, R. M. Venable, H. L. Wood-

cock, X. Wu, W. Yang, D. M. York and M. Karplus, *J. Comput. Chem.*, 2009, **30**, 1545–1614.

[62] M. P. Allen and D. J. Tildesley, *Computer Simulation of Liquids*, Clarendon Press, 1987.

[63] W. Swope, H. Andersen, P. Berens and K. Wilson, *J. Chem. Phys.*, 1982, **76**, 637–649.

[64] W. G. Hoover, *Phys. Rev. A*, 1985, **31**, 1695–1697.

[65] H. J. C. Berendsen, J. P. M. Postma, W. F. van Gunsteren, A. DiNola and J. R. Haak, *J. Chem. Phys.*, 1984, **81**, 3684–3690.

[66] W. Smith and I. T. Todorov, *Mol. Sim.*, 2006, **32**, 935–943.

[67] W. Smith and T. Forester, *J. Molec. Graphics*, 1996, **14**, 136–141.

[68] W. Smith, C. W. Yong and P. M. Rodger, *Mol. Sim.*, 2002, **28**, 358–471.

[69] Y. Kondo, T. Koyama and S. Sasaki, in *Ionic Liquids - New Aspects for the Future*, ed. J.-I. Kadokawa, InTech, 2013.

[70] W. E. Campbell, *Boundary Lubrication, an Appraisal of World Literature, ASME*, 1969, 0187–117.

[71] B. O. Åhrström, O. Andersson and W. Holweger, *Tribol. Lett.*, 2005, **20**, 255–262.

[72] G. Scherer, *J. Am. Ceram. Soc.*, 1992, **75**, 1060–1062.

[73] I. Avramov, *J. Non-Cryst. Solids*, 1988, **104**, 253–260.

[74] C. Roelands, *Correlational Aspects of the Viscosity-Temperature-Pressure Relationship of Lubricating Oils. PhD thesis.*, Delft University of Technology, The Netherlands., 1966.

[75] M. M. Cross, *J. Humphrey Colloid Science*, 1965, **20**, 417–437.

[76] P. Sollich, *Phys. Rev. E*, 1998, **58**, 738–759.

[77] Democritus, *Radial Distribution Function.*, 2015, `http://www.ccp5.ac.uk/DL_POLY/Democritus/Theory/rdf.html`.

[78] P. Atkins and J. de Paula, *Physical Chemistry*, Oxford University Press, Oxford, 2002.

[79] T. Tsubouchi and H. Hata, *Tribol. Int.*, 1994, **27**, 183–3187.

[80] C. L. Yaws, *Thermophysical Properties of Chemicals and Hydrocarbons, 2nd ed.*, Elsevier Inc., 2014.

[81] ChemSpider, *2,4-dicyclohexyl-2-methylpenatane*, 2017, `http://www.chemspider.com/Chemical-Structure.85270.html`, [Online; accessed 23-September-2017].

[82] ChemSpider, *1,6-dicyclohexylhexane*, 2017, http://www.chemspider.com/Chemical-Structure.109738.html, [Online; accessed 23-September-2017].

[83] ChemSpider, *octadecane*, 2017, http://www.chemspider.com/Chemical-Structure.11145.html, [Online; accessed 23-September-2017].

[84] C. W. Yong and Science &Technology Facilities Council, *DL_FIELD*, 2015, https://ccpforge.cse.rl.ac.uk/gf/project/ccpbiosim/wiki/?pagename=DL+Field, [Online; accessed 23-September-2017].

[85] A. R. Leach, *Molecular Modelling: Principles and Applications.*, Prentice Hall, 2nd edn., 2001.

[86] D. Yin and A. MacKerell, Jr., *J. Comput. Chem.*, 1998, **19**, 334–348.

[87] A. MacKerell, Jr., *J. Comput. Chem.*, 2004, **25**, 1584–1604.

[88] K. Vanommeslaeghe, E. Hatcher, C. Acharya, S. Kundu, S. Zhong, J. E. Shim, E. Darian, O. Guvench, P. Lopes, I. Vorobyov and J. A. MacKerell, *J. Comput. Chem.*, 2010, **31**, 671–690.

[89] H. O. Baled, D. Xing, H. Katz, D. Tapriyal, I. K. Gamwo, Y. Soong, B. A. Bamgbade, Y. Wu, K. Liu, M. A. McHugh and R. M. Enick, *J. Chem. Thermodynamics*, 2014, **72**, 108–116.

[90] W. Humphrey, A. Dalke and K. Schulten, *J. of Molecular Graphics*, 1996, **14**, 33–38.